UNIVERSITY OF SOUTHAMPTON

COMPUTER SIMULATIION OF LIQUID CRYSTALS

by

AMIR H. GHAHRAI

A dissertation submitted in partial fulfilment of
the requirement of the degree of Master of Philosophy
at the University of Southampton.

Department of Chemistry

March 2002

Contents

Acknowledgments

I would like to thank Professor Geoffrey. R. Luckhurst for all his help and understanding throughout my MPhil degree.

Special thanks go to Dr Giacomo Saielli who never hesitated to help me with the problems, both scientific and computational, that I encountered during my MPhil degree.

I would also like to thank Dr Katsuhiko Satoh, Dr Jochen Schacht and Dr B.A. Timmimi who created a live atmosphere in the office at all times and most importantly their enthusiasm and clever discussions about liquid crystals which inspired me.

Thanks to my brothers and sisters for their support and understanding.

To the memory of my parents ...

Chapter 1

Introduction to liquid crystals

1.1 The liquid crystalline phase

Liquid crystals represent a state of matter that is intermediate between crystalline solids and amorphous liquids. Substances in this state of matter are strongly anisotropic in some of their properties and yet exhibit a certain degree of fluidity, which in some cases may be comparable to that of an ordinary liquid. The term anisotropic means that the results of measurements of a physical property differs, depending on the direction in which it is measured. Thus, liquids are isotropic (all directions are equivalent) and liquid crystals are anisotropic (not all directions are equivalent). When viewed under a polarising microscope, liquid crystals show optical textures, which indicate an anisotropy in the refractive index. Solids can be either isotropic or anisotropic depending on the structure of the crystal lattice. For example, a cubic solid is isotropic while solids with other symmetries are anisotropic.

In order to understand the structure of the liquid crystalline phase, it is useful to consider first the well-known structure of crystals and liquids. The basic difference between states of matter is that the constituent particles are arranged in different geometrical configurations under different thermodynamic conditions. In general, for a given state point defined by temperature and pressure, specific molecular interactions determine the possible configurations of the given system. In a crystal, the molecules are regularly stacked and fixed in their positions. There is both translational and orientational order at long range. The centres of mass of the molecules are regularly arranged on lattice sites and the ordering of the molecules is extended throughout the whole sample as well as over all six degrees of freedom; three from translation and three from rotation, thus creating a three-dimensional periodic lattice. In liquids, however, because of the high thermal energy relative to the molecular interactions, the molecules move randomly in all directions. There is orientational and translational order of immediate neighbours (i.e. short-range order) but at large distances, there is no correlation either in the positions or the orientations of the molecules. The system possesses full rotational and translational symmetry.

Liquid crystals fall between these two extremes; there is orientational and sometimes positional ordering of the molecules, but in both cases, there is not order for all degrees of freedom. The term mesophase is sometimes used to refer to this intermediate phase and the molecules which form liquid crystal phases are referred to as mesogenic. An example of such a mesogenic molecule with the associated phase behaviour is given in figure 1.1.

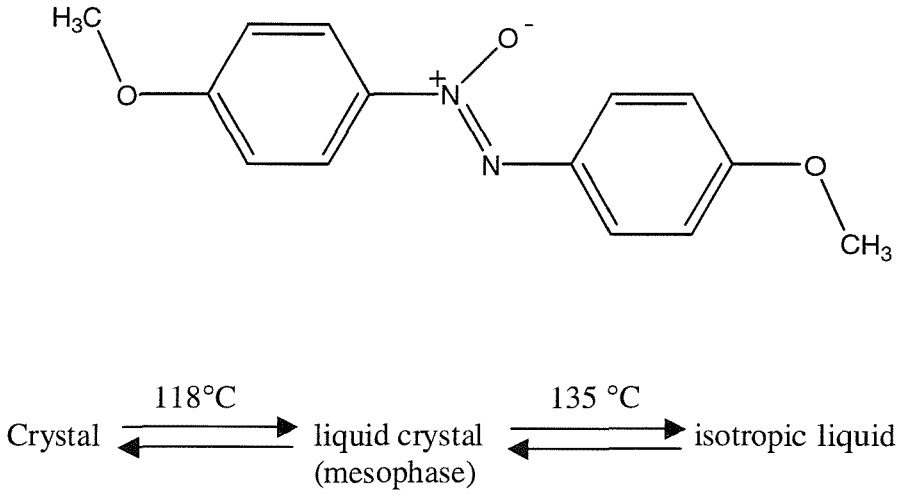

Figure 1.1 A typical mesogen commonly called para-azoxyanisole, abbreviated as PAA, although its correct name is 4,4'-dimethoxyazoxybenzene.

1.2 Molecular structure

One of the key features common to all liquid crystal materials is the anisotropy in the shape of the constituent molecules. Thus, the molecular symmetry tends to be lower than that of a spherical molecule and in fact it has been observed that the mesogenic molecules normally have rod-like or disk-like structures, however mesophases formed from rod-like molecules (calamitics), are more common than the ones formed from disk-like molecules (discotics). The constituent rod-like molecules are usually assumed to have cylindrical symmetry and most consist of a rigid core to satisfy and maintain the

elongated structure necessary to form mesophases. Examples of rod-like and disk-like molecules with their idealised shapes are given in figure 1.2(a) and 1.2(b), respectively. The alkyl chain, as well as giving a rod-like structure, also lowers the melting point However, there are other variations to the simple rod or disk-like structures. Experiments [1] have confirmed that mesophases are formed from compounds which are more complex in shape. An example is that with two cyanobiphenyls linked by a platinum dichloride. Platinum dichloride is almost ellipsoidal in shape while the cyanobiphenyl part is considered as cylindrical. That is the shape can therefore be taken to be spherocylindrical with a bump in the middle, this is shown systematically in figure 1.2(b). It is expected that these molecules would form tilted phases, to maximise the packing efficiency. Molecules shown in figures 1.2(a) and 1.2(b) both form nematics with different transition temperatures, 308K for 5CB and 447K for the rod-like particle.

a)

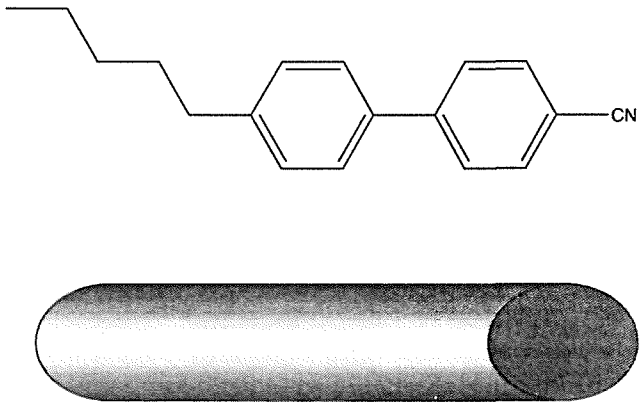

b)

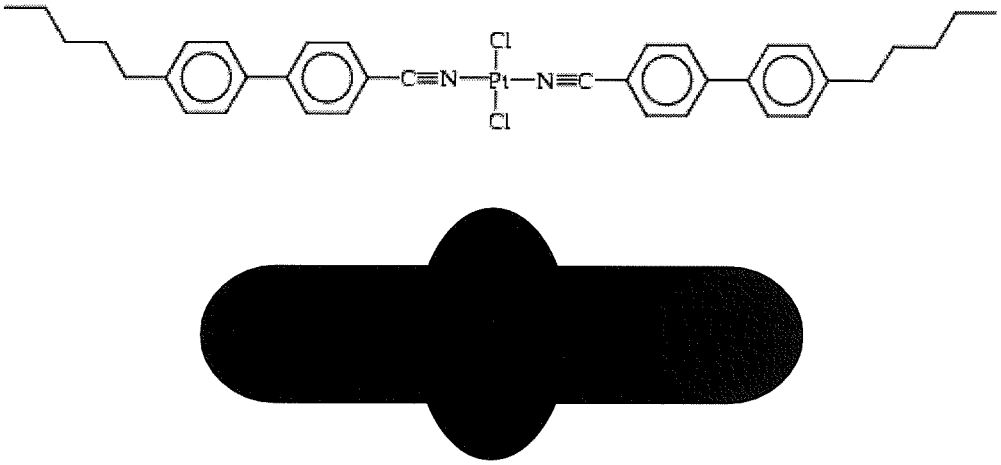

c)

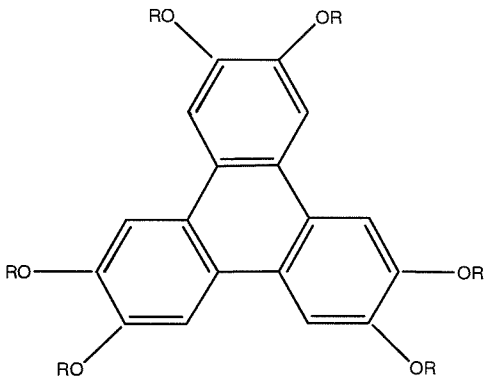

R = C_5H_{11}

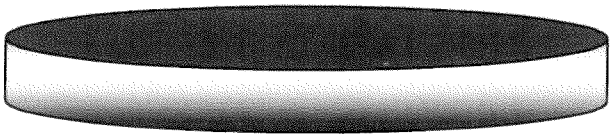

Figure 1.2 Representation of calamitic (a) and (b) and discotic (c) molecules with their idealised analogues.

1.3 Ordering of the molecules

The defining characteristic of liquid crystals is their long-range orientational order. A unit vector $\hat{n}$, named the director, is introduced as a reference with which to help describe this orientational order. In a liquid crystalline phase the molecular symmetry axis, of either rods or discs, on average, tends to be parallel to the director. The resultant long-range orientational order is also responsible for the anisotropy in the properties of a mesophase. The complete description of the orientational order at the single molecule level is provided by the singlet orientational distribution function, $f(\beta)$, which gives the probability density of finding a molecule at a given orientation to the director. If we consider just one molecule in the system and its orientation with respect to $\hat{n}$, see figure 1.3, then we would notice that over time, the angle β, which is the angle between the director and the symmetry axis of the molecule, would vary and $f(\beta)$ would be a continuous function which has a maximum at $\beta = 0°$ (or 180°) and minimum at 90° (or –90°).

1.3.1 Orientational order parameter $\langle P_2 \rangle$

In general, $f(\beta)$ is difficult, but not impossible, to measure experimentally and another approach to describing the orientational order is in terms of order parameters. A complete set of these can be obtained by expanding $f(\beta)$ as a series of Legendre polynomials, $P_L(\cos\beta)$,[2]

$$f(\beta) = \sum_L f_L \; P_L(\cos\beta), \qquad (1.1)$$

where f_L are the expansion coefficients.

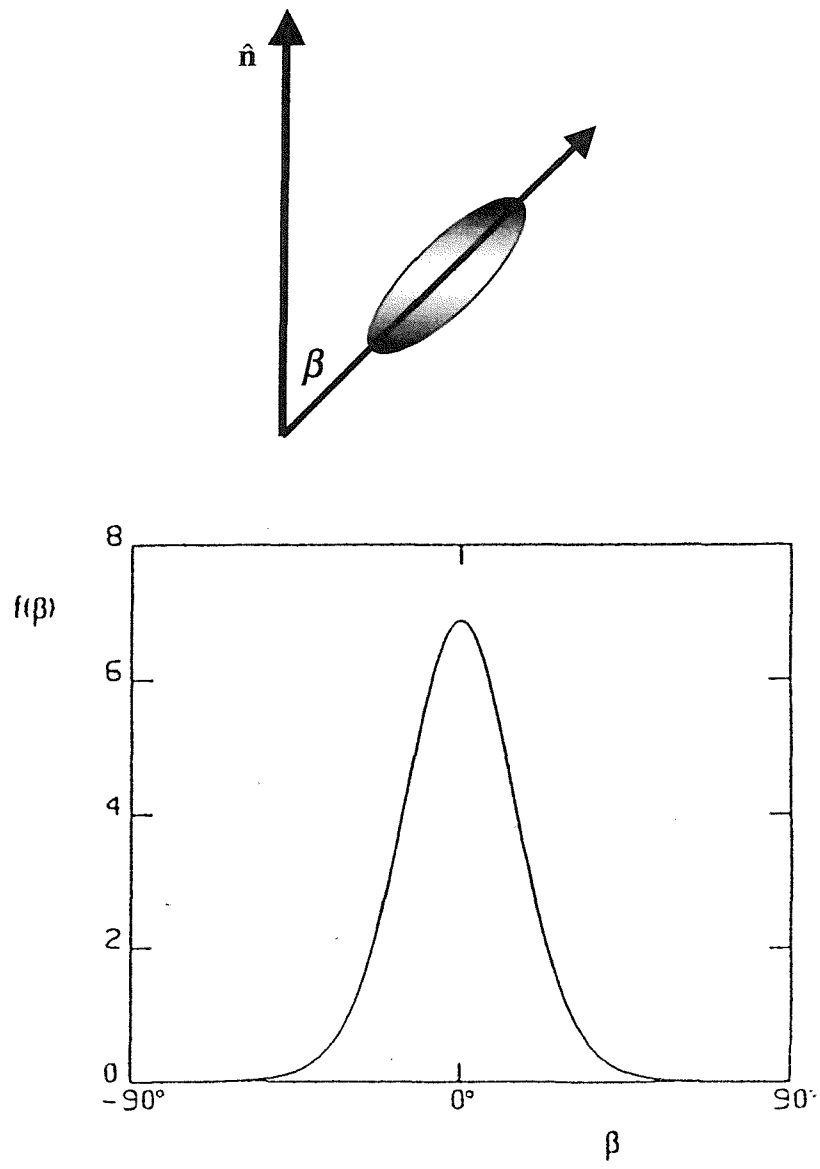

Figure 1.3 Singlet orientational distribution function $f(\beta)$ for a rod-like molecule as a function of the angle between the assumed molecular symmetry axis and the director.

The first few Legendre polynomials are defined as

$$P_0(\cos\beta) = 1, \tag{1.2}$$

$$P_1(\cos\beta) = \cos\beta, \tag{1.3}$$

$$P_2(\cos\beta) = (3\cos^2\beta - 1)/2, \tag{1.4}$$

$$P_3(\cos\beta) = (5\cos^3\beta - 3\cos\beta)/2, \tag{1.5}$$

$$P_4(\cos\beta) = (35\cos^4\beta - 30\cos^2\beta + 3)/8, \tag{1.6}$$

$$P_5(\cos\beta) = (63\cos^5\beta - 70\cos^3\beta + 15\cos\beta)/8, \tag{1.7}$$

$$P_6(\cos\beta) = (231\cos^6\beta - 315\cos^4\beta - 105\cos^2\beta - 5)/16, \tag{1.8}$$

In an uniaxial phase composed of rod-like molecules, there is a plane of symmetry perpendicular to the director, that is $f(\beta) = f(\pi-\beta)$, therefore, $f(\beta)$ is an even function of $\cos\beta$. Therefore, the expansion coefficients of the odd rank polynomials must vanish since they cannot contribute to $f(\beta)$.

The remaining expansion coefficients can be found by multiplying both sides of equation (1.1) by $P_N(\cos\beta)$ and integrating over $\sin\beta d\beta$ gives

$$\int_0^{\pi} f(\beta)P_N(\cos\beta)\sin\beta d\beta = \sum f_L \int P_L(\cos\beta)P_N(\cos\beta)\sin\beta d\beta\,. \tag{1.9}$$

Using the orthogonality of the Legendre functions, we find that when L = N, the expansion coefficient f_L is

$$f_L = (2N+1)\langle P_N\rangle/2\,, \tag{1.10}$$

where $\langle P_N\rangle$ represents a set of orientational order parameters and is defined as

$$< P_N >= \int_0^{\pi} P_N(\cos\beta)f(\beta)\sin\beta d\beta \tag{1.11}$$

In principle the complete definition of the distribution function, $f(\beta)$, is given by an infinite set of even rank order parameters, $\langle P_N \rangle$,

$$f(\beta) = \frac{1}{2} + \left(\frac{5}{2}\right) < P_2 > P_2 \cos\beta + \left(\frac{9}{2}\right) < P_4 > P_4(\cos\beta) + \ldots \quad (1.12)$$

with the limiting values of 0 and 1, indicating disorder and complete order, respectively. In practice, the second rank order parameter is the dominant at least in the vicinity of the nematic-isotropic phase transition and can provide a good description of the orientational order present in a mesophase,

$$\langle P_2 \rangle = 3(\langle \cos^2\beta \rangle - 1)/2 \, . \quad (1.13)$$

The angular brackets denote an ensemble average over all the molecules in th e sample. In an isotropic phase, the average of the cosine squared term is 1/3, giving a zero value for the order parameter, while for a perfect crystal, the order parameter is unity. Typical values of the order parameter of a liquid crystal range between 0.3 at T_{NI} and 0.7 at a reduced temperature, T/T_{NI}, of about 0.8.

1.4 Classification of liquid crystals

There are two main classes of liquid crystals.

a) Lyotropic liquid crystals

Lyotropic liquid crystals are multi-component systems formed by mixtures of amphiphilic molecules and usually a polar solvent. Amphiphilic molecules consist of a hydrophilic

polar head attached to a hydrophobic hydrocarbon tail containing one or two alkyl chains. The most common examples are fatty acids, which when dissolved in water, form micelles to maximise the interactions, both the chain-chain and water-polar heads. These can then interact to form isotropic or liquid crystalline phases, depending now on temperature and concentration and the anisotropy of the micelle.

b) Thermotropic liquid crystals

These are pure organic compounds in which the change in phase is brought about by thermal processes that is by a change in temperature. However, it is also possible to induce a phase change by varying the pressure while keeping the temperature constant, but experimentally, it is more convenient to vary the temperature.

The long range ordering in a thermotropic liquid crystal can be used to differentiate thermotropics into two broad categories:

i) orientational order only as in nematics.

ii) orientational and positional order as in smectics.

In the following sub-sections, we consider the structure in the main liquid crystal phases, namely nematics and smectics.

Nematic phase

Nematics are the simplest and most disordered of the liquid crystal mesophases, with a viscosity normally similar to that of an isotropic phase. There is no translational order, i.e. there is no long-range correlation between the centres of mass of the molecules, but there is a short-range correlation in position similar to that of isotropic liquids.

However, the characteristic feature of the nematic phase is the presence of the long-range orientational order, see figure 1.4. That is, within the sample the molecular orientations are correlated over long distances and by definition are, on average, parallel to the director. The preferred direction usually varies from point to point in the sample but the director can be induced to align in a particular direction by applying an external field, e.g. a magnetic field, to the sample. Optical properties suggest that the nematic phase is uniaxial since light can pass through only one axis without change in plane of polarisation. It is assumed that in the nematic phase, there is a cylindrical symmetry about the director, hence the symmetry of the phase is described as $D_{\infty h}$. Also, there is a plane of symmetry perpendicular to the director so that $\hat{n}$ and $-\hat{n}$ are equivalent which gives $D_{\infty h}$ rather than $C_{\infty v}$ symmetry.

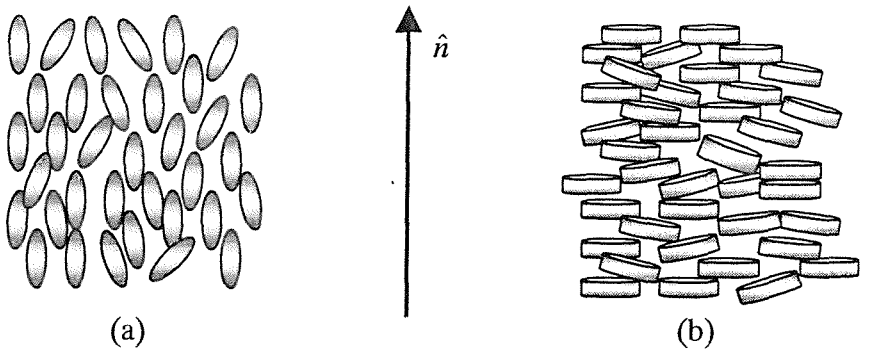

Figure 1.4 A pictorial representation of the nematic phase, showing the existence of long range orientational order for (a) calamitics and (b) discotics.

Smectic phases

Smectic phases all have a layer structure, i.e. there is a tendency for the centres of mass of the molecules to be arranged in layers. This is why smectic phases are more viscous than nematics. This gives rise to long-range translational ordering usually in one dimension as well as orientational ordering. These will be explained in detail in Chapter 4.

Smectic A (SmA) phase

The SmA phase is the least ordered of the smectic phases. There is orientational ordering of molecules within each layer similar to that of nematics, see figure 1.5. The translational ordering of molecules results in a layered structure with layer spacing, d, often approximately equal to the molecular length, but within each layer, there is no long-range translational order. The director is parallel to the layer normal as shown in figure 1.5. The system possesses a one-dimensional translational ordering and the symmetry of the phase is $D_{\infty h}$ as for a nematic.

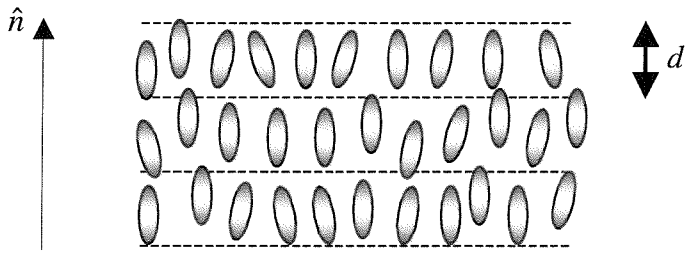

Figure 1.5 The arrangement of the molecules in a smectic A phase.

Smectic C (SmC) phase

The SmC phase is the tilted analogue of the SmA phase; that is the director is tilted with respect to the layer normal, see figure 1.6. The tilt directions of the director in the layers are correlated for a monodomain sample. The tilt angle, ω, can be determined from X-ray studies as well as ESR spectroscopy. Like the SmA phase, there is no translational correlation between the molecules in the layers, and the orientational order of the molecules is similar to that of the SmA. There are now three unequal directors in which the orientational ordering of the molecules, together with the tilted director in each layer produces biaxiality in the optical and other properties of a SmC phase. The symmetry of the phase is characterised as C_{2h}.

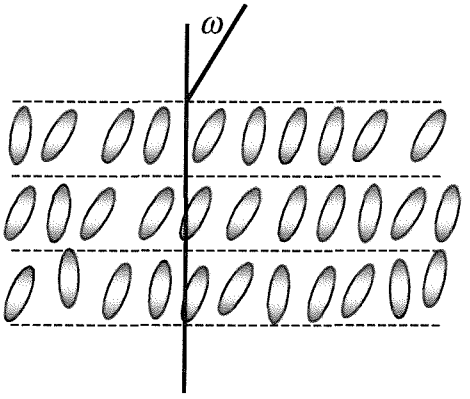

Figure 1.6 The tilted arrangement of molecules in a smectic C phase.

Smectic B (SmB) phase

The SmB phase is the most ordered of the smectic phases. There is translational, as well as orientational ordering, of the molecules within each layer but no correlation between the layers. Locally, the molecules are arranged hexagonally, see figure 1.7. The

arrangements are such that the positional order does not propagate over large distances but the bond orientational order does. The bond orientational order for a particle i at a position r_i is defined as

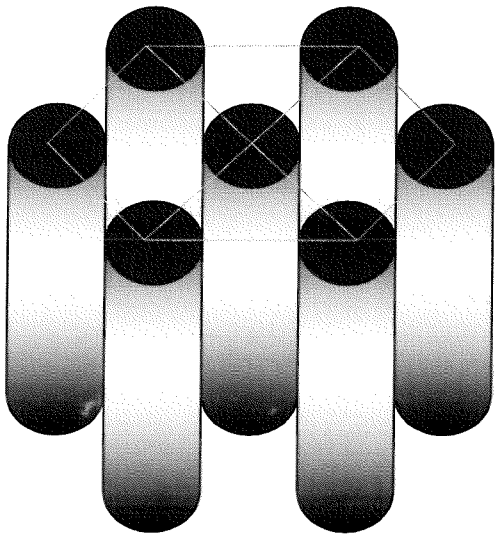

Figure 1.7 A representation of the local hexagonal arrangement of molecules in a layer of a SmB phase.

$$\Psi_6(\mathbf{r}_i) = \frac{\sum_k w(r_{ik}) \exp(6i\theta_{ik})}{\sum_k w(r_{ik})} . \qquad (1.14)$$

In this expression, the summation is over the neighbouring particles and θ_{ik}, see figure 1.8, is the angle between the unit vectors $(\mathbf{r}_i - \mathbf{r}_k)$ projected onto the plane normal to the director and a fixed reference axis and w is the weighting factor which controls the contribution to Ψ with molecules with a particular distance from particle i. The phase is optically uniaxial and belongs to the D_{6h} point group, due to the bond orientational order which extends throughout the sample. For two particles separated by a distance r,

$\langle\Psi_6(0)\Psi_6(r)\rangle$, the bond orientational order does not decay to zero in the smectic B phase, but it does in the smectic A phase, see figure 1.8.

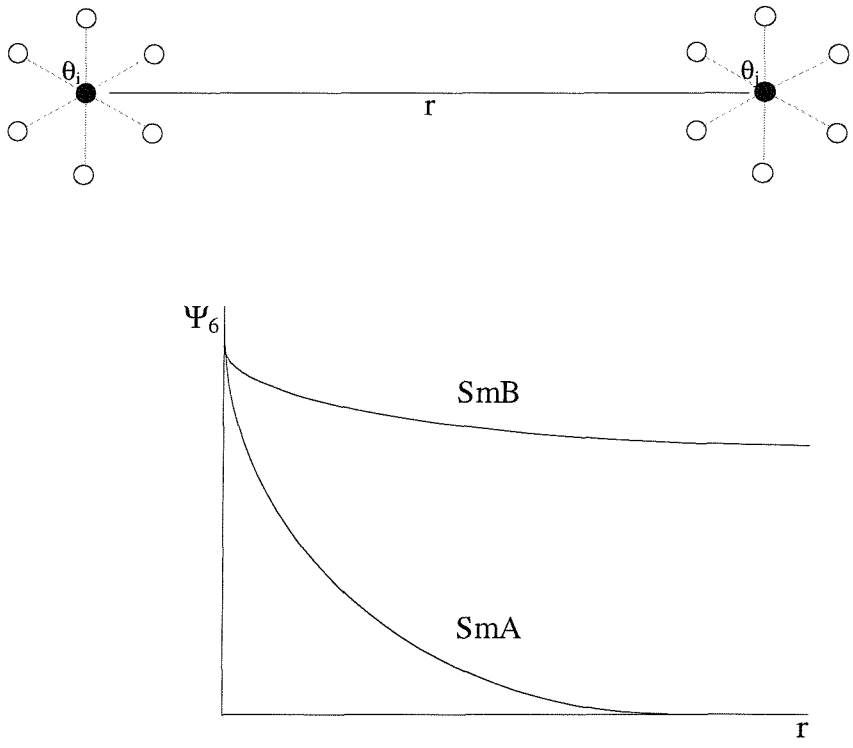

Figure 1.8 A representation of the bond orientational order, Ψ_6, which decays to 0 for SmA and a constant non-zero value for SmB for two molecules separated by a distance r.

Crystal B phase

The crystal B phase is similar in essentially all aspects to the SmB phase, but now there is a correlation of the positions of the molecules between and within layers. This means that there is 3D order and the phase is a crystal. The molecules are free to rotate about their symmetry axis and the structure is optically uniaxial.

1.5 Phase transitions

A phase transition is usually characterised by a change in the order of the phases involved, i.e. entropy S, and the magnitude of ΔS, which is related to the change in enthalpy, H, of the system with temperature, is a quantitative measure of the difference in the order of the two phases.

At the phase transition, the two phases are in equilibrium and so the change in the Gibbs free energy, ΔG, is zero which gives,

$$\Delta S = \Delta H / T_{trans}. \qquad (1.15)$$

For a first order transition, the entropy change is non-zero and so the heat capacity at constant pressure diverges because it is the second derivative of the Gibbs free energy

$$T\left(\frac{\partial^2 G}{\partial T^2}\right)_p = -C_p. \qquad (1.16)$$

A second order transition is one where the first derivative of the Gibbs free energy is continuous but the second derivative is discontinuous. That is the enthalpy and entropy changes at the transition are both zero and there is a finite change in heat capacity, as shown in figure 1.9 (b).

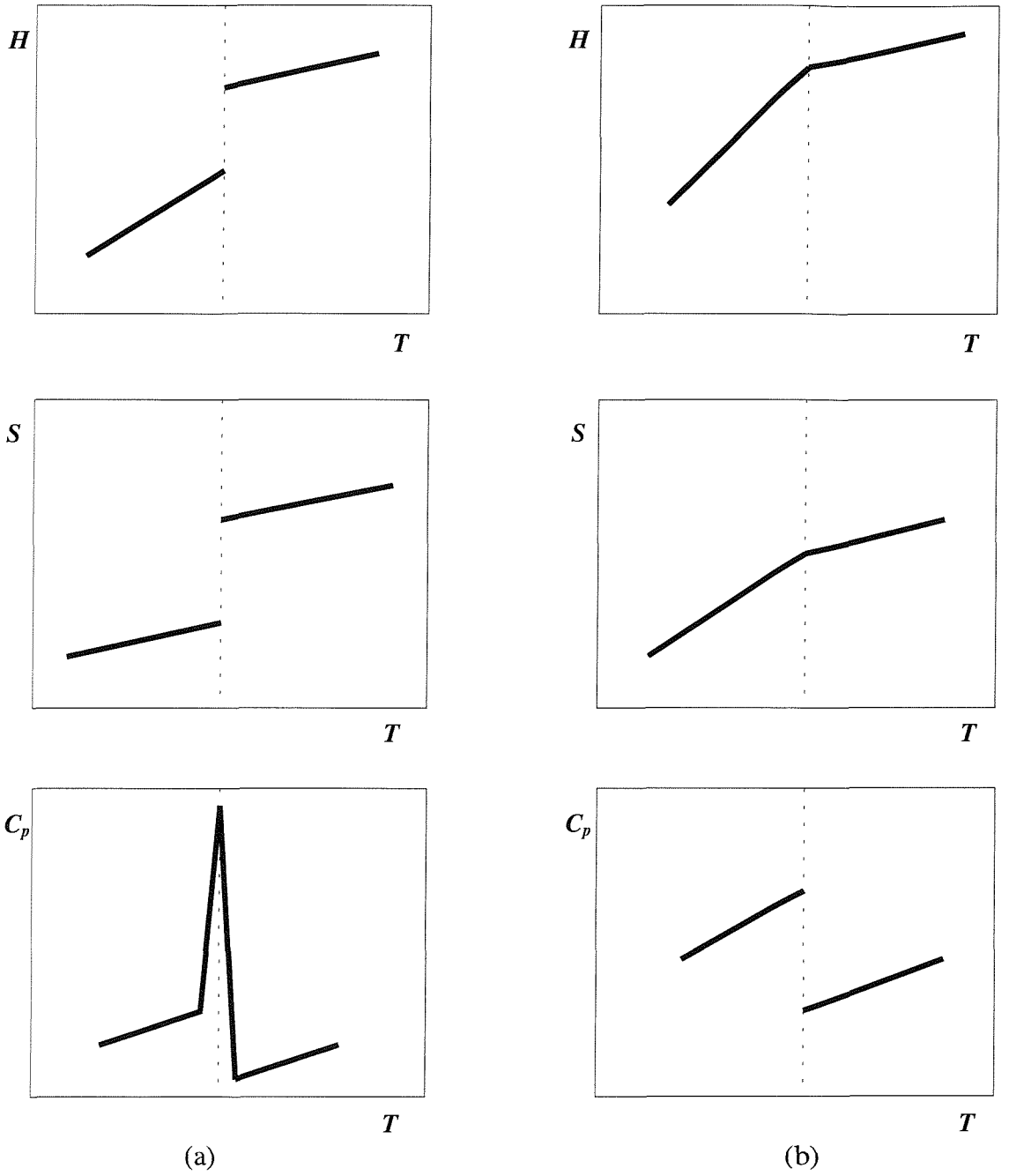

Figure 1.9 Changes in the thermodynamic properties at (a) first and (b) second order phase transitions for a system at constant pressure.

Outline for the rest of the thesis

In this Chapter, we have discussed briefly what a liquid crystal is. We have described the necessary elements for the formation of a mesophase, namely, anisotropy in the shape of the molecules and in the attractive forces, as we shall see in later Chapters. We then compared the properties and in particular the molecular organisation in the main liquid crystal phases, i.e. nematic and smectics. Our understanding of the behaviour of liquid crystals at the molecular level has been considerably enhanced by computer simulation studies. The success of such investigations is, necessarily, dependent on the choice of the intermolecular potential; indeed, this will determine whether the system even forms liquid crystal phases or not. Chapter 2, describes three different, but related, model potentials which are used in computer simulations. These are the Lennard-Jones, the Corner and the Gay-Berne potentials; the latter is an example of a Corner potential. Although it is possible to include anisotropic attractive forces in the Lennard-Jones potential to exhibit liquid crystalline phases, the form of the potential, however, does not allow for the investigation of changes in the anisotropic shape, hence came the development of the more sophisticated single site Corner potential which expresses the coefficients in it in terms of the orientation of the two particles with respect to each other and their intermolecular vector. Single site potentials have the advantage of being computationally cheaper as opposed to multi-site or atomistic potentials. In Chapter 3, we introduce the S-function Corner potential. We explain what S-functions are and how they can be combined, with appropriate coefficients, to mimic the shapes of real nematogens, at least to some extent.

Chapter 4 discusses the technique of computer simulation, its strengths and weaknesses, and in particular the implementation of the Monte-Carlo algorithm to enhance our understanding of phase behaviour and the properties of systems interacting via the model potentials. Finally, in Chapter 5, we discuss in detail and compare the results for the three systems which we have simulated, in particular their thermodynamic behaviour and structural features.

Chapter 2

Molecular Interaction Potentials

2.1 Introduction

The simulation methodology for the study of soft condensed matter is now well-established so that the major challenge for any simulation study is the design of the intermolecular potential. In order to understand the behaviour of liquid crystals at the molecular level, it is essential to choose a potential which includes anisotropic interactions, both attractive and repulsive, i.e. the potential should depend on the separation as well as the orientations of the molecules and their intermolecular vector, since the molecules responsible for the formation of any liquid crystalline phase are anisotropic in shape.

When two molecules come close to one another, the various interactions between the electrons of one molecule and the electrons of the other produce a potential energy of interaction. At very small distances the molecules repel each other strongly. At very large distances there is no interaction between the two molecules and the potential energy

approaches zero. At some intermediate distance, the potential energy is negative corresponding to the attraction between molecules. The attractive and repulsive parts of the potential help investigate how effectively two molecules interact by the indication of the well depth and the contact distance.

In this Chapter we shall consider three different types of potentials, (a) the Lennard-Jones potential for atoms, (b) the Corner potential, an extension of the Lennard-Jones model to molecules and (c) the Gay-Berne potential, which is a special case of the Corner potential.

2.2 The Lennard-Jones Potential

One of the simplest models for describing atomic interactions is that of a system of spherical particles interacting via a pairwise potential that depends only on the magnitude of the separation, $r = | \boldsymbol{r}_i - \boldsymbol{r}_j|$ between pairs of atoms. The Lennard-Jones potential is a useful function which describes the distance dependence of the interactions between two atoms or two molecules with spherical symmetry; its functional form is given by

$$U_{LJ} = 4\varepsilon\left[\left(\frac{\sigma}{r}\right)^{12} - \left(\frac{\sigma}{r}\right)^{6}\right] . \qquad (2.1)$$

It is a sum of the short-range repulsive contribution ~ $1/(r)^{12}$ and the attractive contribution ~ $1/(r)^{6}$.

Attractive term

This describes the attraction between two atoms. When they are brought close to each other, charge density fluctuations in the electronic shell of the first atom polarises the electronic shell of the other. The attraction between the instantaneous and induced dipoles leads to the attractive inverse sixth power term; this is the London dispersive interaction which is often known as the van der Waals interaction, this also includes other weak attractive contributions.

Repulsive term

Unlike the attractive term, the exact functional form for the repulsive interaction is not well-known. The twelfth power dependence for the repulsive energy is chosen for convenience and because it provides a reasonable fit to the experimental data. It is also practical for computer simulations, as it is the square of 6 and hence can be calculated relatively quickly.

Parameters σ and ε

As we can see from figure 2.1 and equation (2.1), σ is the point where U changes sign, and a measure of the diameter of the atom. It is the distance where the energy of the interaction is zero that is the attractive and repulsive forces are exactly balanced. The minimum in the Lennard-Jones potential is at $r = 2^{1/6}\sigma$. The strength of the interaction at this minimum is denoted by ε, also known as the well depth, which is the minimum energy for the interaction between two particles. The values of σ and ε are usually extracted from

experimental data, such as crystal structures, thermodynamic properties and kinetic coefficients, since they are very difficult to calculate from first principles except for the simplest of atoms.

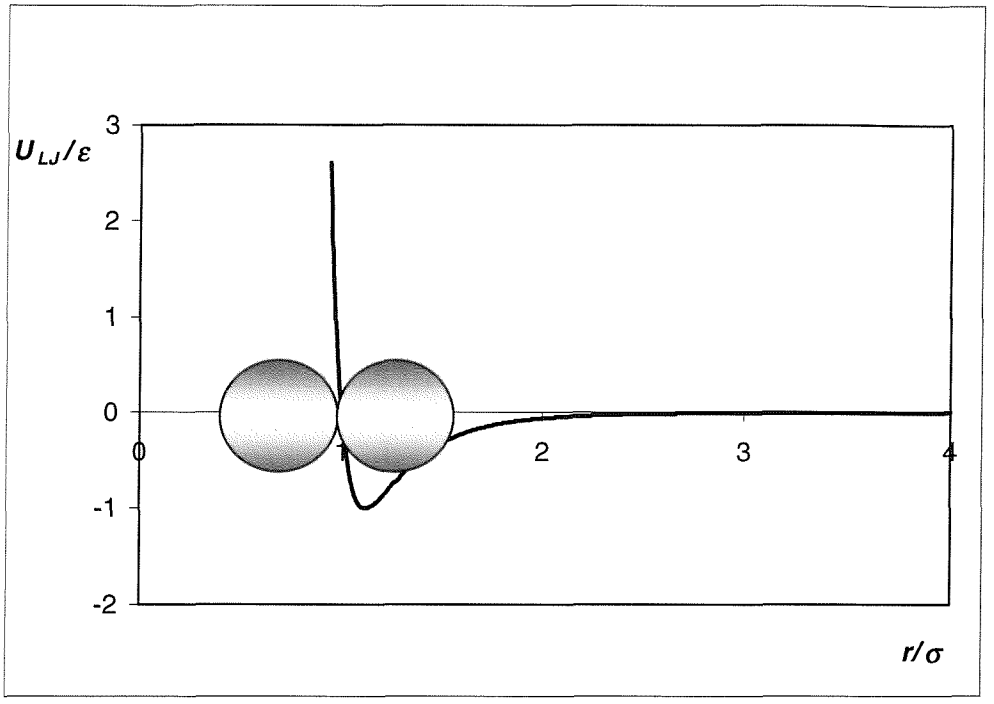

Figure 2.1 A representation of the interaction energy as a function of the intermolecular separation, for two Lennard-Jones atoms.

2.3 The Corner Potential

The Lennard-Jones potential proves to be a valuable model for describing the interaction energy between two spherical particles, such as atoms. However, when

considering molecules where the symmetry is much less than that of atoms, this simple potential is no longer appropriate. In particular the potential must now depend not only on the separation but also on the orientation of the two molecules and the vector joining them. A new potential with these characteristics was proposed by Corner [3]. The importance of the Corner potential is that it is a single-site molecular pair potential $U(\hat{\mathbf{u}}_1,\hat{\mathbf{u}}_2,\mathbf{r})$, of the form $\varepsilon f(r/\sigma)$ where the strength parameter ε, and the range parameter σ are assumed to depend on the orientations of the molecules, $\hat{\mathbf{u}}_1$ and $\hat{\mathbf{u}}_2$, as well as the orientation of the intermolecular vector, $\hat{\mathbf{r}}$, see figure 2.2.

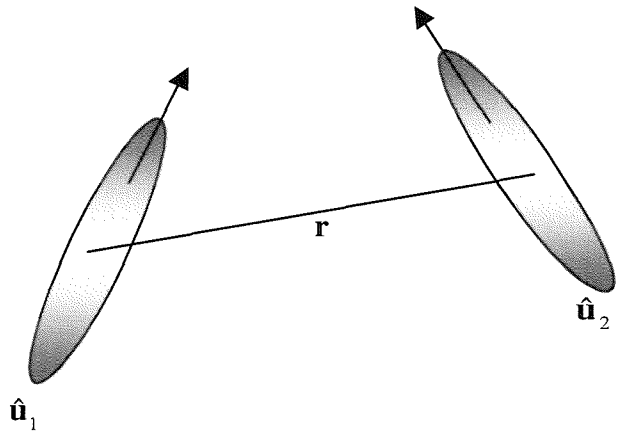

Figure 2.2 The three vectors defining the orientations of the two molecules and the vector joining them.

In Corner's formalism, the potential was assumed to have the scaled Lennard-Jones 12-6 form,

$$U(\hat{\mathbf{u}}_1, \hat{\mathbf{u}}_2, \mathbf{r}) = 4\varepsilon(\hat{\mathbf{u}}_1, \hat{\mathbf{u}}_2, \hat{\mathbf{r}})\left[\left(\frac{\sigma(\hat{\mathbf{u}}_1, \hat{\mathbf{u}}_2, \hat{\mathbf{r}})}{r}\right)^{12} - \left(\frac{\sigma(\hat{\mathbf{u}}_1, \hat{\mathbf{u}}_2, \hat{\mathbf{r}})}{r}\right)^{6}\right], \qquad (2.2)$$

where $\varepsilon(\hat{\mathbf{u}}_1,\hat{\mathbf{u}}_2,\hat{\mathbf{r}})$ is the strength function taken as the potential well depth, and $\sigma\ (\hat{\mathbf{u}}_1,\hat{\mathbf{u}}_2,\hat{\mathbf{r}})$ is the range function considered as the contact distance. The well depth was expressed as

$$\left(\frac{\varepsilon(\hat{\mathbf{u}}_1,\hat{\mathbf{u}}_2,\hat{\mathbf{r}})}{\varepsilon_0}\right)^{1/2} = 1+\left[\frac{10}{9}\left(\frac{l}{\sigma_0}\right)^2 - \frac{9}{8}\frac{l}{\sigma_0}\right]F_1 + \frac{9}{8}\frac{l}{\sigma_0}F_3 - \frac{l}{7\sigma_0}F_4\ , \tag{2.3}$$

where l is the length of the molecules and ε_0 is the well depth which is the value of $\varepsilon(\hat{\mathbf{u}}_1,\hat{\mathbf{u}}_2,\hat{\mathbf{r}})$ for the side-by-side configuration ($f_0 = 1, f_1 = f_2 = 0$). The range function was expressed as

$$\begin{aligned}\left(\frac{\sigma(\hat{\mathbf{u}}_1,\hat{\mathbf{u}}_2,\hat{\mathbf{r}})}{\sigma_0}\right)^{1/3} &= 1-\frac{2}{5}\frac{l}{\sigma_0}+\frac{7}{2}\frac{l}{\sigma_0}F_1+21\left(\frac{l}{\sigma_0}\right)^3F_2 \\ &\quad -14\left(\frac{l}{\sigma_0}\right)+16\left(\frac{l}{\sigma_0}\right)^3F_1F_4-25\left(\frac{l}{\sigma_0}\right)^3F_2F_4\ ,\end{aligned} \tag{2.4}$$

In these functions we have introduced a short hand notation for the functions used for the expansions, thus

$F1 = f_1 + f_2,$
$F2 = f_1^{\,2} f_2^{\,2},$
$F3 = f_0 f_1 f_2 - f_1^{\,2} f_2^{\,2},$
$F4 = f_0^{\,2} - 2f_0 f_1 f_2 + f_1^{\,2} f_2^{\,2}\ ,$

where $f_0 = \hat{\mathbf{u}}_1 \cdot \hat{\mathbf{u}}_2$, $f_1 = \hat{\mathbf{u}}_1 \cdot \hat{\mathbf{r}}$ and $f_2 = \hat{\mathbf{u}}_2 \cdot \hat{\mathbf{r}}$. The expansion coefficients for the ε and σ functions were determined by fitting the expansion to a set of previously determined depth and positions of the potential minima of a range of molecules with different anisotropies. respectively. For these site-site models, the pair potential was determined as the sum of the individual site-site interactions, via

$$U = \sum_{i=1}^{4}\sum_{j=1}^{4} U_{ij}(\mathbf{r}_{ij}). \tag{2.5}$$

where i and j denote atoms in the different molecules. The interaction between the *i*th and *j*th centres on molecule *1* and *2*, respectively, was defined to be Lennard-Jones form

$$U = 4\varepsilon\left[\left(\frac{\sigma}{r_{ij}}\right)^{12} - \left(\frac{\sigma}{r_{ij}}\right)^{6}\right]. \tag{2.6}$$

Although, Corner's potential was a major improvement for studying molecules with anisotropic shapes it only works for small molecules, because Corner used only a small number of terms in the expansion and consequently, this form of the potential is unsuitable for the study of liquid crystals where typically the length-to-breadth ratio of 3 or greater is necessary to form liquid crystalline phases [4]. Also in the Corner potential, the well width varies for different orientations of the molecules, which is unrealistic. In the next section we shall see how the Gay-Berne potential overcome these problems.

2.4 The Gay-Berne potential

The Gay-Berne potential [5], is an extension of the Berne and Pechukas [6] potential, based on the Gaussian overlap model. Like the Corner potential, it is a single site potential with parameters which depend on the orientations of two particles as well as that of the vector linking them.

$$U(\hat{\mathbf{u}}_i, \hat{\mathbf{u}}_j, \hat{\mathbf{r}}) = 4\varepsilon(\hat{\mathbf{u}}_i, \hat{\mathbf{u}}_j, \hat{\mathbf{r}})(R^{-12} - R^{-6}), \tag{2.7}$$

The dependence of the width of the well depth on the molecular orientation with respect to the intermolecular vector was removed by choosing a shifted, rather than scaled, functional form to produce a Kihara-like potential, thus

$$R = \{r - \sigma(\hat{\mathbf{u}}_i, \hat{\mathbf{u}}_j, \hat{\mathbf{r}}) + \sigma_0\}/\sigma_0 \quad . \tag{2.8}$$

This was first suggested by Stone [7] and later employed by Gay and Berne in their model potential [6]. We should note that for the original Lennard-Jones potential, we get

$$R = \frac{r}{\sigma(\hat{\mathbf{u}}_i, \hat{\mathbf{u}}_j, \hat{\mathbf{r}})} . \tag{2.9}$$

The expression for the angular dependence of the conta ct distance is

$$\sigma(\hat{\mathbf{u}}_i\, \hat{\mathbf{u}}_j\, \hat{\mathbf{r}}) = \sigma_0 \left(1 - \chi \left\{ \frac{(\hat{\mathbf{u}}_i.\hat{\mathbf{r}})^2 + (\hat{\mathbf{u}}_j.\hat{\mathbf{r}})^2 - 2\chi(\hat{\mathbf{u}}_i.\hat{\mathbf{r}})(\hat{\mathbf{u}}_j.\hat{\mathbf{r}})(\hat{\mathbf{u}}_i.\hat{\mathbf{u}}_j)}{1 - \chi^2(\hat{\mathbf{u}}_i.\hat{\mathbf{u}}_j)^2} \right\} \right)^{-1/2} . \tag{2.10}$$

Here χ is the parameter defining the molecular shape anisotropy and is given by

$$\chi = \frac{\kappa^2 - 1}{\kappa^2 + 1} , \tag{2.11}$$

and κ is the ratio σ_e/σ_s of the contact distances σ_e and σ_s for the particles in an end-to-end arrangement and a side-by-side arrangement, respectively. It is apparent that for a sphere, χ equals 0, while for an infinitely long rod it is 1 and for an infinitely thin disk it is -1. The scaling parameter σ_0 is the contact distance for a pair of rods in a cross configuration. The well depth has also an angular dependence and was originally represented in the Berne-Pechukas potential (again derived from the Gaussian overlap model) as

$$\varepsilon(\hat{\mathbf{u}}_i\, \hat{\mathbf{u}}_j) = \varepsilon_0 \{1 - \chi^2(\hat{\mathbf{u}}_i.\hat{\mathbf{u}}_j)\}^{-1/2} . \tag{2.12}$$

In these expressions for the contact distance and well depth, the angular variation is contained in the three scalar products $\hat{\mathbf{u}}_i.\hat{\mathbf{u}}_j$, $\hat{\mathbf{u}}_i.\hat{\mathbf{r}}$ and $\hat{\mathbf{u}}_j.\hat{\mathbf{r}}$, which are simply the cosines of the angle between the symmetry axes of the two molecules and of the angles between each molecule and of the intermolecular vector. However, later it was realised that there were some unrealistic features associated with this form of the well depth. As can be seen from equation (2.12), the well depth has no dependence on the orientation of the molecules with respect to the intermolecular vector. This results in the unrealistic characteristic of the end-to-end and side-by-side orientations having equal well depths. Several workers in the field made contributions to modify the potential that was free from these unrealistic features [8]. The idea was to construct a new strength parameter to allow for the dependence of the well depth on the orientation of the molecules with respect to the intermolecular vector as well as on the relative orientation of the two particles. This form of the well depth suggested by Gay and Berne was

$$\varepsilon(\hat{\mathbf{u}}_i,\hat{\mathbf{u}}_j,\hat{\mathbf{r}}) = \varepsilon_0\,\varepsilon^{\nu}(\hat{\mathbf{u}}_i,\hat{\mathbf{u}}_j)\varepsilon'^{\mu}(\hat{\mathbf{u}}_i,\hat{\mathbf{u}}_j,\hat{\mathbf{r}}) \tag{2.13}$$

The first function $\varepsilon^{\nu}(\hat{\mathbf{u}}_i,\hat{\mathbf{u}}_j)$ is given in equation (2.12) and depends on only the relative orientation of the two particles. The second function $\varepsilon'^{\mu}(\hat{\mathbf{u}}_i,\hat{\mathbf{u}}_j,\hat{\mathbf{r}})$ is more involved and has much in common with that for the contact distance $\sigma(\hat{\mathbf{u}}_i,\hat{\mathbf{u}}_j,\hat{\mathbf{r}})$;

$$\varepsilon(\hat{\mathbf{u}}_i\,\hat{\mathbf{u}}_j\,\hat{\mathbf{r}}) = \left(1-\chi'\left\{\frac{(\hat{\mathbf{u}}_i.\hat{\mathbf{r}})^2+(\hat{\mathbf{u}}_j.\hat{\mathbf{r}})^2-2\chi'(\hat{\mathbf{u}}_i.\hat{\mathbf{r}})(\hat{\mathbf{u}}_j.\hat{\mathbf{r}})(\hat{\mathbf{u}}_i.\hat{\mathbf{u}}_j)}{1-\chi'^2(\hat{\mathbf{u}}_i.\hat{\mathbf{u}}_j)^2}\right\}\right), \tag{2.14}$$

where

$$\chi' = \frac{\kappa'^{1/\mu}-1}{\kappa'^{1/\mu}+1} \quad . \tag{2.15}$$

Here, κ' is the ratio $\varepsilon_s/\varepsilon_e$ which provides a measure in the anisotropy of the well depth, that is the attractive interaction for a pair of rods in a side-by-side, ε_s, and an end-to-end, ε_e, arrangement. In the limit that κ and κ' tend to unity, that is χ and χ' vanish, then the Gay Berne potential reduces to the Lennard-Jones potential.

Depending on the values of the parameters κ, κ', and the exponents μ and ν, different Gay-Berne potentials can be achieved, therefore, the notation GB(κ, κ', μ, ν) has been introduced [9] to distinguish between the different sets of parameters. In section 2.4.1, we shall explain how the values of these four parameters can be chosen to produce a potential suitable for the simulation of liquid crystals.

A graphical representation of the potential is helpful to appreciate the significance of the various terms occuring in it. This can be done by plotting the distance dependence of the potential for a particular orientation of the molecules. These representations are given for the Gay-Berne potential, GB(4.4, 20, 1, 1) in figure 2.3, with the two molecules in four different but characteristic relative orientations: side-by-side, end-to-end, side-to-end and the cross configuration.

From figure 2.3, it is apparent that the side-by-side is the most favourable arrangement since it gives rise to the lowest well depth. The attractive part of the potential becomes less pronounced when the rod-like particles are side-to-end and end-to-end, indicating a weak interaction for these arrangements as expected for real rod-like molecules. Similarly, the contact distance changes from a small value when the rod-like particles are arranged side-by-side to a larger value when they are arranged end-to-end, again as expected.

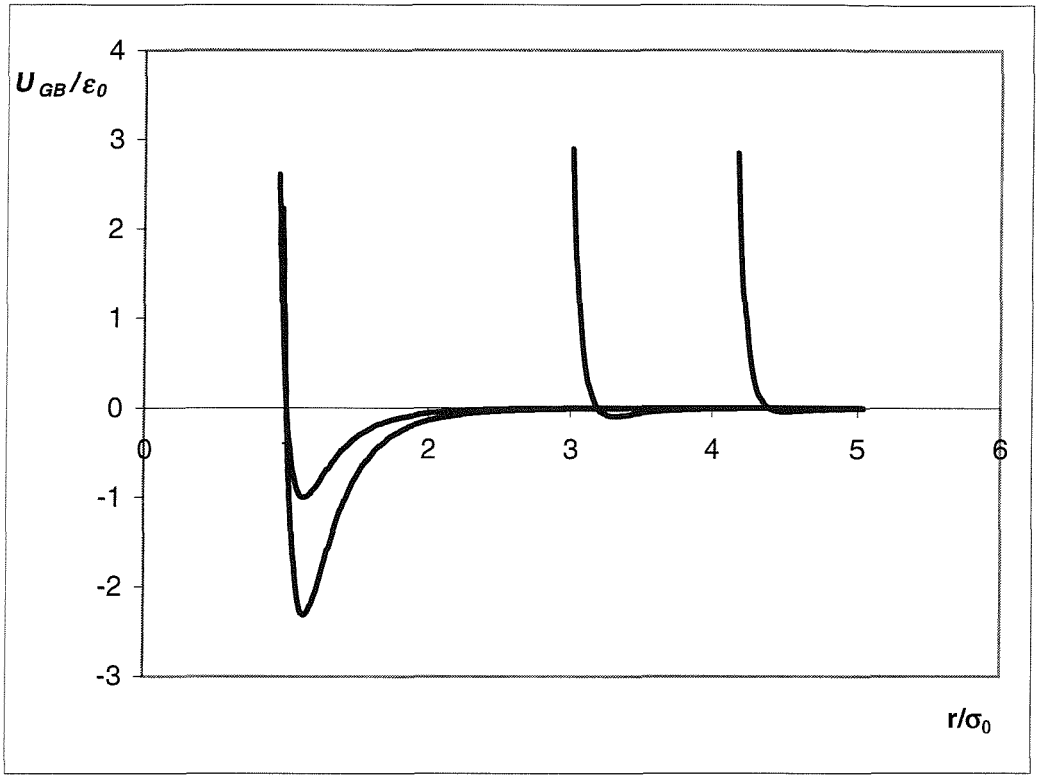

Figure 2.3 The distance dependence of the Gay-Berne potential for GB(4.4, 20, 1, 1) when the two molecules are in side-by-side, end-to-end, side-to-end and cross arrangements

An alternative representation of the potential is to plot the energy contours for a pair of molecules confined to a plane with a fixed relative orientation. The energy contours shown in figure 2.5 were produced by keeping one molecule, M1, fixed in an arbitrary frame with its centre of mass at the origin and its symmetry axis along the z axis, and moving the second molecule, M2, with its symmetry axis parallel to that of M1, see figure 2.4.

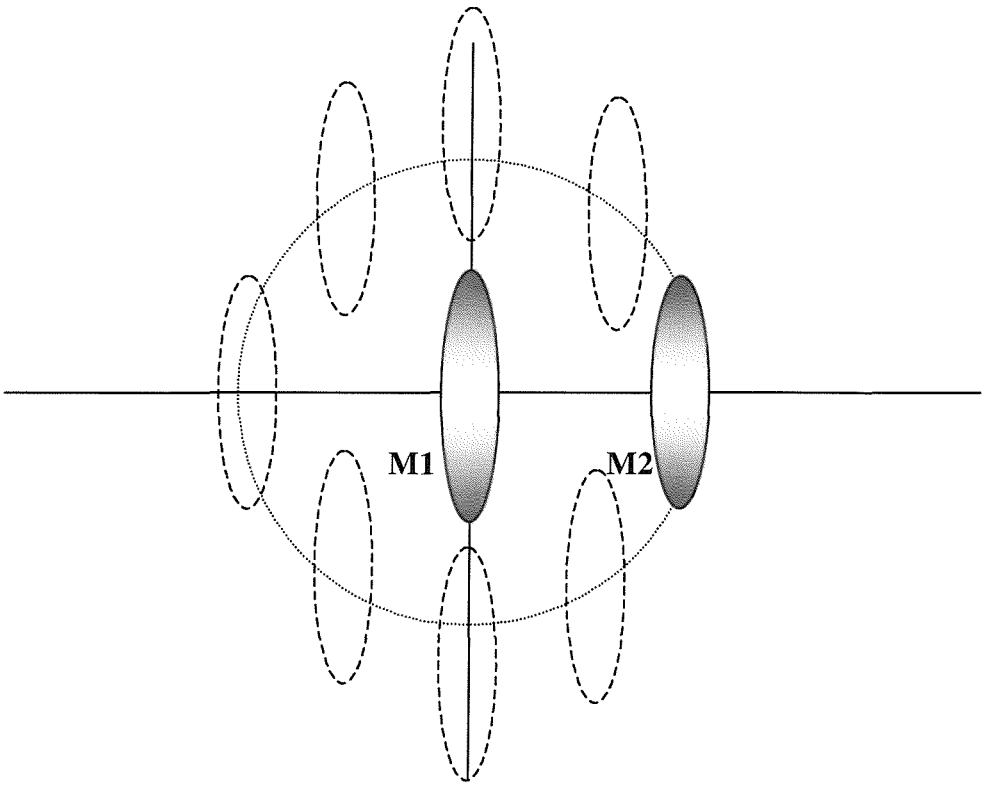

Figure 2.4 Moving M2 around M1 in a parallel arrangement.

The strong anisotropy in the attractive interactions is apparent from the contour plot with the low energy contours (blue in the plots) when the molecules are side-by-side but not end-to-end, see figure 2.5. For comparison, the energy contours for a pair of molecules produced from the Lennard-Jones potential is also given in figure 2.5 (d), where it can be seen that the energy contours for this potential are circular. This is due to the fact that in the Lennard-Jones potential, the energy is only a function of the separation between the two molecules. In the Gay-Berne potential however, the energy does depend on the orientation of the two molecules with respect to the intermolecular vector as well as their separation. Tracing the zero energy contour, (brown colour in the plots) which is the contact distance, it seems that the Gay-Berne molecules have an ellipsoidal shape. This

follows from the functional form of the contact distance σ and is explained in the Appendix. However, it should be noted that the shapes produced by such contours depend strongly on the relative orientations of the molecules, since different relative orientations produce different shapes, as we can see in figure 2.5. For example, when one molecule moves around the other in a T configuration (side-to-end), a circle is produced, analytically, and when the molecules are orthogonal to each other and the intermolecular vector, the zero energy contour suggests an ellipsoidal shape, but with a different ellipticity, than that for the parallel arrangement, see figure 2.5 (c), and Appendix. There are also some unrealistic features present in the inner regions of the energy contours which indicates that the molecules pass through each other, which is not physically reasonable, however, it can normally be ignored in simulations, since the molecules never come this close to each other. These features have been removed from figure 2.3 for clarity. We should also note that the scale in figure 2.5 is x2 and the distances are scaled with σ_0.

2.4.1 Parameterisation of the Gay-Berne potential

The Gay-Berne potential depends on four parameters, κ, κ', μ and ν, which determine the anisotropy in the repulsive and attractive forces as well as the two parameters σ_0 and ε_0 which scale the distance and energy, respectively. The choice of κ is relatively straightforward, as it is the length of the molecule divided by its width σ_e/σ_s, see equation (2.6). The determination of the other three parameters is not so obvious, and in their

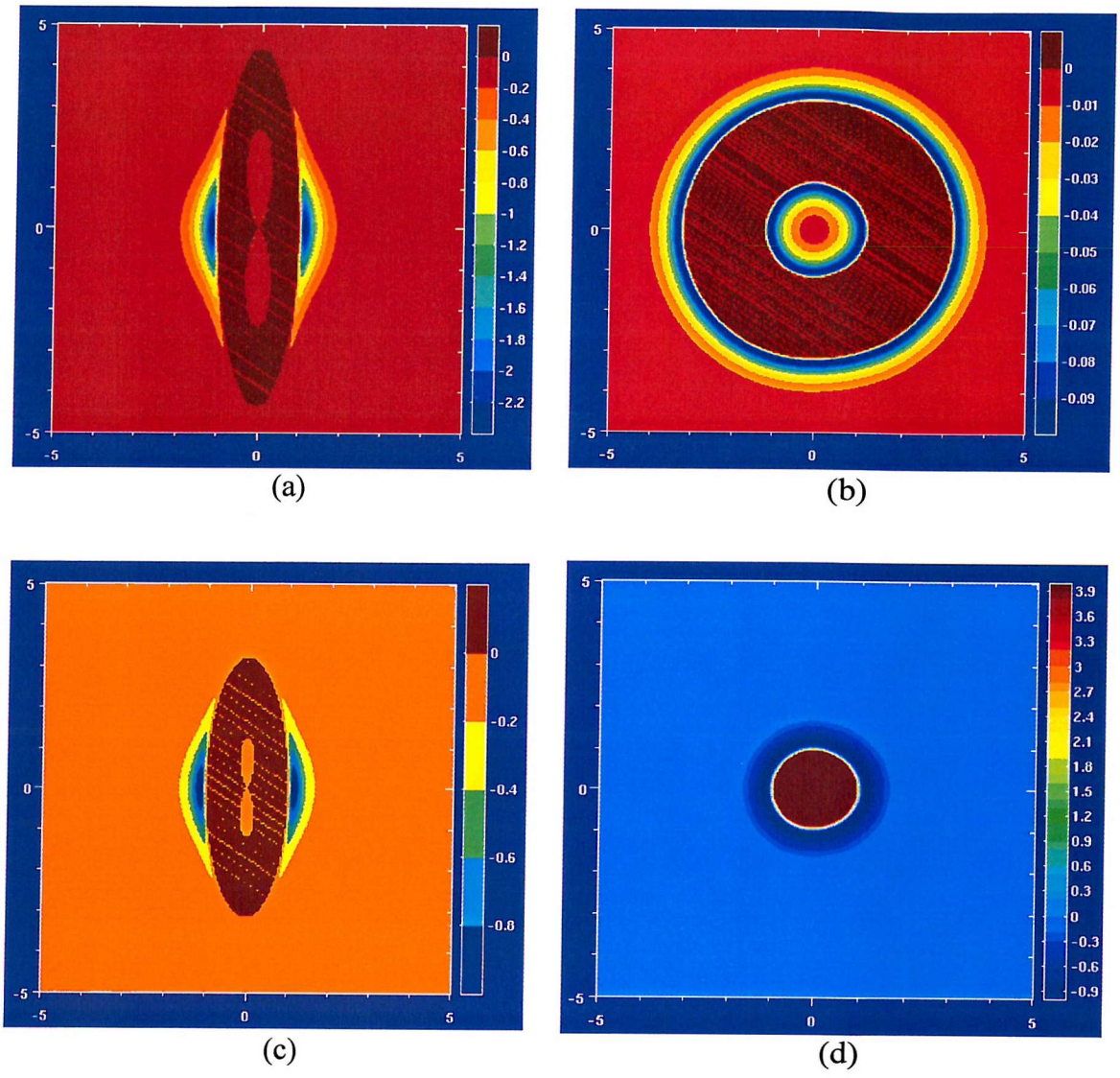

Figure 2.5 The energy contours for the Gay-Berne mesogen GB(4.4,20,1,1) for two molecules in (a) side-by-side (b) side-to-end and (c) cross configurations, in comparison with that (d) for a Lennard-Jones potential.

original work, Gay and Berne constructed an atomistic model of four Lennard-Jones centres in a line and mapped the Gay-Berne potential onto the interaction energy of two such arrays. This procedure gave $\kappa' = 5$, $\mu = 2$ and $\nu = 1$. The value for κ was chosen to be 3, since this is the minimum length-to-breadth ratio necessary to produce a liquid crystalline phase for real nematogens [4]. The shape of the Gay-Berne mesogen is ellipsoidal while that of four Lennard-Jones atoms is essentially a spherocylinder, see figure 2.5. This inconsistency prompted Luckhurst and Simmonds to use a more realistic atomistic model, onto which to map the Gay-Berne potential; they used the atomistic interaction between two *p*-terphenyl molecules [10]. Although this is not a liquid crystal at atmospheric pressure, it does have a virtual nematic-isotropic transition temperature of 360 K. For this, the values obtained were $\kappa = 4.4$, $\kappa' = 39.6$, $\mu = 0.80$ and $\nu = 0.74$. The length-to-breadth ratio is somewhat larger than the original value of 3, also μ and ν are different. However, the difference between the well depth ratio is far greater. The relation between the values for the parameters in the Gay-Berne potential and the structure of the phases formed is discussed in section 2.4.2.

2.4.2 Phase behaviour of Gay-Berne mesogen

One of the features of the Gay-Berne potential is the presence of anisotropic attractive forces which should favour the formation of anisotropic phases, in particular smectic phases because of the strong side-by-side interaction, see figure 2.3. As was mentioned earlier, the phases formed, depend strongly on the values of the four parameters κ, κ', μ

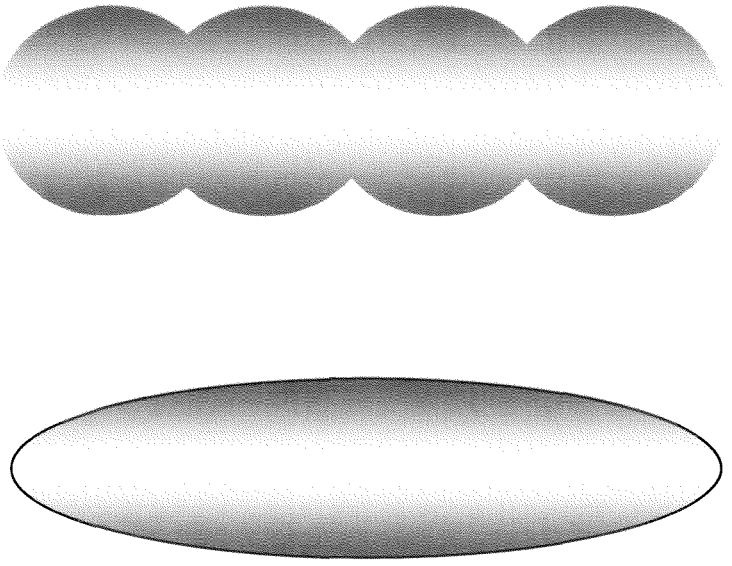

Figure 2.5 Comparison of the shape of four Lennard-Jones centres (essentially a spherocylinder) with that of a Gay-Berne mesogen which is an ellipsoid (only when probed by molecules in a parallel arrangement).

and ν as well as pressure and temperature. The parameter κ, which is the ratio of the end-to-end to the side-by-side contact distances, favours the parallel alignment of the particles and so aids liquid crystal formation. The parameter κ' favours the side-by-side arrangement over the end-to-end and so encourages the formation of the smectic phases. The other two parameters, μ and ν, also influence the formation of nematic and smectic phases. Extensive simulations has been performed to investigate the dependence of the phase behaviour of the Gay-Berne mesogens on the four parameters. The first of these simulations were done using the parameterisation proposed by Gay and Berne, thus Adams et al. [12] showed that GB(3.0, 5.0, 2, 1) exhibits nematic and isotropic phases.

However, the formation of the smectic phases were discovered [11] by studying a system of particles using molecular dynamics with the parameters GB(3.0, 5.0, 1, 2) in which the exponents μ and ν have been exchanged. The phases reported were isotropic, nematic, smectic A, smectic B and crystal as the temperature was lowered. de Miguel et al. [12] also performed a number of simulations to explore the influence of the well depth anisotropy parameter κ' on the phase behaviour while keeping the other Gay-Berne parameters fixed, that is the mesogens GB(3.0, κ', 1, 2), where κ' was assigned the values 1, 1.25, 2.5, 5, 10 and 20. The temperature for these simulations was fixed at 0.7 and the density was allowed to vary. It was found that when κ' is greater than, or equal to 5, the mesogen exhibited a smectic B and isotropic phases. This is the expected behaviour for large values of κ' which favours the side-by-side configuration. When κ' was less than 5, a nematic phase was also observed, although for κ' of 2.5 the nematic range was very short and for κ' less than 2.5, no smectic B phases were reported. More simulations were done using the parameters GB(4.4, 39.6, 0.8, 0.74) which were obtained by the fitting procedure developed by Luckhurst and Simmonds [10]. For this system, the mesogen was found to form isotropic, nematic and smectic A phases. The formation of the smectic A phase was somewhat unexpected since earlier results with other parameters gave only a smectic B phase. It was also found that even for κ' of 5.0, a smectic A was still formed which suggests its appearance is a consequence of the larger shape anisotropy, in this case $\kappa = 4.4$. To investigate this further, Bates and Luckhurst [9] performed simulations with parameters GB(4.4, 20, 1, 1) where now the value of κ' is halved, but as we have seen, this should not effect the formation of the smectic phases, and the exponents have been

set to unity, for convenience. The simulations were done at constant pressure and for low pressures, they found the system formed isotropic, smectic A and smectic B phases and at higher pressures, a nematic phase was also observed.

In this Chapter, we have discussed the essential elements required in the Corner potentials needed for the successful computer simulation of liquid crystals, namely the length-to-breadth ratio of particles, which normally needs to be greater or equal to 3, and the need for the interaction potential to possess anisotropic interactions both in the attractive and repulsive parts. For this to be possible, the potential has to depend on the relative orientations of the molecules and the intermolecular vector. We saw how the Gay-Berne potential facilitates these requirements, but it is not ideal for simulating particles with a range of anisotropic shapes. In the next Chapter, we shall introduce the use of S-functions to provide a functional form for σ and ε and will discuss how they can be used to generate different shape anisotropies. The contact distance and the well depth are defined in terms of S-functions and are used in the Corner potential to investigate the phase behaviour of different shapes using Monte Carlo simulations, the methodology of which is discussed in Chapter 4.

Chapter 3

S-function Corner Potential

3.1 Introduction

The Gay-Berne potential has been used in many simulations to help understand the liquid crystal behaviour for both calamitic and discotic systems. However, despite its many successes, the Gay-Berne potential is deficient when the shape of the molecule becomes a major concern, as the Gay-Berne molecules have an ellipsoidal shape, defined by zero energy contour, at least when probed by parallel molecules. It is believed that the shapes of molecules play an important role in determining the liquid crystal phases that are formed. Indeed hard particle simulations for ellipsoids and spherocylinders show very different phase behaviour [4]. Here, we use S-functions [7] to construct the parameters in Corner potential. The S-function expansion approach provides a way to model more closely, real nematogens, which are still anisotropic but not necessarily confined to a particular shape, as is the case for the Gay-Bern potential model. As we saw in the previous Chapter, from the expression for the contact distance, it can be seen that there is no simple modification of σ to produce different molecular shapes.

The energy, U, between two molecules of arbitrary shape can be expanded in terms of S-functions

$$U = \sum U_{L_1L_2J}(r) S_{L_1L_2J} \,, \tag{3.1}$$

where $U_{L_1L_2J}$ is a given as

$$U(\hat{\mathbf{u}}_1, \hat{\mathbf{u}}_2, \mathbf{r}) = 4\varepsilon(\hat{\mathbf{u}}_1, \hat{\mathbf{u}}_2, \hat{\mathbf{r}}) \left[\left(\frac{\sigma_0}{r - \sigma(\hat{\mathbf{u}}_1, \hat{\mathbf{u}}_2, \hat{\mathbf{r}}) + \sigma_0} \right)^{12} - \left(\frac{\sigma_0}{r - \sigma(\hat{\mathbf{u}}_1, \hat{\mathbf{u}}_2, \hat{\mathbf{r}}) + \sigma_0} \right)^{6} \right] . \tag{3.2}$$

The contact distance σ and the well depth ε are expressed in terms of S-functions,

$$\sigma(\hat{\mathbf{u}}_1, \hat{\mathbf{u}}_2, \hat{\mathbf{r}}) = \sum \sigma_{L_1L_2J} \, S_{L_1L_2J}(\Omega_1, \Omega_2, \Omega_{12}) \,, \tag{3.3}$$

and

$$\varepsilon(\hat{\mathbf{u}}_1, \hat{\mathbf{u}}_2, \hat{\mathbf{r}}) = \sum \varepsilon_{L_1L_2J} \, S_{L_1L_2J}(\Omega_1, \Omega_2\Omega_{12}) \,, \tag{3.4}$$

respectively. Here, $\sigma_{L_1L_2J}$ and $\varepsilon_{L_1L_2J}$ are the expansion coefficients and the angular dependence of $\sigma(\hat{\mathbf{u}}_1, \hat{\mathbf{u}}_2, \hat{\mathbf{r}})$ and $\varepsilon(\hat{\mathbf{u}}_1, \hat{\mathbf{u}}_2, \hat{\mathbf{r}})$ is described by $S(\Omega_1, \Omega_2, \Omega_{12})$, where, Ω_1 describes the orientation of molecule 1, Ω_2 describes the orientation of molecule 2 (both with respect to an arbitrary laboratory frame) and Ω_{12} describes the orientation of the intermolecular vector $\mathbf{r} = \mathbf{r}_2 - \mathbf{r}_1$. The indices L_1 and L_2 are positive integers and J takes values in the range $|L_2 - L_1|$ to $L_2 + L_1$.

The S-functions used in our simulations are listed below, where we have used the notation: $f_0 = \hat{\mathbf{u}}_1 \cdot \hat{\mathbf{u}}_2$, $f_1 = \hat{\mathbf{u}}_1 \cdot \hat{\mathbf{r}}$ and $f_2 = \hat{\mathbf{u}}_2 \cdot \hat{\mathbf{r}}$.

$$S_{000} = 1, \tag{3.7}$$

$$S_{202} = \{3f_1^{\,2} - 1\}/2\sqrt{5}, \tag{3.8}$$

$$S_{022} = \{3f_2^{\,2} - 1\}/2\sqrt{5}, \tag{3.9}$$

$$S_{220} = \{3f_0^{\,2} - 1\}/2\sqrt{5}, \tag{3.10}$$

$$S_{222} = \{2 - 3f_1^{\,2} - 3f_2^{\,2} - 3f_0^{\,2} + 9f_1 f_2 f_0\}/\sqrt{70}, \tag{3.11}$$

$$S_{224} = \{1 + 2f_0^{\,2} - 5f_1^{\,2} - 5f_2^{\,2} - 20f_0 f_1 f_2 + 35f_1^{\,2} f_2^{\,2}\}/4\sqrt{70}, \tag{3.12}$$

$$S_{404} = \{3 - 30f_1^{\,2} + 35f_1^{\,4}\}/24, \tag{3.13}$$

$$S_{044} = \{3 - 30f_2^{\,2} + 35f_2^{\,4}\}/24, \tag{3.14}$$

The value of S_{000} is a constant, since it does not depend on either the orientation of the molecules or the orientation of the intermolecular vector. The graphical representation of this S-function is given in figure 3.1 (a), which is just a circle of radius 1. In fact, when there is no dependence on the orientation of the intermolecular vector, for example S_{220}, the shape of the function will be a circle, see figure 3.1 (b). This S-function depends only on the orientation of the two molecules and has a maximum value of $1/\sqrt{5}$ when the two molecules are parallel, $(f_0 = 1)$, and a minimum value $-1/2\sqrt{5}$ when the two molecules are orthogonal, $(f_0 = 0)$.

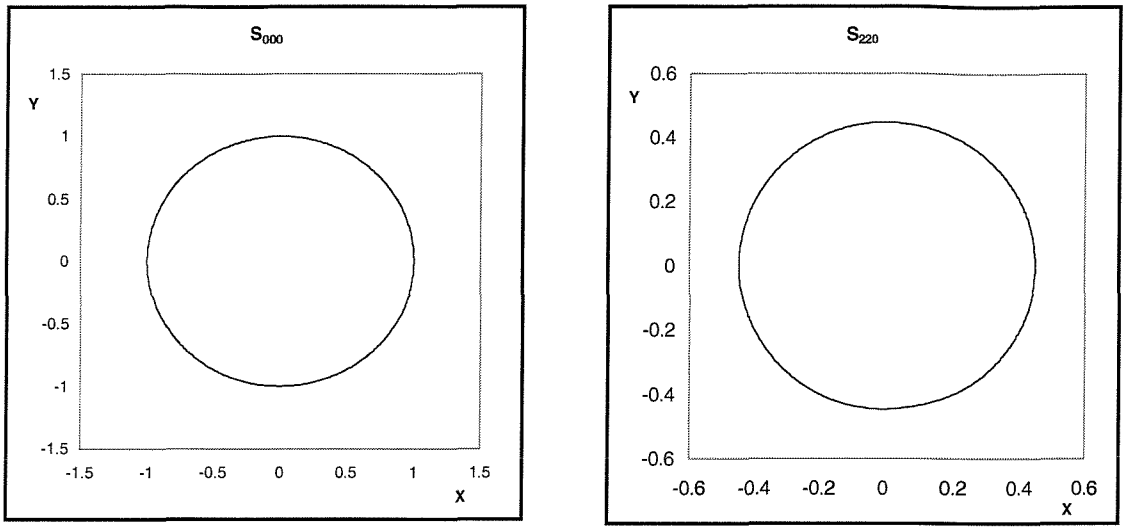

(a) (b)

Figure 3.1 The graphical representation of S_{000} and S_{220}, which are circular for parallel molecules.

In these plots, $\hat{\mathbf{u}}_1$ and $\hat{\mathbf{u}}_2$ both have components (0, 0, 1), so the dot product of the two is 1. One particle is always taken to define the origin. The x and z in the plots are the x and z components of the intermolecular vector in a Cartesian co-ordinate system

$$\hat{r} = \left(\frac{x}{\sqrt{x^2 + z^2}}, 0, \frac{z}{\sqrt{x^2 + z^2}} \right). \tag{3.15}$$

The S-function S_{202}, depends on the orientation of the first molecule and that of the intermolecular vector; similarly, the S-function S_{022}, depends on the orientation of the second molecule and the intermolecular vector. In fact S_{202} and S_{022} are the same since the intermolecular vector stays the same and molecules 1 and 2 are simply exchanged. The same is true for the S-functions S_{404} and S_{044}, as we can see in figure 3.3. The shapes for the S-functions S_{202} and S_{022} are given in figures 3.2(a) and 3.2(b), respectively. The S-

functions S_{222} and S_{224}, depend on the orientations of both molecules and the intermolecular vector. These are given in figure 3.2, (c) and (d).

The S-functions have some relationship to the atomic orbitals, for example, the shapes of S_{000} and S_{220} resemble the p orbitals, while the shapes of S_{202}, S_{022} and S_{222} resemble the shape of the d_{z^2} orbital

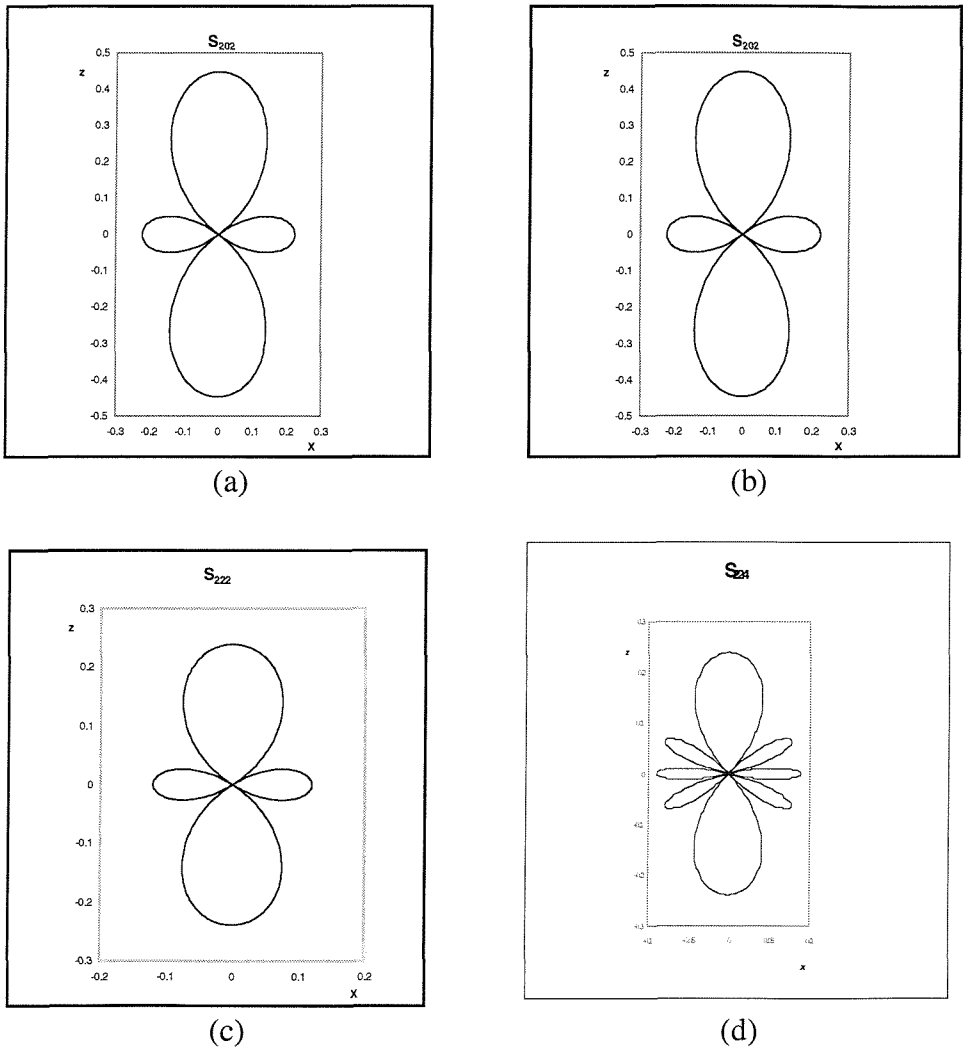

Figure 3.2 A graphical representation of S_{022}, S_{220}, S_{222} and S_{224}.

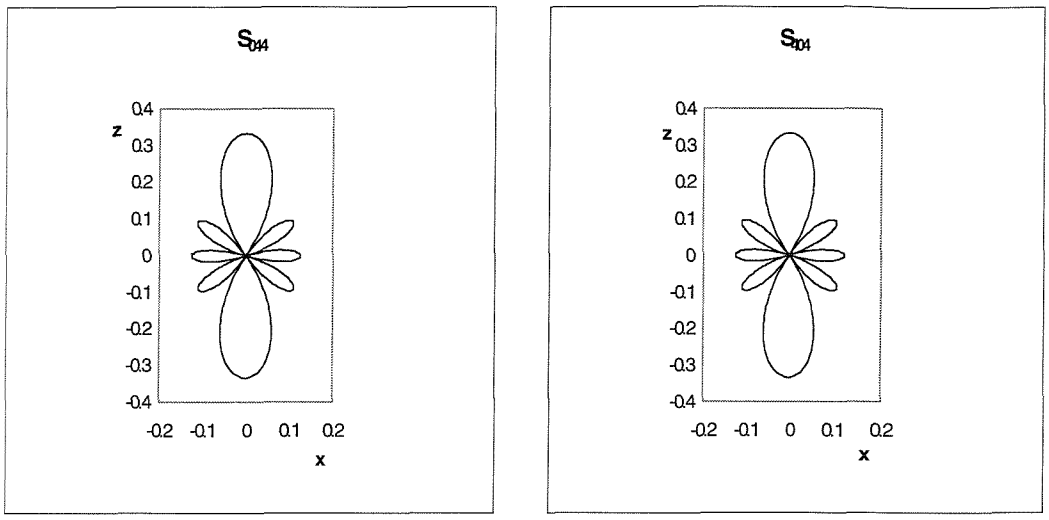

(a) (b)

Figure 3.3 A graphical representation of the S-functions (a) S_{404} and (b) S_{044}.

It is important to note that the S-functions can be positive or negative. This is indicated in the plots.

3.2 Determination of the expansion coefficients

The contact distance in the S-function notation is expanded as

$$\sigma(\hat{u}_1,\hat{u}_2,\hat{r}) = (\sigma_{000}S_{000} + \sigma_{202}S_{202} + \sigma_{022}S_{022} + \sigma_{220}S_{220} + \sigma_{222}S_{222} + \sigma_{224}S_{224}). \qquad (3.16)$$

Here we see some similarity between the S-functions and those used by Corner. However, here, the form of the range function, does not depend on the molecular geometry, in contrast to Corner's definition of the range parameter, where such a specific dependence was assumed. This is one of the reasons, that the Corner potential, although suitable for

small molecules, length less than 3, does not give correct results for anisometric molecules, i.e. with lengths greater than 3.

Our task was to determine the coefficients of the S-functions to achieve the shape required. This can be done in a number of ways:

a) to use a fitting procedure;

b) to determine the contact distance for various specific arrangements and derive the values by solving simultaneous equations, a limiting case of (a).

c) intuition / trial and error;

a) Fitting procedure

For the approximately uniform spherocylinder we used the coefficients previously obtained by Zewdie[13]. He used an iterative method of least-squares to determine the expansion coefficients of the S-functions for a rod-like particle (a sphero-cylinder where both ends are capped with a hemisphere of diameter 1) with a length to breadth ratio of 3 to 1 (see figure 3.3a) to mimic the shape anisotropy of a typical mesogenic molecule. He first identified a set of N configurations of the two molecules, although they were not defined, which were assumed to be important in contributing to the organisation of the particles in the liquid crystal phase. Then for each configuration, a corresponding minimum distance of approach, σ_i, between the pair of molecules was determined. The least-squares function χ_σ^2 was defined as

$$\chi_\sigma^2 = \sum_{i=1}^{N} w_i \left[\sigma_i - \sigma(\hat{\mathbf{u}}_1, \hat{\mathbf{u}}_2, \hat{\mathbf{r}})\right]^2 , \qquad (3.17)$$

where w_i is a weighting function for the ith configuration. Initially, w_i was set equal to unity for all the configurations and then the function (see equation (3.15)) was minimised with respect to the expansion coefficients by using a conjugate gradient method in a multidimensional space [14]. The coefficients for the contact distance were then estimated via equation (3.14) and compared with the numerically determined set of minimum distance approach, σ_i . The resulting geometry was plotted and compared against that of the reference molecules. Based on the quality of the fit against the original geometry, a decision was then made as to whether to include additional configurations, exclude some configurations or adjust the weights of the configurations. The whole process was then repeated to reminimise the least-square function with the new set of configurations and weighting functions.

b) Solving via simultaneous equations, limiting case of (a)

This method was used to determine the expansion coefficients for the spherocylinder with the small sphere in the middle. The initial step is the same as that used by Zewdie [13], but using far fewer configurations to achieve the desired shape. Five different configurations which were assumed to be important in contributing to the shape were identified. These were side-by-side (ss), end-to-end (ee), side-to-end (se), cross(x) and slipped parallel (sp), (see figure 3.4). We only considered five configurations, because there are just five terms to determine in the expansion, see equation (3.18).

For each configuration i, the contact distance σ_i was determined by measuring the centres of mass between two particles, and was substituted into the set of simultaneous equations to be solved:

$$\sigma_{ss} = \sigma_{000}S_{000} + \sigma_{202}S_{202} + \sigma_{022}S_{022} + \sigma_{220}S_{220} + \sigma_{222}S_{222} + \sigma_{224}S_{224} \quad , \tag{3.18}$$

with similar expressions for σ_{ee}, σ_{se}, σ_x and σ_{sp}. Using matrix notation the simultaneous equations can be written as

$$\begin{pmatrix} \sigma_{ss} \\ \sigma_{ee} \\ \sigma_{se} \\ \sigma_{x} \\ \sigma_{sp} \end{pmatrix} = \begin{pmatrix} S_{000}^{ss} & S_{202}^{ss} & \cdots & \cdots & S_{224}^{ss} \\ S_{000}^{ee} & S_{202}^{ee} & \cdots & \cdots & S_{224}^{ee} \\ S_{000}^{se} & S_{202}^{se} & \cdots & \cdots & S_{224}^{se} \\ S_{000}^{x} & S_{202}^{x} & \cdots & \cdots & S_{224}^{x} \\ S_{000}^{sp} & S_{202}^{sp} & \cdots & \cdots & S_{224}^{sp} \end{pmatrix} \begin{pmatrix} \sigma_{000} \\ \sigma_{202} \\ \sigma_{220} \\ \sigma_{222} \\ \sigma_{224} \end{pmatrix} . \tag{3.19}$$

The contact distances calculated for the reference shape were 2.0, 3.0, 2.5, 2.0 and 1.8 for the side-by-side, end-to-end, side-to-end, cross and slipped parallel configurations, respectively. These give

$$\begin{pmatrix} \sigma_{000} \\ \sigma_{202} \\ \sigma_{220} \\ \sigma_{222} \\ \sigma_{224} \end{pmatrix} = \begin{pmatrix} 1.00 & -0.448 & 0.447 & -0.120 & 0.090 \\ 1.00 & 0.894 & 0.447 & 0.239 & 0.239 \\ 1.00 & 0.894 & -0.224 & -0.120 & -0.120 \\ 1.00 & -0.448 & -0.224 & 0.239 & 0.030 \\ 1.00 & 0.478 & 0.447 & 0.127 & -0.032 \end{pmatrix} \begin{pmatrix} 2.0\sigma_0 \\ 3.0\sigma_0 \\ 2.5\sigma_0 \\ 2.0\sigma_0 \\ 1.8\sigma_0 \end{pmatrix} . \tag{3.20}$$

The evaluation of the inverse of the matrix in this equation produced the following set of coefficients:

$\sigma^*_{000} = 1.834$, $\sigma^*_{202} = 0.933$, $\sigma^*_{022} = 0.933$,

$\sigma^*_{220} = -0.658$, $\sigma^*_{222} = -0.678$, $\sigma^*_{224} = 3.301$.

where the asterisk indicates that the contact distances are scaled with σ_0. It is not easy to determine analytically how S-functions give a particular shape, especially if there are several S-functions that contribute to the shape of the particle. However, one can argue qualitatively what contribution each S-function make to the shape of the particle, by analysing the shape of each S-functions. For example, the S-function S_{202}, has positive lobes at each end and smaller negative lobes in the middle. If we combine this S-function with S_{000}, which is a sphere, one would expect to get a dumbbell shape, and the extent of the shape would depend on the coefficients of each S-function. This is both analytical and intuitive, however, when the number of S-functions in the term increases, then, it will not be so easy to say which S-functions, contribute to which part of the shape. The large value of coefficient σ_{224}, shows a large positive value, indicating the shape anisotropy to behave like a quadrupolar effect. Also the sign of the coefficients is of importance. We see from the coefficients that σ_{220} and σ_{222} have negative values. The negative values are thought to decrease the size of the positive lobes and to increase the size of the negative lobes. Also when we compare our coefficients, with those obtained by Zewdie [13], we see a similar pattern, in that both σ_{220} and σ_{222} are negative, and σ_{224} is relatively large and positive.

3.3 Shapes used in our simulations

In our simulations, we have used a combination of the S-functions, described in section 3.1, with appropriate coefficients to produce shapes comparable to those of real nematogens. Our aim was to simulate and investigate the phase behaviour of three different shapes:

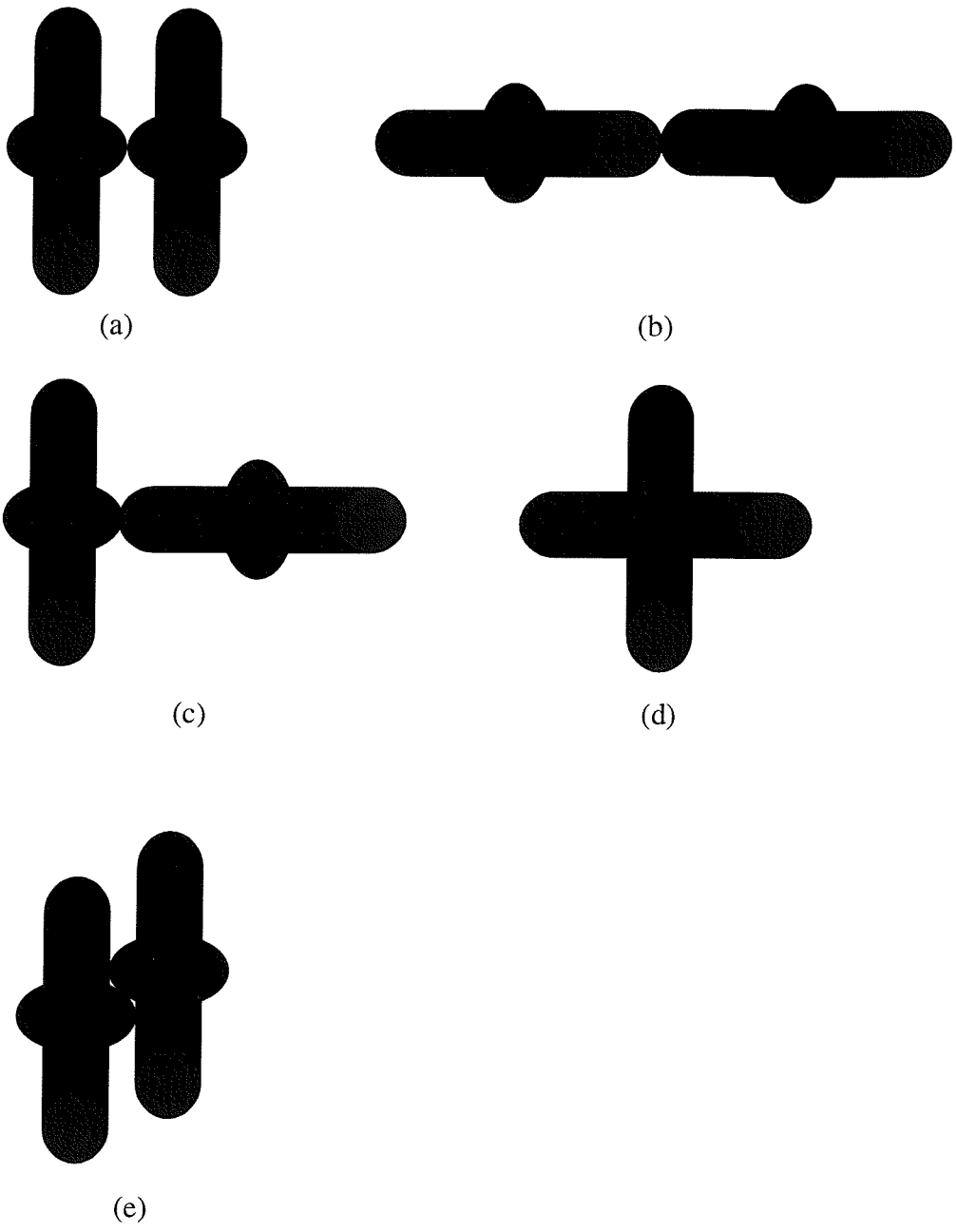

Figure 3.4 The arrangements used to obtain the contact distances for various arrangements, (a) side-by-side, (b) end-to-end, (c) side-to-end, (d) cross and (e) slipped parallel, all with length-to-breadth ratio of 3 to 1.

(i) a uniform spherocylinder,

(ii) a spherocylinder with a sphere in the middle of radius 1.75,

(iii) a spherocylinder with a sphere in the middle of radius 1.50,

all with the length to breadth ratio of 3 to 1 for the cylinder. The length of the cylinder is 2 plus two hemispheres at the each end of the cylinder with a diameter of 1, making the total length 3. The width of the spherocylinder is taken to be the width of the cylinder which is 1 and not the diameter of the sphere in the middle. These shapes, defined by the zero energy contour for two parallel molecules, together with their coefficients are shown in figure 3.5.

We have also plotted the energy potential as a function of the distance only, for each shape in four different arrangements: side-by-side, side-to-end, end-to-end and cross. The coefficients of the well-depth parameters used in calculating the potential energy were

$\varepsilon^*_{000} = 1.040, \quad \varepsilon^*_{022} = -1.404, \varepsilon^*_{202} = -1.404,$

$\varepsilon^*_{220} = 2.199, \quad \varepsilon^*_{222} = -0.722, \varepsilon^*_{224} = -0.132.$

where the asterisk indicates that the well-depths are scaled with ε_0. We used the same values for the well-depth parameters as used by Zewdie so that we could compare the effect of the shape of the particles with the same well depth parameters.

For the uniform spherocylinder, see figure 3.6(a), the scaled contact distances for the side-by-side and cross configurations are 0.99 and 1.045, almost close to 1.0. The scaled contact distances for the side-to-end, obtained as the average of the end-to-end and side-by--side contact distances, is 1.92, a little less than the expected value of 2.0, (3+1)/2, and for the end-to-end is 3, as expected. For the spherocylinder with a sphere of radius of 1.50, the contact distances for the side-by-side and the cross configurations are 1.5, as expected,

for the side-to-end it is 1.87 instead of the expected value of 2.25, that is (3+1.5) / 2, and for the end-to-end it is 3, again as expected.

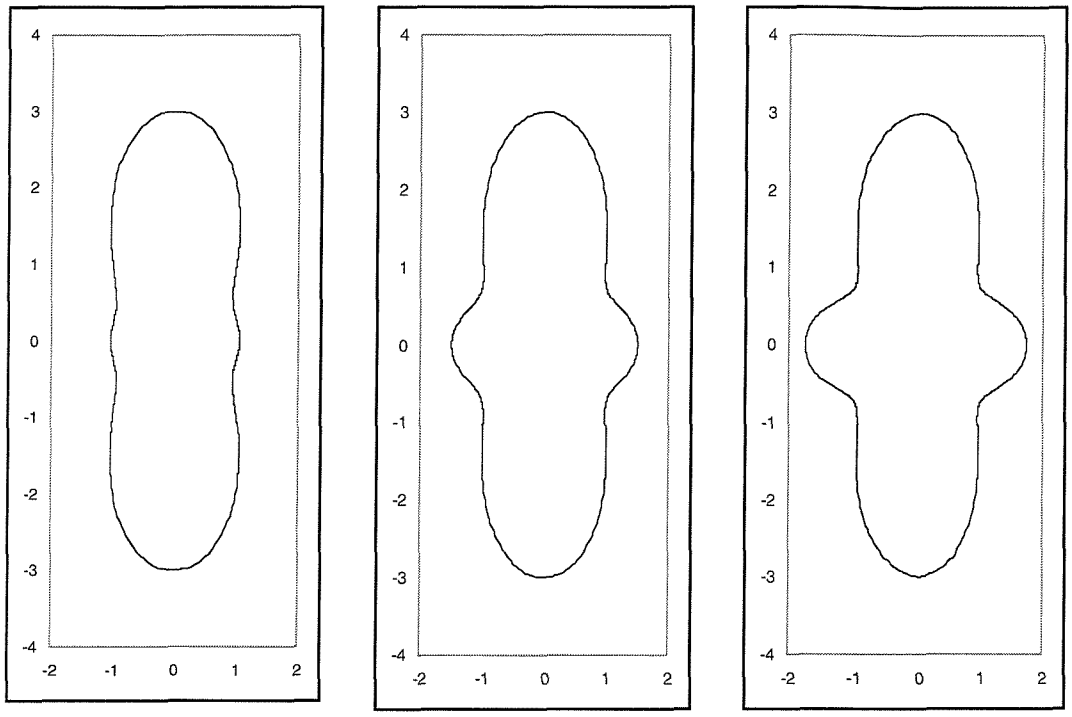

(a) (b) (c)

	σ^*_{000}	σ^*_{202}	σ^*_{022}	σ^*_{220}	σ^*_{222}	σ^*_{224}	σ^*_{404}	σ^*_{044}
(a)	**1.641**	**1.436**	**1.436**	**-0.599**	**-0.885**	**2.323**	------	------
(b)	**1.834**	**0.933**	**0.933**	**-0.657**	**-0.678**	**3.301**	------	------
(c)	**2.320**	**1.000**	**1.000**	**-1.599**	**-1.885**	**1.000**	**1.050**	**1.050**

Figure 3.5 The shapes used in our simulations, together with the coefficients that were used to construct them.

However, for the spherocylinder with a sphere in the middle of radius 1.75, we notice that only the contact distances for the side-by-side and end-to-end are correct, i.e. 1.75 and 3.0, respectively, but the values for the contact distances for the cross and side-to-end are not as expected. The values are 2.07 for cross and 3.48 for side-to-end instead of the expected values of 1.75 and 2.375 for cross and side-to-end, respectively. However, these arrangements are not important within the liquid crystal phases and so can be ignored.

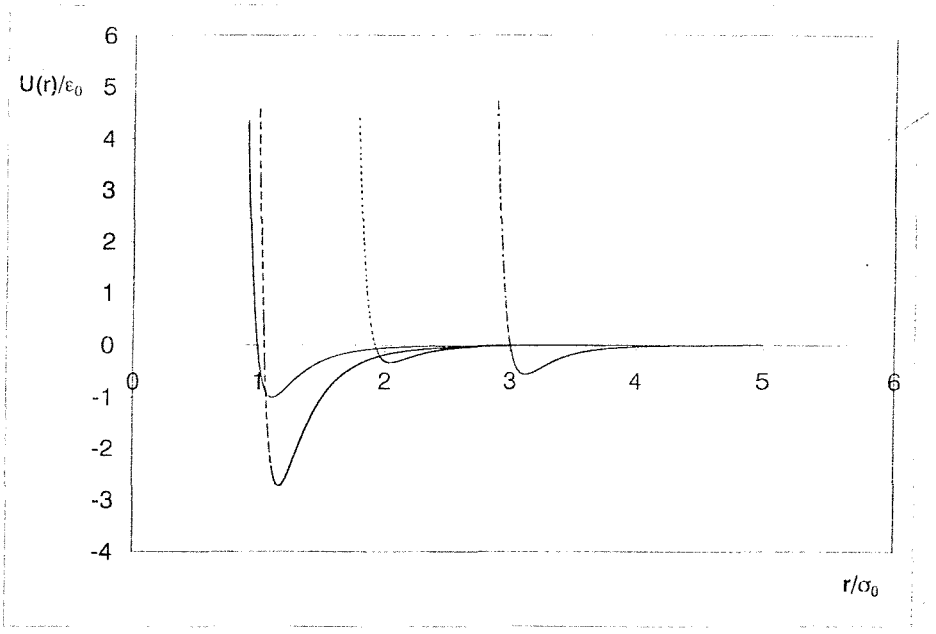

(a)

Figure 3.6(a) The energy plots for side-by-side (——), side-to-end (– – – –), cross (-----) and end-to-end (— - —) arrangements for the uniform spherocylinder.

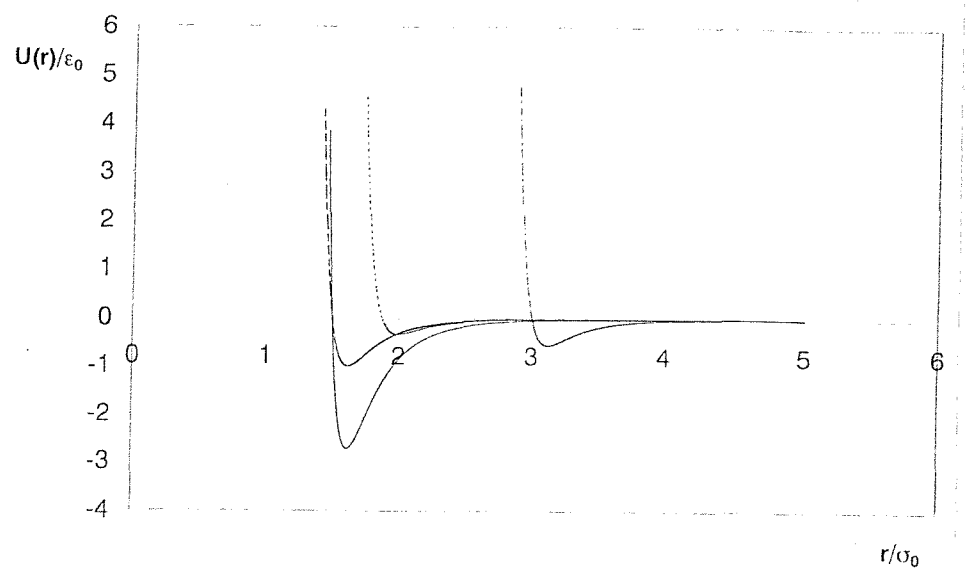

(b)

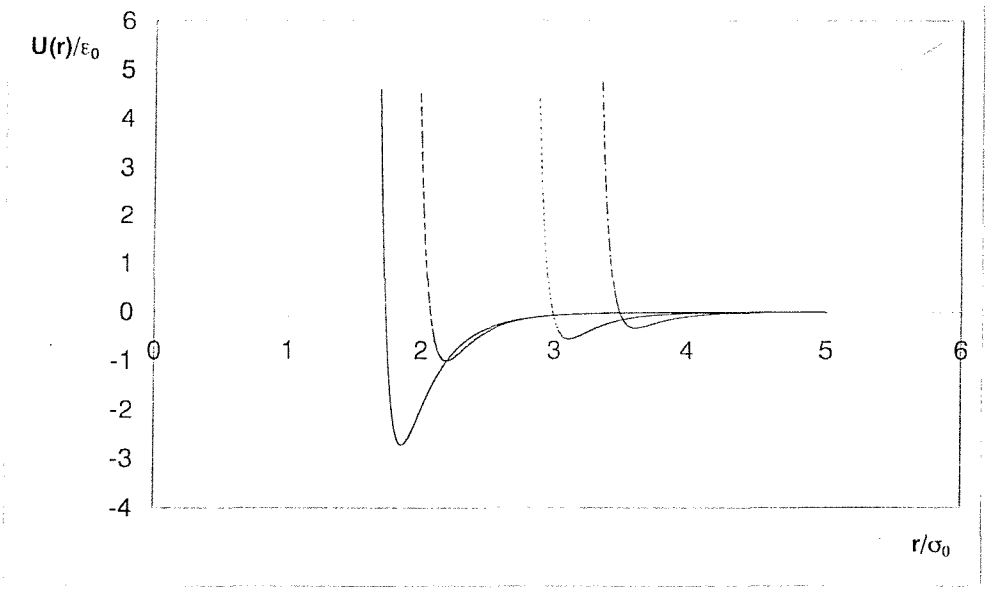

(c)

Figure 3.6 The energy plots for side-by-side (——), side-to-end (– – – –), cross (- - - -) and end-to-end (— - —) arrangements for (b) spherocylinder with a central sphere of radius 1.5 and (c) the spherocylinder with a central sphere of radius 1.75.

(a)

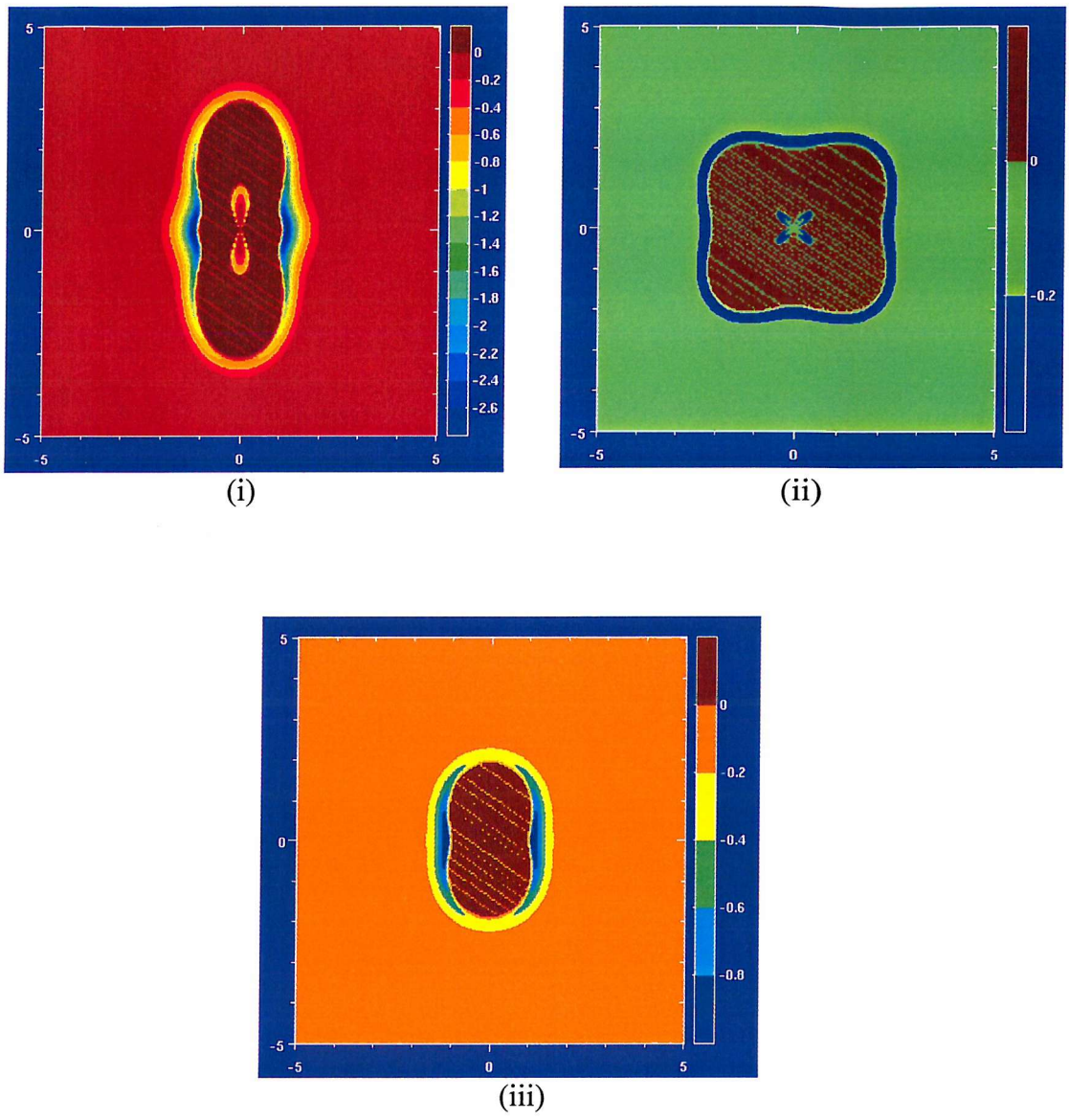

Figure 3.7(a) The energy contours for (i) parallel, (ii) side-to-end and (iii) cross configurations for the uniform spherocylinder.

(b)

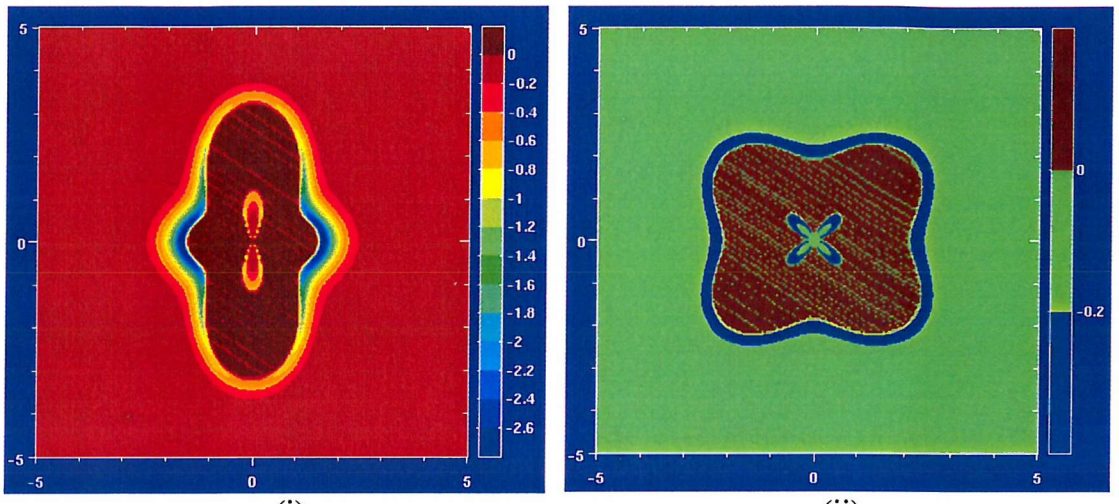

(i)

(ii)

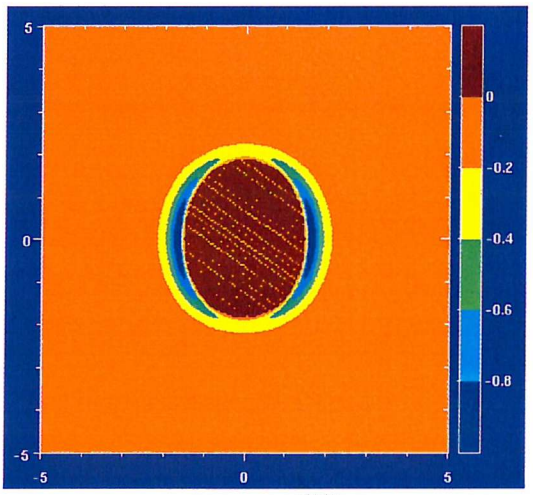

(iii)

Figure 3.7(b) The energy contours for (i) parallel, (ii) side-to-end and (iii) cross configurations for spherocylinder with a small central sphere.

(c)

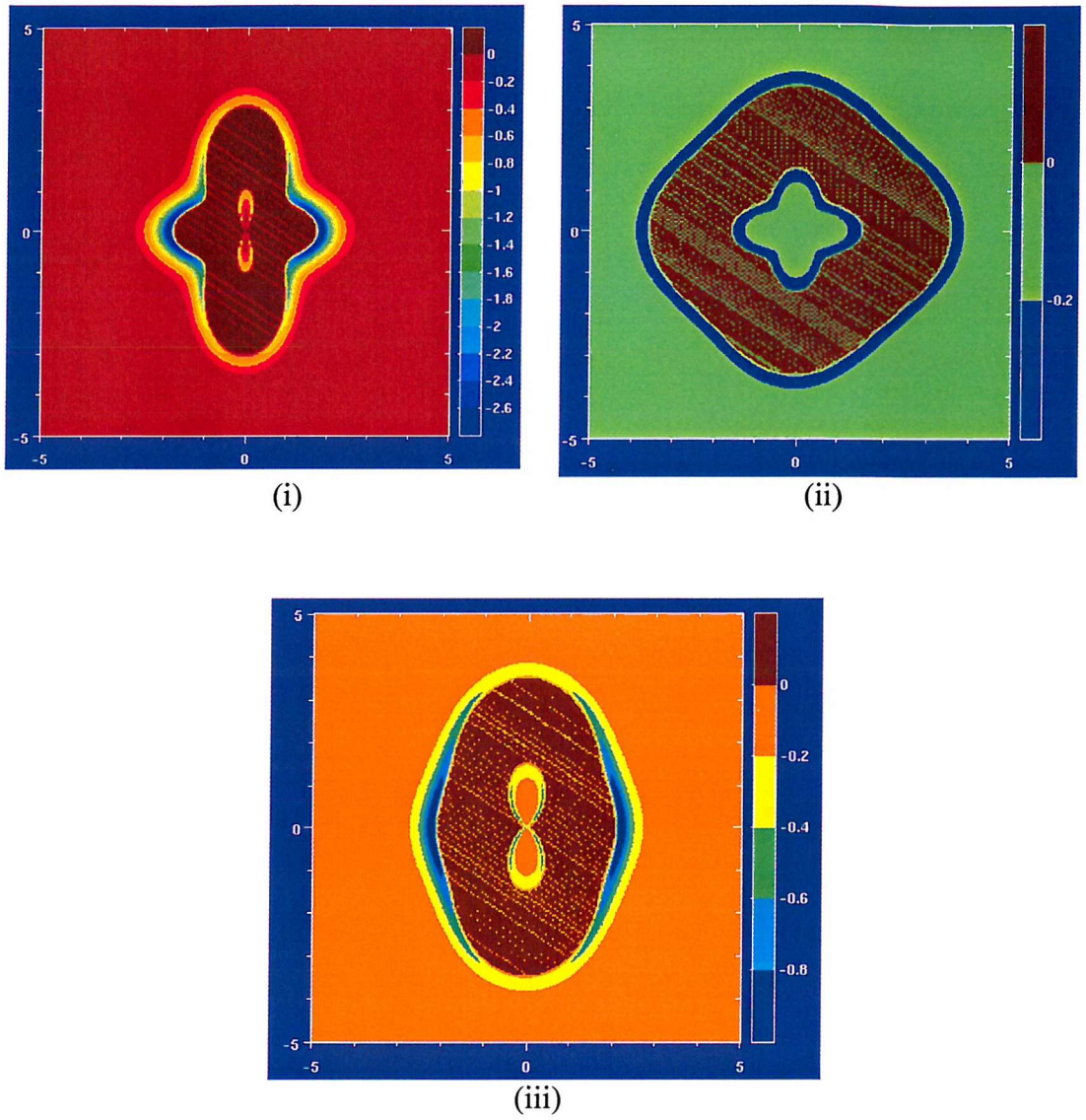

Figure 3.7(c) The energy contours for (i) parallel, (ii) side-to-end and (iii) cross configurations for the spherocylinder with a large central sphere.

We also compared our model potential against that of a multi-site Lennard-Jones potential constructed to give an analogous shape. This involved setting up an array of eight neon atoms and a xenon atom placed at the centre, see figure 3.8. The reason for this choice of atoms was because the ratio of the contact distances Ne:Xe is 1:1.45 which is close to the dimensions of the spherocylinder with the small sphere of radius of 1.50 at its centre. The contact distance and the well depth for xenon and neon atoms are

Ne: $\sigma = 279\text{pm}$ $\varepsilon/k_B = 35.7\text{K}$

Xe $\sigma = 229\text{pm}$ $\varepsilon/k_B = 406\text{K}$

We set up two such atomic arrays, see figure 3.8, in a common Cartesian coordinate system to evaluate the pair potential. There are some ripples on the surface, because of the small number of atoms that we used obtain a smoother surface, we would need to use a large number of neon atoms. However, since our main concern was to see the effect of the xenon in the middle of the array, then for our purpose, eight neon atoms were considered to be enough. One molecule was fixed with the xenon atom at the origin and the neon atoms along the z-axis of the coordinate system, and both linear arrays were kept parallel. The other array was allowed to move, in the same fashion as described in figure 2.4 (see Chapter 2), to produce the energy contours which are shown in figure 3.9. The total potential energy was calculated by summing over all the pairwise interactions, for the atoms in different arrays,

$$U_{tot} = \frac{1}{2}\sum U_{pairs} \,. \tag{3.21}$$

The factor 1/2 was used to avoid inclusion of the same pairs of atoms twice. The energy for a pair of atoms was calculated using the Lennard-Jones potential

$$U_{ij} = 4\varepsilon_{ij}\left\{\left(\frac{\sigma_{ij}}{r}\right)^{12} - \left(\frac{\sigma_{ij}}{r}\right)^{6}\right\}, \tag{3.22}$$

where i and j denote the pairs, Ne-Ne, Ne-Xe and Xe-Xe, but in different arrays. For the interaction between two neon atoms or two xenon atoms we used the values for the contact distance and well depth given previously. For the interaction between a neon atom with a xenon atom, we used the Lorentz-Berthelot combining rules to obtain the values for the contact distance and well depth. That is the contact distance, σ_{NeXe}, is the arithmetic mean of σ_{Ne} and σ_{Xe}

$\sigma_{NeXe} = (\sigma_{Ne} + \sigma_{Xe}) / 2$,

and the well depth, ε_{NeXe}, is the geometric mean of ε_{Ne} and ε_{Xe}

$\varepsilon_{NeXe} = \sqrt{(\varepsilon_{Ne}\varepsilon_{Xe})}$.

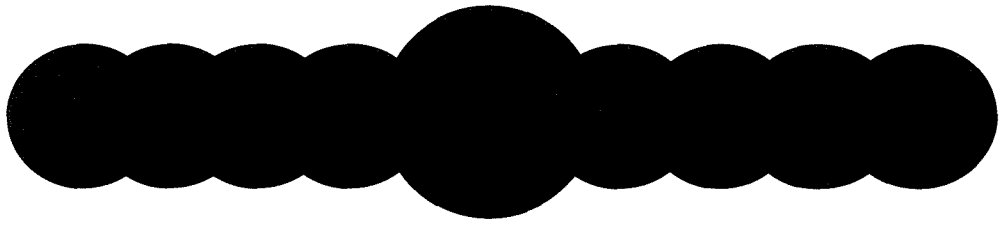

Figure 3.8 A representation to mimic the shape of the spherocylinder with a small sphere in the middle, using eight neon atoms and a single xenon atom as the small sphere.

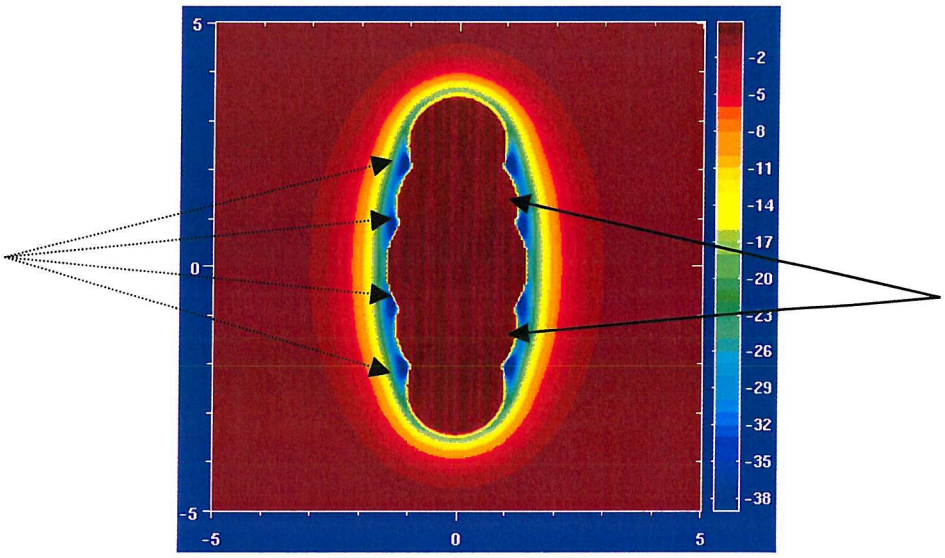

Figure 3.9 The energy contours of the multi-site potential for the parallel configuration of the two molecules.

From the energy plot shown in figure 3.9, two features are immediately apparent. First, we notice that there are extra bumps (indicated by the solid arrows) below and above the original central bump. Secondly, we notice that the minima of the potential (indicated by the dotted arrows) form below and above each bump, and not on the sides of the middle bump, as compared with the previous energy contours for side-by-side arrangement when the well-depth function was fitted to the Gay-Berne potential.

The former difference is almost certainly due to the fact that we did not include a second slipped parallel configuration (see figure 3.10(b)) when calculating the contact distances,

which is important and could make a major contribution in determining the shape of the molecule.

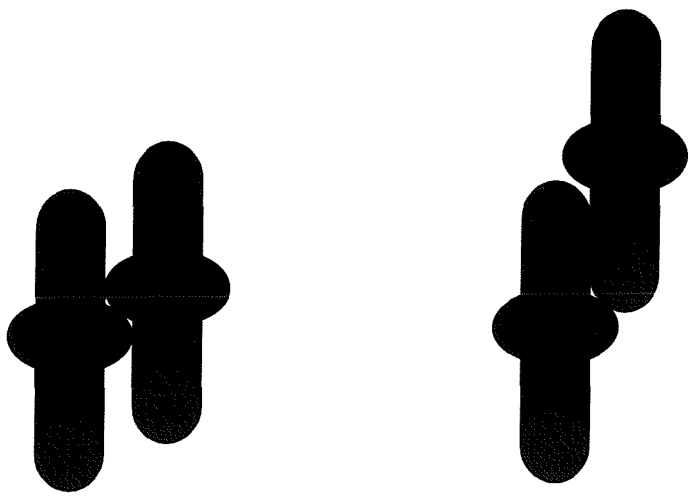

(a) (b)

Figure 3.10 Two possible slipped-parallel arrangements for the spherocylinder with a sphere in the middle.

The latter difference can be justified since we used the same values for the well depth as that employed by Zewdie to favour the side-by-side arrangement of molecules, and not another set of values to favour the slipped parallel configuration of the molecules, as suggested by the energy contour diagram. Since our primary interest was in seeing the effect of the shape on the phase behaviour of mesogenic molecules, then we only varied the sigma coefficients, to produce different shapes, while the epsilon coefficients were taken to be the same for all of the three shapes.

In the next Chapter, we shall see that in fact for the spherocylinders with a sphere in the middle, the slipped parallel arrangement of molecules is greatly favoured over the side-by-

side arrangement, even though the epsilon values used predominantly favour the side-by-side arrangement.

If the project was to be repeated with the same shape, namely a spherocylinder with a central sphere, both possible slipped parallel configurations should be included , instead of a less important arrangement, say the cross or side-to-end arrangements, which are unlikely to occur in a liquid crystal phase. Also, it may even be possible to use the S-function expansion approach to determine coefficients which fit the true well-depth, which is shown in figure 3.9. However, that may require more S-functions with higher ranks.

Chapter 4

Computer Simulation

4.1 Introduction

The interaction potentials define the microscopic properties of the constituent particles and in the last two Chapters, our main concern was to develop model potentials with which to describe how mesogenic particles interact at the molecular level; these were described in terms of molecular pair potentials. The next step is to see how, from a given pair potential, we can determine the behaviour of the bulk system, and the answer lies in statistical thermodynamics which provides the link between the microscopic properties of matter and its bulk properties. At the heart of statistical thermodynamics, lies the concept of the Boltzmann distribution which is concerned with the population of the atomic or molecular energy states. All information regarding the energetic states of a physical system is contained in the partition function Q,

$$Q = \int \exp\left[-U(\{X^N\})/k_B T\right]\{dX^N\}, \tag{4.1}$$

where X denotes the set of coordinates for all of the particles contained in the system, and k_B is the Boltzmann constant. Once Q is known, then any thermodynamic observable can be calculated, since the molar Helmholz free energy is related to Q via

$$A = -RT \ln Q . \tag{4.2}$$

The equations used in statistical thermodynamic are clearly complex in nature for condensed phases because $U(\underline{X}^N)$ is dependent on the coordinates of all the constituent particles. One way of evaluating such equations is by numerical methods which require time, effort and most importantly accuracy. There are two major techniques used in computer simulation, these are Monte Carlo and molecular dynamics [15] and they are now widely used and have proved to be of great importance in understanding the behaviour of liquid crystals, especially at the molecular level.

In this Chapter, we shall see how thermodynamics together with the appropriate choice of a model potential can be implemented in a Monte-Carlo programme. First, we describe the techniques of Monte-Carlo simulation. Then, the concept of the periodic boundary conditions, and why they are necessary in computer simulation. The thermodynamic and structural properties required to characterise a phase are introduced and described in section 4.4. The results available from our Monte Carlo simulations are discussed in Chapter 5.

4.2 Monte Carlo simulations

The Monte Carlo computer simulation technique is a probabilistic method for the evaluation of multi-dimensional integrals by the use of random numbers. It is done by

integrating over a set of points chosen randomly throughout the relevant region of phase space. In the Monte Carlo method, the algorithm has no connection with real time and the bulk thermodynamic observables are calculated from a sample of molecules by taking the appropriate ensemble averages, which is NPT or isothermal-isobaric ensemble.

We consider a system containing N particles. Then, any time-independent average property can be written as

$$\langle A \rangle = \int A\{X^N\} P\{X^N\} \{dX^N\}, \tag{4.3}$$

where $A\{X^N\}$ is a function of the X^N variables, defining the positions of all N particles, with X being the six positional and orientational coordinates (r, Ω) for a given particle. In general, the integral is evaluated over all positions and orientations. The probability density function $P(\{X^N\})$, gives the probability of finding the N particles in positions X^N; it is related to the potential energy by the Boltzmann expression

$$P\{X^N\} = Q^{-1} \exp\left[-U(\{X^N\})/k_B T\right], \tag{4.4}$$

where Q is the partition function and is given in equation 4.1.

In order to evaluate the integral in equation 4.3 numerically, one might randomly generate $\{X^N\}$ with a uniform distribution throughout phase space and then calculate the average over m samples as

$$\langle A \rangle_m = \sum_{k=1}^{m} A(\{X^N\}_k)\, P(\{X^N\}_k) . \tag{4.5}$$

However, there is a problem associated with this method in that $<A>_m$ might take a long time to converge since for many regions of phase space $P(X^N)$ is very small. Also a great deal of computer resource might be consumed in calculating $A(\{X^N\})$ outside of regions of interest, i.e. when two molecules are at a very long distance from each other so their

interaction can be neglected. Another problem is that for an accurate evaluation of $P\{m\}$, m has to be very large to include all possible states or at least a realistic sample of them. To overcome this problem of evaluating $<A>_m$ effectively, the method of importance sampling is employed so that configurations $\{X^N\}_k$ are chosen randomly but with a distribution $P\{X^N\}$ to ensure that for the relatively limited number of samples available in the simulation, the most representative regions of phase space are sampled most frequently.

The Metropolis sampling scheme

Metropolis, Rosenbluth, Rosenbluth, Teller and Teller [15] devised a method in which both conditions of importance sampling and Markov-chain processes are satisfied. This is the method used extensively in computer simulation in investigations of fluids and liquid crystals. Although each MC programme is tailored for specific application, the core algorithm used is essentially the same in every case. The Metropolis scheme is performed in a sequence of the following steps:

1. Set up an initial configuration, $\{X^N\}_0$.
2. Select a particle i at random, or sequentially, at position r and orientation Ω and calculate its energy $\sum_j U_{ij}(r,\Omega)$.

3. Move the chosen particle from its current position and orientation by some small random displacement which we show symbolically as $r' = r + \Delta r$ and orientation $\Omega' = \Omega + \Delta\Omega$ and calculate its new energy $\sum_j U'_{ij}(r', \Omega')$.

4. If the energy at the new position is more stable than the old position, i.e. if $U_i'(r', \Omega') < U_i(r, \Omega)$ then accept the move.

5. If the energy at the new position is less stable than the old position, i.e. if $U_i'(r', \Omega') > U_i(r, \Omega)$ then calculate $P = exp(-\Delta U / k_B T)$, where $\Delta U = U'_i - U_i$, and generate a random number in the range $0 < Rand < 1$.

6. If $Rand < P$ then accept the move,

   if $Rand > P$ then reject the move and restore the old configuration, *i*.

7. Repeat (from step 1). Until the requested number of cycles has been performed and gives configurations with probability equal to Boltzmann distribution.

Ensembles

A typical Monte Carlo simulation involves a number of particles *N*, normally a few hundred to a few thousand. Thermodynamic variables such as temperature, pressure, volume or energy can be either fixed in value or allowed to vary. The most common ensembles are

(i) isothermal-isobaric (*NPT*) in which temperature, pressure and the number of particles are fixed and the volume is allowed to vary,

(ii) canonical (*NVT*) in which temperature, volume and the number of particles are fixed and the pressure is allowed to vary,

(iii) microcanonical (*NVE*) in which volume and energy are fixed and the temperature is allowed to vary.

There are advantages and disadvantages associated with different ensembles. For example, in constant volume simulations the structure of the ordered phases such as smectics may not fit exactly to the dimensions of the simulation box, since the dimensions of the box are not allowed to change. Another problem associated with constant volume simulations is that low temperature phases which normally have a higher density than the high temperature phases, may have cavities in the simulation box at low temperature. Constant pressure simulations overcome these problems in principle by allowing the dimensions of the box to change to compensate for the change in volume of the system. Also, most experiments on liquid crystals are performed at constant pressure, rather than constant volume, and so the, isothermal-isobaric ensemble resembles, more closely, the experimental conditions. In our simulations, the number of particles was 2000 and we used isothermal-isobaric Monte Carlo simulation. For constant pressure simulations, where the box size is allowed to change, the change in the free energy is calculated by

$$\Delta U + p\Delta V + RT\ln(V_2/V_1)\ . \qquad (4.6)$$

where $\Delta U + p\Delta V$ is associated with change in enthalpy and $RT\ln(V_2/V_1)$ is associated with change in entropy.

4.2.1 Acceptance / Rejection Ratio

During the Monte Carlo simulation, particles undergo a trial change in their positions and orientations. As we have seen, this changes the energy of the system. The probability of accepting a trial move is $\exp(-\Delta U/k_B T)$. In general if the displacement is very large, then it is likely that the particle moves from a stable configuration to an unstable configuration and so the move will be rejected. If, however, the displacement is very small, the change in energy will be negligible and virtually all of the moves will be accepted. Neither case is ideal, since the system will then take an infinite time to reach equilibrium. The maximum displacements can be chosen (as we shall see in the following subsection) so that the number of accepted configurations are approximately equal to the number of those rejected. This seems reasonable since if all the moves are rejected, then the system dosenot move and if all the moves are accepted, then the particles only move short distances and the system barely changes.

4.2.2 Trial moves

a) Translational moves

The coordinates of a molecule i in a Cartesian coordinate system are given by (x_i, y_i, z_i). A random translational move is performed on a molecule by taking the old components of $\underline{r}$ and adding a random displacement to them, so that the new coordinates of the molecule become

$$x_{new} = x_{old} + \delta_{max}\,(2 * Rand - 1.0),$$

$$y_{new} = y_{old} + \delta_{max}\,(2 * Rand - 1.0),$$

$$z_{new} = z_{old} + \delta_{max}\,(2 * Rand - 1.0), \qquad (4.7)$$

where δ_{max} is the maximum translational displacement. This is included in the equations to control the acceptance / rejection ratio and also provide control over the movements. *Rand* is a random number in the range $0 < Rand < 1$ and is used as $(2 * Rand - 1.0)$ in order to produce random numbers in the range $-1.0 < Rand < 1.0$ so that the translational moves can be in all directions.

b) Rotational moves

In three dimensions, the orientation of a cylindrically symmetric particle can be expressed by the spherical polar coordinates, β and α, see figure 4.2

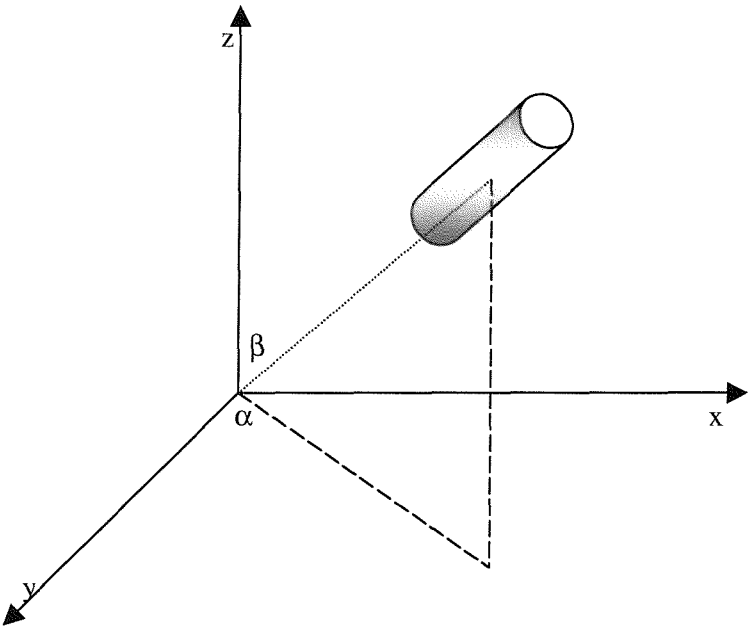

Figure 4.2 Spherical polar coordinates used to define the orientation of a cylindrically symmetric molecule in a Cartesian coordinate system.

In our simulations, we used the method, devised by Barker and Watts [16] to change the molecular orientation. In this method, one of the Cartesian laboratory axes is chosen at random and the molecule is then rotated, via a rotation matrix $\mathbf{R}_\alpha$, by some random amount $\delta\Psi$ about the chosen axis, where

$$\delta\Psi = \Delta\,(2 * Rand - 1.0), \tag{4.8}$$

here *Rand* is a random number between 0 and 1 and Δ is the maximum displacement allowed for a given temperature and pressure. If a particle has an orientation given by the unit vector $\hat{u}_{old}$, the new coordinates of the molecule $\hat{u}_{new}$, are given by

$$\begin{pmatrix} \hat{u}_x \\ \hat{u}_y \\ \hat{u}_z \end{pmatrix}_{new} = \mathbf{R}_\alpha \begin{pmatrix} \hat{u}_x \\ \hat{u}_y \\ \hat{u}_z \end{pmatrix}_{old}, \tag{4.9}$$

where $\mathbf{R}_\alpha$ is the rotation matrix, defining the rotation about the axis α *(x, y, z)*. For example, for a rotation about the *z*-axis $\mathbf{R}_z$ is written as

$$\mathbf{R}_z = \begin{pmatrix} \cos\delta\Psi & -\sin\delta\Psi & 0 \\ \sin\delta\Psi & \cos\delta\Psi & 0 \\ 0 & 0 & 1 \end{pmatrix}, \tag{4.10}$$

with similar expressions for rotation about the *x* and *y* axes. In our simulations, the translational and rotational moves were performed together.

4.2.3 Equilibration

The Monte Carlo simulation should run for many configurations while the system equilibrates to the appropriate energy, density, volume, etc. This part of the simulation is

called the equilibration run, and if the properties of the system such as the order parameters, energy, distribution functions etc. are calculated during this period, then we would notice large differences in the initial values until the system reaches equilibrium. Once we know the system has equilibrated, i.e. when the cumulative average configurational value of a property fluctuates about a constant value, then we can start the production run and calculate the system properties at thermal equilibrium.

4.3 Periodic boundary conditions

Due to time constraints and restraints on computer resources, we are limited to the size of the system which can be investigated in a simulation, typically a few hundred to a few thousand particles, depending on the pair potential. However, the finite size of the system induces some surface effects, that is the surface / volume ratio is large, which is unrealistic for a bulk system. To minimise such surface effects, periodic boundary conditions are introduced in the simulation where the sample box is surrounded by exact replicas of itself. That is every particle at a position (x, y, z) in a cubic box of side length λ will have images at $(x\pm n\lambda, y\pm n\lambda, z\pm n\lambda)$ where n is an integer, and in turn, every image is surrounded by identical images. The particles are allowed to move between the simulation box and the images and the boundary conditions ensure that when a particle leaves a box, its image enters the same box in the opposite direction at the same time, so in fact there is the same number of particles in every box for any given configuration, see figure 4.1. However, there is a problem associated with this method in that we now have an infinitely repeating structure where a given particle will interact with all other particles

in the same box and all particles in other boxes, including its own image. This is overcome by the 'minimum image' convention where the interactions of a particle with the others in the system are calculated by locating the nearest image of each particle in the surrounding periodic images of the system. For example, in figure 4.1, particle P can interact either with particle N or its image N'. Using the concept of minimum image, the particle P will interact with N' rather than N.

To help minimise the computational time, a cut-off radius r_c is included beyond which all the intermolecular interactions are neglected or treated as resulting from a continuous range of particles. This is shown in figure 4.1

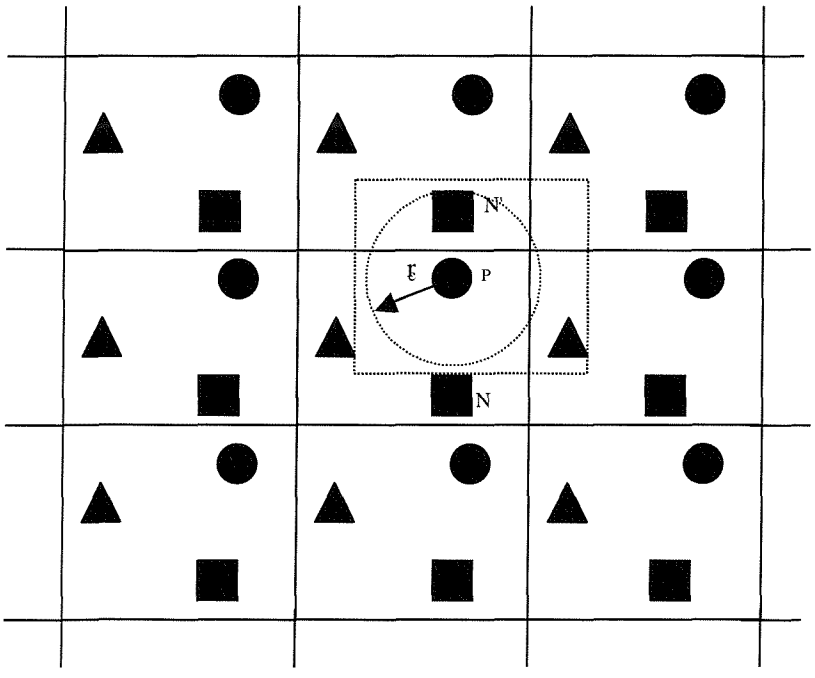

Figure 4.1 Periodic boundary conditions used in computer experiments to simulate a bulk system and also show the minimum image convention and cut-off radius.

4.4 Calculation of system properties

During the production stage of the simulation, thermodynamic and structural properties are calculated for each configuration and averaged. Thermodynamic properties such as the internal energy, density and the enthalpy give information about the physical state and phase behaviour of a system while the structural properties such as the orientational and positional distribution functions, order parameters etc. provide information about the molecular organisation of the system. In the following sub-section, we introduce and define the thermodynamic properties calculated in our simulations. To characterise the phases that are formed, we need to evaluate various distribution and correlation functions; these are introduced in sub-section 4.4.2.

4.4.1 Thermodynamic properties

a) Internal energy

The internal energy is the easiest to calculate since it is already part of the Monte Carlo procedure. The internal energy of the system is half of the sum of all the pair interactions for all the molecules in the system. The factor of half is to avoid calculating each interaction twice. As we have seen the pair interactions are calculated via a potential which depends on the orientation of each molecule and the intermolecular vector and their separation. In general

$$U_{ij} = U(\hat{\mathbf{u}}_i, \hat{\mathbf{u}}_j, r), \tag{4.11}$$

where, $\hat{\mathbf{u}}_i$ and $\hat{\mathbf{u}}_j$ contain the angles which define the orientations of molecules i and j respectively and r is the length of the intermolecular vector, i.e. ($r_i - r_j$).

For a system of N particles, the expression for the total energy is

$$U = \sum_i \sum_{j>i} U_{ij} \,. \tag{4.12}$$

The energy per particle is thus $<U> / N$, where the angular brackets denote an average over all accepted configurations.

b) Enthalpy

An interpretation of the enthalpy is that a change in enthalpy is equal to the heat supplied at constant pressure to a system. Once the internal energy and density are known then the enthalpy is calculated from

$$<H> = <U> + P<V>, \tag{4.13}$$

for an NPT ensemble. The volume is calculated directly from the simulation.

The entropy and the Gibbs free energy cannot be measured directly from the simulation, because the partition function Q (see equation 1.*) is not available. However the change in entropy at the transition can be calculated from equation 1.17.

4.4.2 Structural properties

In addition to the thermodynamic properties, we have also calculated two long-range order parameters to distinguish between the phases formed and to locate the transitions between them. While the orientational order parameter is useful to detect if

there is a liquid crystalline phase or not (it is zero in the isotropic phase, non-zero in the liquid crystalline phase and unity for a perfectly ordered crystal) the translational order parameter, τ, is used to distinguish smectic phases from isotropic or nematic.

a) Orientational order parameter $\langle P_2 \rangle$

In Monte Carlo simulations, we normally use the **Q** tensor, introduced by Vieillard-Baron [17], to calculate the second rank orientational order parameter $\langle P_2 \rangle$, without the need to know the director, $\hat{n}$.

The **Q** tensor is defined as

$$\mathbf{Q} = \frac{1}{N}\sum_{i=1}^{N}\begin{pmatrix} u_{i,x}^2 - 1/3 & u_{i,x}u_{i,y} & u_{i,x}u_{i,z} \\ u_{i,x}u_{i,y} & u_{i,y}^2 - 1/3 & u_{i,x}u_{i,z} \\ u_{i,x}u_{i,z} & u_{i,x}u_{i,y} & u_{i,z}^2 - 1/3 \end{pmatrix}, \tag{4.14}$$

for each configuration. By diagonalising this matrix, we can define the orientation of the director frame in our laboratory frame. The director itself is defined by the eigenvector corresponding to the largest eigenvalue, λ_{max}, of Q. The average of the largest eigenvalue, which is calculated by diagonalising the Q tensor after every cycle, is taken to be $\langle P_2 \rangle$.

b) Translational distribution function $\rho(z)$

For smectic phases, the defining characteristic is their layer structure with its one-dimensional translational order parallel to the layer normal. At the single molecule level

this order is completely defined by the singlet translational distribution function, $\rho(z)$, which gives the probability of finding a molecule with its centre of mass at a distance z from the centre of one of the layers, irrespective of its orientation. This probability can be expanded in a Fourier series

$$\rho(z) = (1/d) + (2/d)\sum_{n\neq 0} \tau_n T_n(\cos 2\pi z/d) \quad . \tag{4.15}$$

where ($cos\ 2\pi z/d$) are the Chebychev polynomials.

Associated with this distribution function is the set of translational order parameters [23]

$$\tau_n = \int \cos(2\pi z n/d)\rho(z)dz \quad , \tag{4.16}$$

where d is the layer spacing [23], and is also known as the smectic periodicity. τ_n gives a measure of the translational order in the system. It has limiting values of 1, meaning perfect order (smectics) and 0 meaning no layer (nematic and isotropic). The dominant translational order parameter at least near the SmA-N or SmA-I transition is given by

$$\tau_1 = < \cos 2\pi z/d > . \tag{4.17}$$

From the translational distribution function, $\rho(z)$, we can calculate d, by measuring the distance between any two peaks. Once d is known, then it is relatively forward to calculate the τ_n.

d) Radial distribution function *g(r)*

This function is defined so that $g(r)\ r^2dr$ is the probability that a molecule will be found in the range dr at a distance r from another. It is also normalised so that, in the absence of the correlations at large separations, $g(r)$ tends to unity. This is because at large distances, (in a liquid) the correlation between the molecules is completely lost and the probability of finding a second molecule is independent of r. To calculate $g(r)$ it is necessary to look at a small, finite range of r, such that $r+\delta r/2 < r < r-\delta r/2$ in order to find a significant number of particles with a separation in that range. This is normally calculated by constructing a histogram where first a range is defined and then divided into small and equally spaced regions. The function is then evaluated over all regions, incrementing the appropriate section of the histogram. For crystals, this contains sharp regularly spaced peaks, indicating an ordered array of molecules. In liquids, there is only short-range order i.e. there is a local structure of molecules around any given particle and this is indicated by a large peak followed by another much smaller peak. There are two other distribution functions analogous to $g(r)$, namely $g_{\|}(r_{\|})$ and $g_{\perp}(r_{\perp})$, which give the probability of finding a particle at a distance $r_{\|}$ from another at the origin parallel and perpendicular to the director, respectively. These distribution functions are particularly valuable in exploring the layered structures of the smectic phases. $g_{\|}(r_{\|})$ provides information about the distribution of particles between layers while $g_{\perp}(r)$ provides information about the structure of the smectic phase within a layer. This is calculated for all the layers and then averaged.

Chapter 5

Results and discussion

5.1 Introduction

In this Chapter we present and discuss the results of our simulations using the S-function Corner potentials. It is divided into three main sections, each corresponding to one of the systems we have investigated. The results for the uniform spherocylinder are discussed in section 5.2. Those for the spherocylinder with the sphere in the central sphere of radius 1.5 are considered in section 5.3 and in section 5.4 we discuss the results for the spherocylinder with a central sphere of radius 1.75. For convenience, we shall refer to these as system 1, system 2 and system 3, respectively. For each system, we give the thermodynamic properties calculated during the production run, together with the structural properties and snapshots of configurations to help characterise the phases formed.

5.2 Simulation Details

The simulations were performed using an isothermal-isobaric Monte Carlo simulation technique, with 2000 particles in an orthorhombic box. The phase behaviour for the uniform spherocylinder, was investigated at three pressures, P^*, of 1.0, 2.0 and 3.0, while for the other two systems, due to time constraints, the simulations were only performed for two scaled pressures: 1.0 and 2.0. The simulations took about 0.7s for one cycle on a SGI Power Challenge R10000. In some cases, very long runs were needed to equilibrate the systems, typically 1,000000 cycles near the phase transitions. Despite the very long equilibration run, this was not sufficient to avoid a residual hysteresis present at some temperatures, typically in the vicinity of the phase transitions.

5.3 System 1

A phase transition is usually identified by a jump in the slope of the graph of a thermodynamic property, as explained in Chapter 1. For a scaled pressure of 1.0, from the thermodynamic plots (see figure 5.1.1) we can identify two first order transitions at scaled temperatures of 1.25 ± 0.05 and 1.05 ± 0.05. We notice that the results for the cooling run and the for the heating run are the same. The transition temperatures were obtained by taking the average between the two temperatures on either side of the transition, while the uncertainties are estimated as just half the difference between the same two temperatures on either side of the transition. The enthalpy of transition was estimated by taking the difference between the values obtained from a linear extrapolation of the values of the

enthalpy at higher and lower temperatures. The change in enthalpy, ΔH^*_{SmAI}, at the transition temperature of 1.25, is approximately 2.51 ± 0.01, corresponding to a transitional entropy, $\Delta S/R$, of 2.01 ± 0.09. This value is consistent with a smectic A-isotropic transition [18]. Another indication that a smectic A phase is formed is given by the value of the orientational order parameter, $\langle P_2 \rangle$, which has a jump to about 0.85 at the scaled temperature of 1.25. This relatively high value of $\langle P_2 \rangle$ indicates a more ordered phase than a nematic, which has typical values of $\langle P_2 \rangle$ in the range 0.3 to 0.6. In figure 5.1.1, we also report the scaled number density, ρ^*. The relative change in volume, which is defined as $2(V_I^* - V_{SmA}^*)/(V_I^* + V_{SmA}^*)$, is estimated to be about 15%, which is in good agreement with the results obtained for a smectic A-isotropic transition from the simulation of Gay-Berne mesogen GB(4.4, 20, 1, 1), at a scaled pressure of 1.0 which is 14.8%; however this value is rather large for a real SmA-I transition. The second transition, which involves a phase which will be identified as crystal B, occurs at a temperature of 1.05 ± 0.05, although it is quite difficult to see on the plots, indicating a somewhat weak transition. There is an increase in the value of $\langle P_2 \rangle$, which suggests a more ordered phase than the smectic A phase. For this transition, the change in enthalpy, ΔH^*_{BSmA}, is 0.59 ± 0.01, which gives a transitional entropy, $\Delta S/R$, of 0.56 ± 0.04.

The thermodynamic quantities calculated at a scaled pressure of 2.0 are shown in figure 5.1.2. where now the SmA-I transition and B-SmA transitions, occur at scaled temperatures of 1.65 ± 0.05 and 1.3 ± 0.10, respectively. The increase in pressure, has increased the transition temperature, by 0.4 and 0.25, in the scaled temperature, for the SmA-I and B-SmA transitions, respectively. The scaled enthalpy and the scaled energy

per particle are shown in figures 5.1.2(a) and 5.1.2(b), respectively. Clearly there is hysterisis present for this transition.

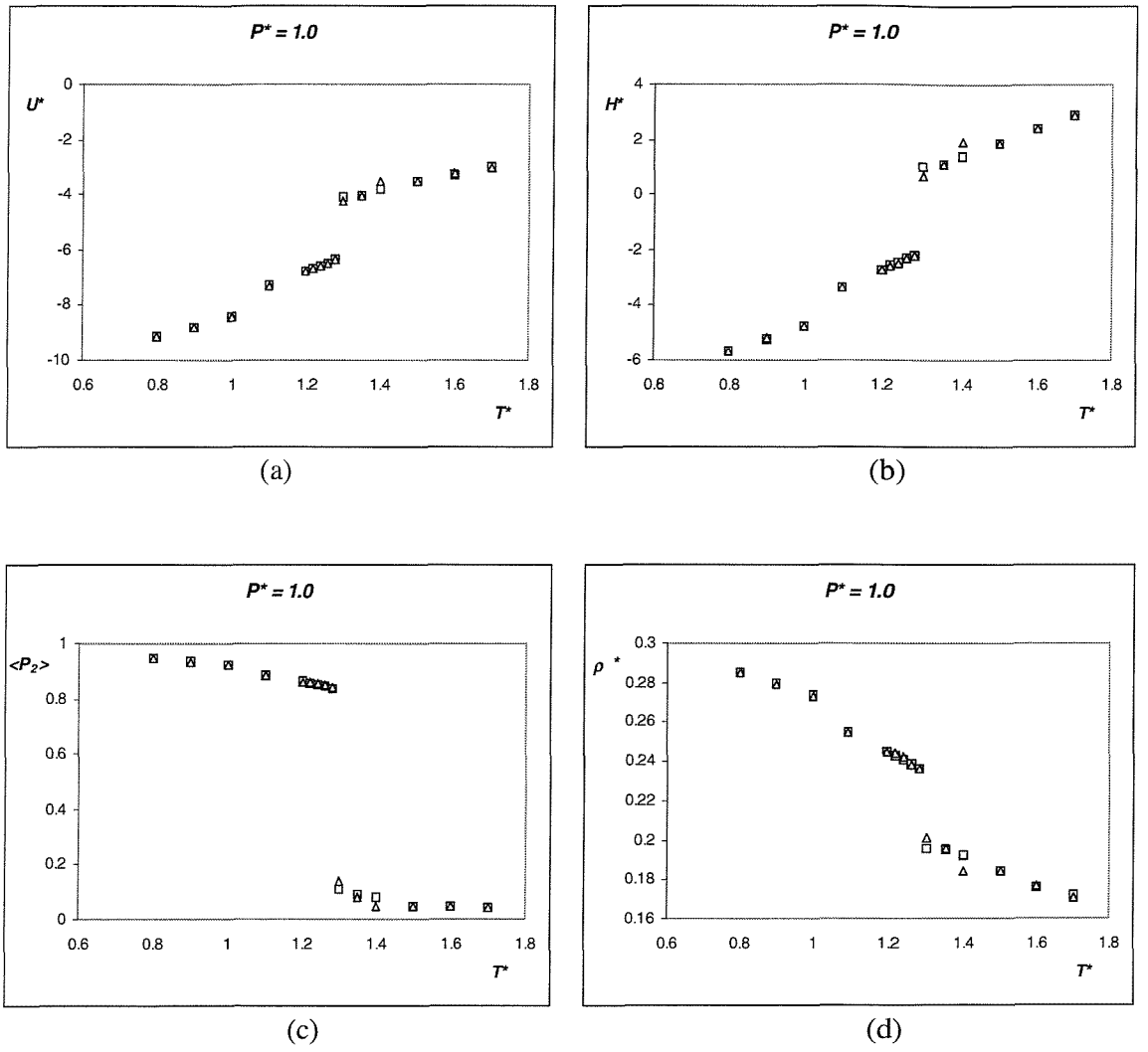

Figure 5.1.1 Thermodynamic properties for the sample at a scaled pressure, P^*, of 1.0 as a function of the scaled temperature, T^*. Squares represent the cooling run while the triangles represent the heating run. (a) Scaled internal energy per particle U^*, (b) scaled enthalpy per particle H^*, (c) orientational order parameter $\langle P_2 \rangle$ and (d) scaled number density ρ^*.

The enthalpy of transition, $\Delta H^*_{SmA\text{-}I}$, is estimated to be 2.55 ± 0.01 for the *SmA-I* transition, with a corresponding entropy change, $\Delta S/R$, of 1.55 ± 0.05.

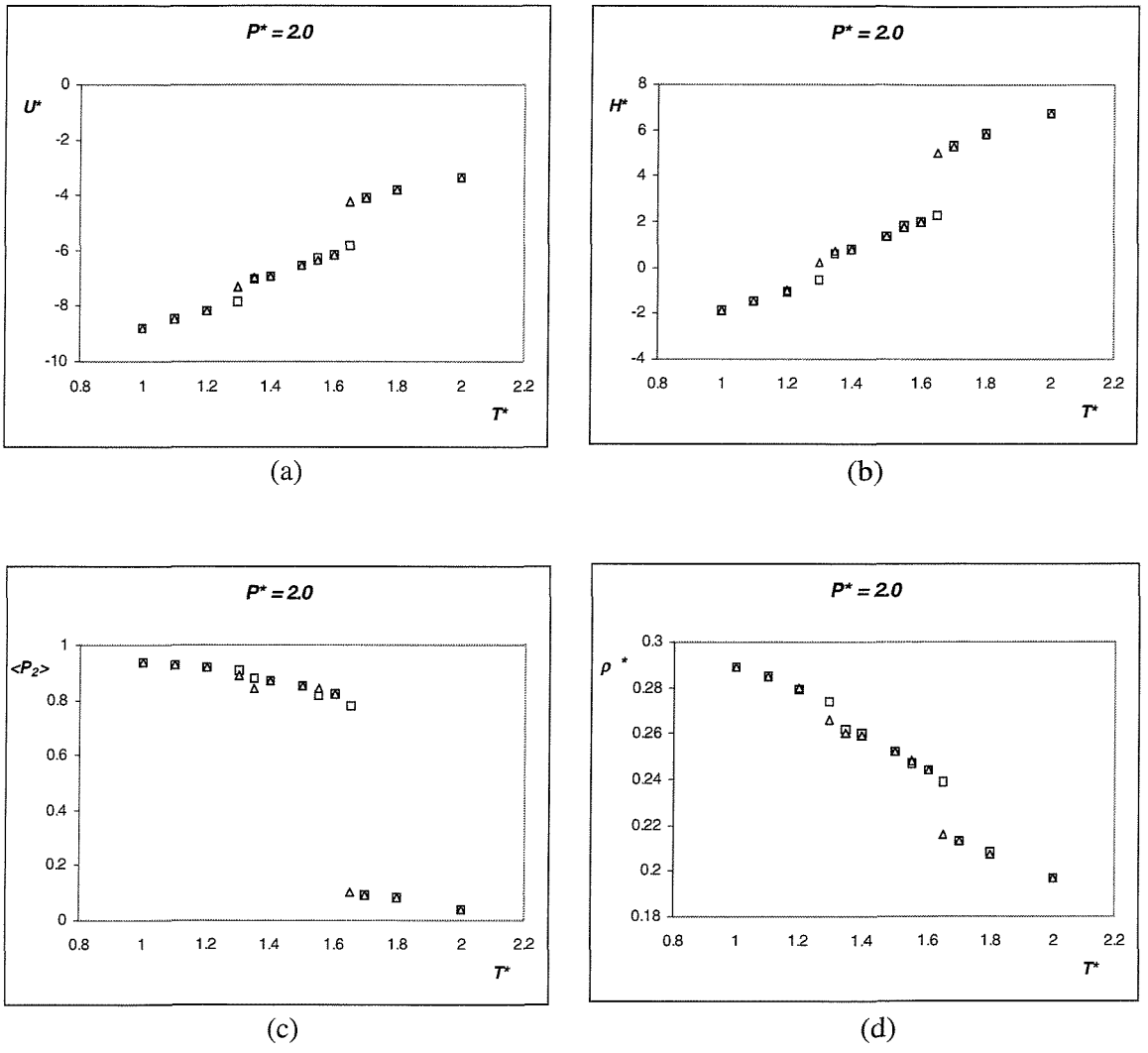

Figure 5.1.2 Thermodynamic properties for the sample at a scaled pressure, P^*, of 2.0 as a function of the scaled temperature, T^*. Squares represent the cooling run while the triangles represent the heating run. (a) Scaled internal energy per particle U^*, (b) scaled enthalpy per particle H^*, (c) orientational order parameter $\langle P_2 \rangle$ and (d) scaled number density ρ^*.

The values for the orientational order parameter are shown in figure 5.1.2(c), where we can see that in the isotropic phase, the value of $\langle P_2 \rangle$ is below 0.1 up to T^* of 1.65, then it jumps to a higher value of 0.80 in the smectic A phase. On cooling the system further, a second transition occurs at a scaled temperature of 1.30, which corresponds, to the B-SmA transition. For this transition, the change in the enthalpy, ΔH^*_{SmA1}, is estimated to be 0.74 ± 0.01 which corresponds to an entropy change $\Delta S/R$ of 0.57 ± 0.05. The change in scaled number density, ρ^*, is estimated to be about 14%. A comparison with Zewdie's results is made in sub-section 5.3.2.

Finally, for the highest pressure, P^* of 3.0, the thermodynamic quantities are presented in figure 5.1.3. Again, two transitions can clearly be identified from discontinuities in the plots and with some hysterisis. The SmA-I transition now occurs at a scaled temperature of 1.90 ± 0.01 and the B-SmA occurs at a scaled temperature of 1.50 ± 0.01. In figure 5.1.3(b), we report the scaled enthalpy for the cooling and heating runs. The change in enthalpy, $\Delta H^*_{SmA\text{-}I}$, for the SmA-I transition is 2.70 ± 0.01. From this we can calculate the entropy of transition, $\Delta S/R$, which is found to be 1.42 ± 0.07. An analogous calculation gives a value of 0.81 ± 0.01 for the enthalpy of transition at the scaled temperature of 1.5, which corresponds to the B-SmA transition. The entropy change for this transition is estimated to be 0.54 ± 0.04. Although we see large variations in the entropy change for the SmA-I transition when comparing for pressures 1.0, 2.0 and 3.0, there is not a big difference in the entropy change for B-SmA transition for the three pressures. The values of the orientational order parameter, $\langle P_2 \rangle$, are plotted in figure 5.1.3(c). In the isotropic phase, the order parameter is as small as 0.05. It then jumps to a value of 0.80 at the

transition to the SmA phase. It increases slightly to a value of 0.88 at T^* of 1.5 where a second very small jump occurs to a value of 0.91 for the crystal **B** phase. Finally, the change in density for the SmA-I transition, $2(V_I^* - V_{SmA}^*)/(V_I^* + V_{SmA}^*)$, is estimated to be 8.8% and for the B-SmA transition it is 2.5%. The temperature dependence of the number density is shown in figure 5.1.3(d).

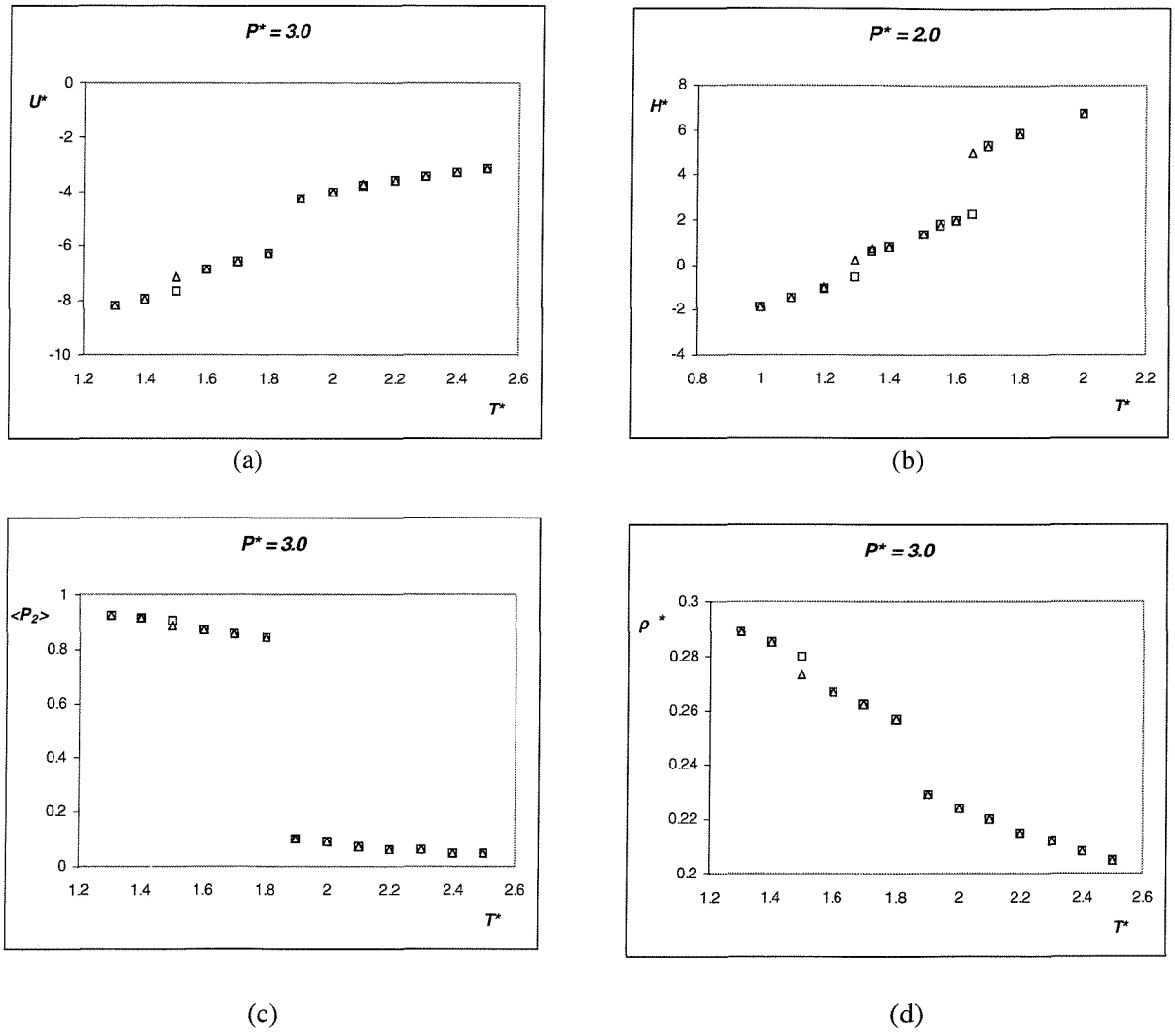

Figure 5.1.3 Thermodynamic properties for the sample at a scaled pressure, P^*, of 3.0 as a function of the scaled temperature, T^*. Squares represent the cooling run while the triangles represent the heating run. (a) Scaled internal energy per particle U^*, (b) scaled enthalpy per particle H^*, (c) orientational order parameter $\langle P_2 \rangle$ and (d) scaled number density ρ^*.

Once the change in volume, ΔV^* and the change in enthalpy, ΔH^*, at the transition are known, then we can calculate the slope of the associated phase boundary by means of the Clapeyron equation,

$$\frac{dP^*}{dT^*} = \frac{\Delta H^*}{T^* \Delta V^*} . \tag{5.1}$$

The phase diagram constructed from the transitions for the three scaled pressures, is shown in figure 5.1.4.

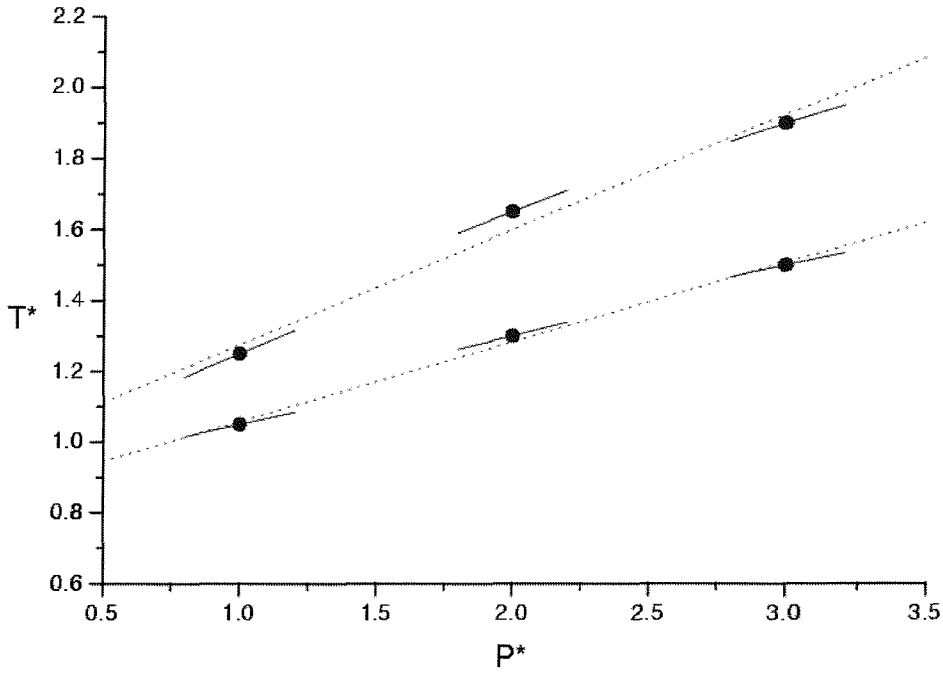

Figure 5.1.4 Phase diagram for the system 1 composed of spherocylinders investigated. The points represent the transition temperatures estimated as discussed in text; the solid short lines represent the slope of the phase boundaries estimated from the Clapeyron equation, while the dotted lines represent the phase boundaries obtained from a linear fit of the three points available for each phase transition.

The solid lines represent the slopes calculated from the Clapeyron equation while the dotted lines are the boundaries estimated with a linear fit of the points, for each phase transition. As can be seen from figure 5.1.4, there is a good agreement between the slopes at the phase boundary calculated by the Clapeyron equation and the slopes obtained from the fit of the transition temperatures in the graph. The slopes of the phase boundaries, assuming a linear dependence of transition temperatures against pressure, for the SmA-I transition is 3.1, and for the B-SmA transition is 4.4. We observe, from figure 5.1.4, that as the pressure is increased, so does the stability of the more ordered phases, in this case SmA and B. Also, the greater slope of the graph for the SmA-I in comparison with the B-SmA transition means that the range over which the SmA phase is stable increases, as the pressure is increased. A similar behaviour, although with different stable phases, is observed for the mesogen GB(4.4, 20, 1, 1) where increasing the pressure brings a nematic phase into phase diagram, see figure 5.1.5.

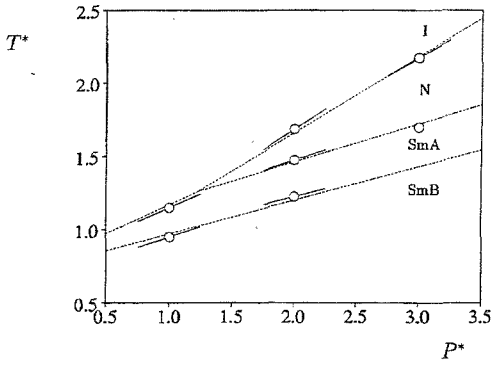

For our system we do not observe a nematic phase presumably because the length-to-breadth ratio of the spherocylinders are too short [4]. This is suggested by studies of

systems of hard spherocylinders by Bolhuis et al. [4], which found that for short spherocylinders (length-to-breadth ratio smaller than 3) only isotropic and solid phases are stable. The smectic phase appears for an aspect length-to-breadth ratio larger than ~ 4.1 while the nematic phase is stable only for spherocylinders with aspect ratio larger than ~ 4.7. In Ref. [4] the authors use *L/D* to indicate the shape anisotropy and not the aspect ratio. Our system has a shape anisotropy of 2 plus two hemispheres of diameter 0.5 at both ends giving an aspect ratio of 3.0. This aspect ratio should not form any mesophases in the absence of attractive interactions. However, the presence of a relatively strong side-by-side interaction, added to the repulsive contribution, stabilises the smectic phase.

5.1.2 Structural properties

The structural properties which were obtained from the simulation, were introduced in Chapter 4. In this section, we shall show how we can identify the phases with the aid of the structural properties. This study has been done for the system at a scaled pressure of 2.0 only, due to time constraints.

We begin with the orientational order. The orientational distribution function, $f(cos\beta)$, is shown in figure 5.1.6(a) and 5.1.6(b) for the smectic A phase and crystal B phase, respectively. Clearly, the distribution functions are strongly peaked for values of $cos\beta$ close to one and virtually no particles have an orientation perpendicular to the director. This behaviour is in contrast with the observation for hard spherocylinders [24] that some particles can lie in between the layers of a smectic phase. In our case, however, the

presence of the attractive potential with its strong minimum for a side-by-side interaction clearly favours the particles to be aligned parallel and so to stay in the layer. The solid lines shown in figure 5.1.6, represent a fit to the function:

$$f(\cos\beta) = Z^{-1}\exp(aP_2(\cos\beta)), \tag{5.2}$$

where Z is given by

$$Z = \int \exp(aP_2(\cos\beta))\sin\beta d\beta . \tag{5.3}$$

This kind of orientational distribution function is based on the Maier-Saupe [25] theory, where, for a single molecule, the molecular field potential or potential of mean torque,

$$U_{mf} = -aP_2(\cos\beta), \tag{5.4}$$

is predicted. In equation (5.4), $a^* = \varepsilon\overline{P_2}/k_BT$ is the strength parameter, proportional to the orientational order parameter. Although the Maier-Saupe theory has been derived for nematic phases, it is to be expected that the orientational distribution function has the same form in smectic phases as well. The strength parameters for the various temperatures are reported in Table 1. It is clear from the values that the orientational distribution function $f(\cos\beta)$ can be almost perfectly represented assuming a Maier-Saupe potential. We notice that the ratio between the strength parameter a at different temperatures is not the same as the ratio between the orientational order parameter at the same temperatures, as predicted by the Maier-Saupe theory. For highly ordered systems higher order Legendre polynomials enter the expansion of the molecular field energy in equation (5.4), which should be written as

$$U_{mf} = -\sum_L a_L P_L(\cos\beta) \tag{5.5}$$

However, in the high order limit, the distribution function $f(\cos\beta)$ adopts significant values only for β close to zero, so that each polynomial reduces to a simple quadratic form in β. Therefore the complete expansion in equation (5.5) becomes equivalent to the truncated expansion in equation (5.4), where the coefficient a now contains contributions from all of the higher order Legendre polynomial.

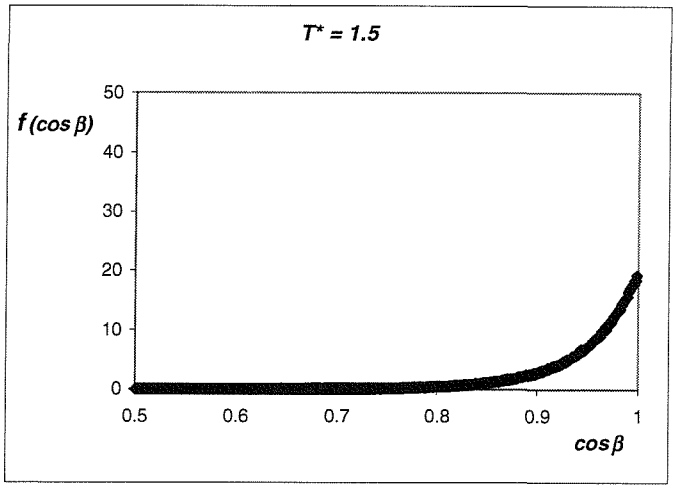

(a)

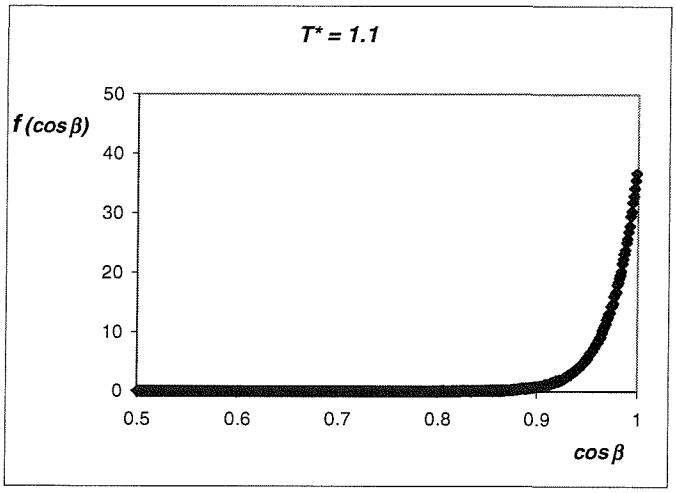

(b)

Figure 5.1.6 Orientational distribution function, $f(\cos\beta)$, with the best fit curve for the system at a scaled pressure of 2.0. (a) smectic A phase at a scaled temperature, T^*, of 1.5; (b) crystal B phase at a scaled temperature of 1.1.

T^*	1.00	1.10	1.20	1.30	1.40	1.50	1.60	1.65
a^*	15.73	13.81	12.16	10.48	7.84	6.67	5.94	5.23
P_2	0.936	0.928	0.919	0.907	0.868	0.850	0.820	0.780
a^*/P_2	16.8	16.36	15.87	15.02	12.65	11.78	11.60	11.06

Table 1: The field strength parameter a^* of the Maier-Saupe theory (Eq.5.4) obtained from the fitting of the orientational distribution function $f(cos\beta)$.

The singlet translational distribution function, $\rho(z)$, is shown in figure 5.1.7(a) for the smectic A phase, at a scaled temperature of 1.5, and in figure 5.1.7(b) for the crystal B phase, at a scaled temperature of 1.1. In both cases, the distribution is strongly peaked. In contrast to the smectic A phase, the presence of long range translational order in the crystal B phase, results in more intense and hence sharper peaks in the plots. The width of the peaks gives an indication of the layer spacing and this is calculated from the plots to be about 3, which is the length of the particles. The intensity of the peaks is not constant and is reduced towards the edges of the box. This is due to the fact that the layers, in general, do not arrange themselves parallel to one face of the box. As a consequence the box contains some complete layers and some others only in part, as can be seen from the snapshots of configurations shown in figures 5.1.8(b) and 5.1.8(c) which correspond to the smectic A and crystal B phases, respectively. We can see from these figures there are four layers which cross the box from the left side to the right side, while the others are cut partially at the top and bottom of the box. Correspondingly, there are four main peaks in the distribution $\rho(z)$ plus the minor lateral peaks. The programme used to generate the

snapshots, represents the particles as ellipsoids, rather than spherocylinders. Also, in order to fit the pictures on the page, some resizing was done, and as a result, the molecules seem to be tilted with respect to the layer normal.

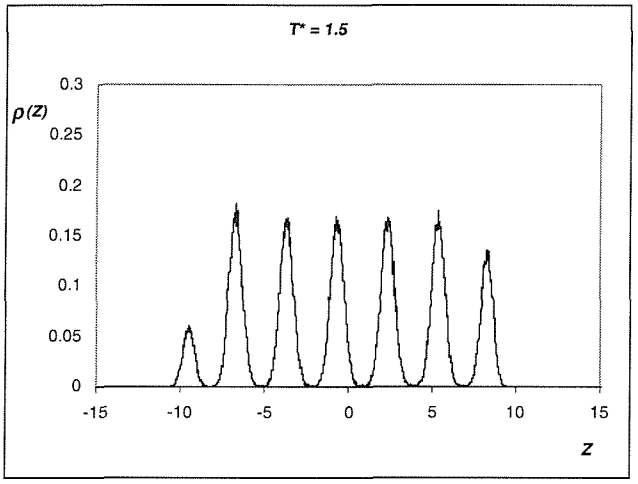

(a)

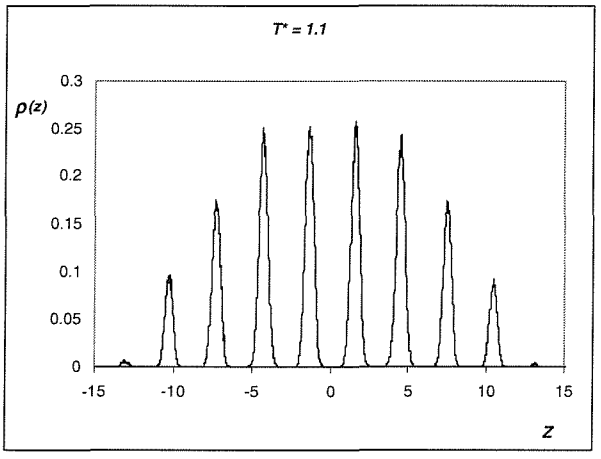

(b)

Figure 5.1.7 Translational distribution function, $\rho(z)$, at a scaled pressure of 2.0 for (a) the smectic A phase, at a scaled temperature of 1.5; (b) the crystal B phase at a scaled temperature of 1.1.

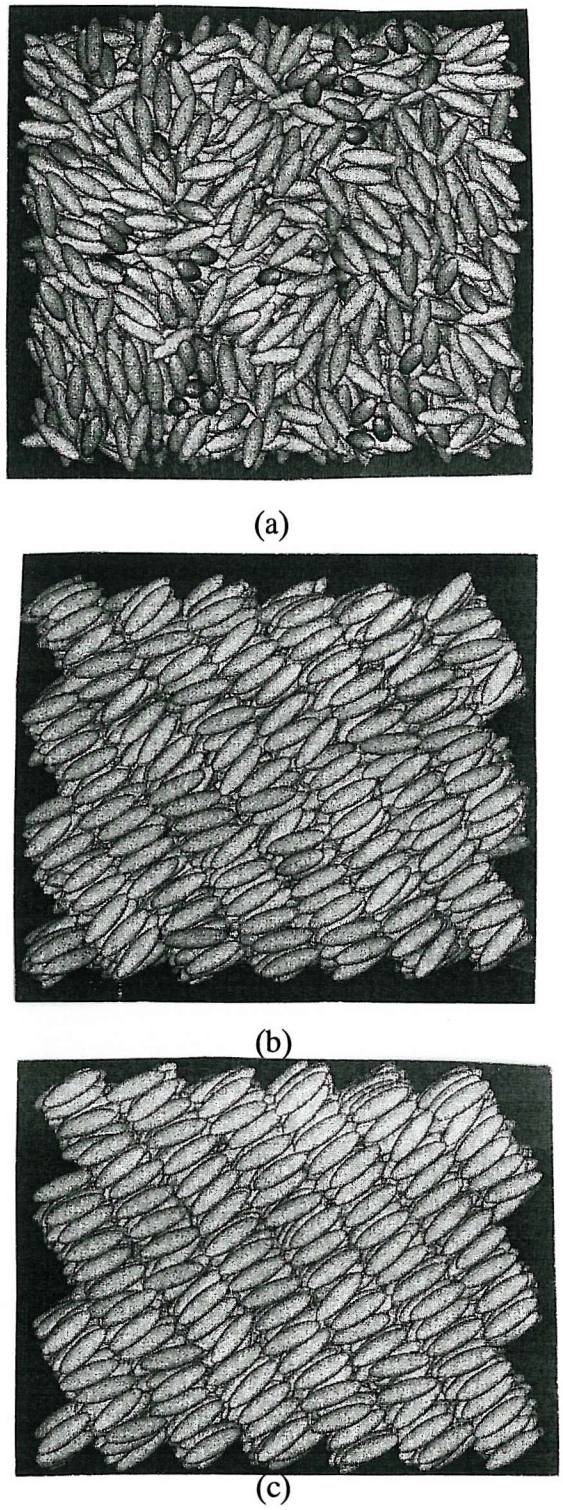

Figure 5.1.8 Snapshots of the configurations for the system at a scaled pressure of 2.0 for the (a) isotropic phase at a scaled temperature of 1.8; (b) for the smectic A phase at a scaled temperature of 1.5; (c) for the crystal B phase at a scaled temperature of 1.1.

The radial distribution functions, $g(r)$, for the three phases, isotropic at T^* of 1.8, smectic A at T^* of 1.5 and crystal B at T^* of 1.1, are shown in figures 5.1.8(a), 5.1.8(b) and 5.1.8(c), respectively. In the isotropic phase, the radial distribution function shows only a relatively small peak at a separation of 1.21, then it rapidly converges to a constant limiting value of 1.0, indicating the absence of any translational correlation for longer distances. The radial distribution function at the lower scaled temperature of 1.5 in the SmA phase shows a more structured form, with a sharp peak at 1.15, followed by a smaller peak at a distance of 2.19 and a broad peak at distance of about 3.0. At distances greater than about 6.0, we see only small deviations from the limit of 1.0. Again this is due to the, decreased but still present, translational correlation between particles at large separations. At a scaled temperature of 1.1, the radial distribution function shows an extremely structured form, with a very sharp peak at a distance of 1.15, then a double peak at a distance of about 2, followed by significant structure long range which is continuous, although slightly reduced, even at a distance of 10, which is half the size of the simulation box. The double peak in the radial distribution function is a characteristic of local hexagonal packing of the particles in the plane. As was mentioned in Chapter 1, smectic B and crystal B phases, both show hexagonal arrangements of particles. In the smectic B phase, there is no long-range correlation of particles between layers, only long-range bond orientational order, whereas in a crystal B phase, there are translational correlations between layers. The peak at r* of 3, could be due to end-to-end arrangement of particles or it could be due to side-by-side particles 3 shells apart. The relatively small peak at r* of 4, corresponds to 4 shells of side-by-side particles. The radial distribution function at a scaled temperature of 1.1 suggests a more ordered phase than a smectic B

phase. As a comparison, the radial distribution for the smectic B phase observed in the Gay-Berne mesogen *GB*(4.4, 20, 1, 1) only shows a broad second peak, and is not much different from the radial distribution function for the smectic A phase for the same mesogen [19]. As well as the radial distribution function, $g(r^*)$, we have also calculated the parallel $g_{\parallel}(r_{\parallel}^*)$ and perpendicular $g_{\perp}(r_{\perp}^*)$ radial distribution functions which give the probability of two particles being separated by a distance $r_{\parallel}^*$ measured parallel to the director and a distance $r_{\perp}^*$ measured perpendicular to the director, respectively. As expected, these functions are featureless in the isotropic phase, due to the absence of a layer structure. The parallel distribution functions at the scaled temperatures of 1.5 and 1.1 are shown in figures 5.1.9(a) and 5.1.9(b). The periodic nature of $g_{\parallel}(r_{\parallel}^*)$ in the smectic A phase, shown in figure. 5.1.9(a), indicates the clear tendency for the particles to arrange themselves in layers. The average spacing between the peaks can be used to determine the scaled layer spacing, d^*; this is found to be 3.0 ± 0.1, which is to be expected from the length of the spherocylindrical molecules which is also 3.0. On cooling to the crystal B phase, the peaks become sharper and hence more intense, due to the higher translational ordering of molecules, however the layer spacing is almost unchanged at 3.0. The loss of the intensity of the peaks is due to the fact that the layers are tilted with respect to the simulation box and so there are different number of molecules in each layer; so the layers in the middle have more molecules that the layers near the corner of the box. In figures 5.1.10(a) and 5.1.10(b), we show the in-plane radial distribution function for smectic A at the scaled temperature of 1.5 and for crystal B at the scaled temperature of 1.1, respectively. In the smectic A phase, we can see that there is not much order within the plane. The small number of peaks with decreasing intensity

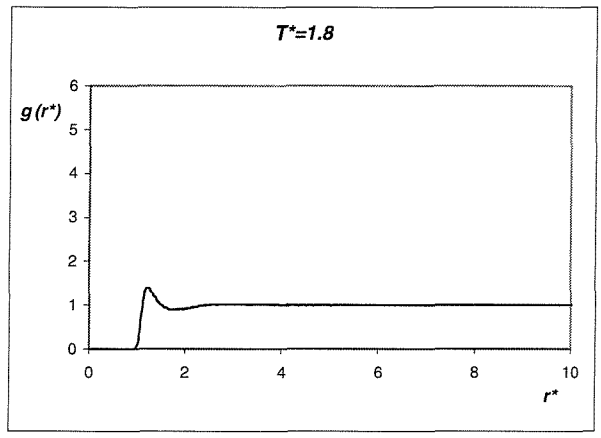

(a)

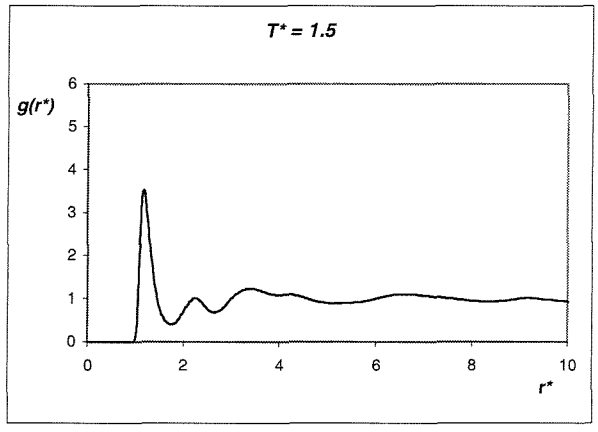

(b)

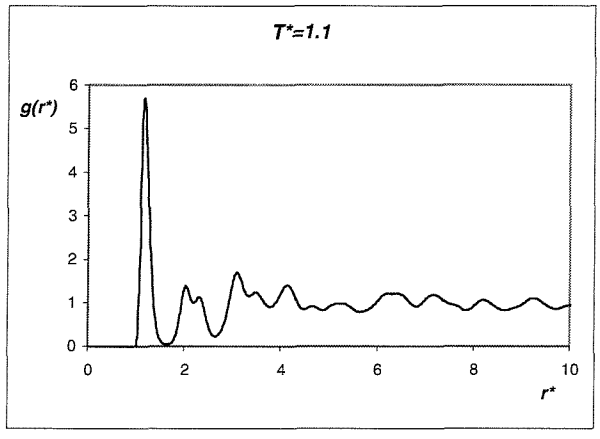

(c)

Figure 5.1.8 Radial distribution function, g(r*), for three phases at a scaled pressure of 2.0. (a) isotropic phase at a scaled temperature of 1.8; (b) smectic A phase at T* of 1.5; (c) crystal B phase at T* of 1.1.

indicates that there is only short-range translational order within the layers. However, for distances greater than about 7.0, the correlation between the molecules is lost and $g_{\perp}$ tends to unity. In the crystal B phase, the in-plane order extends to larger distances and even at distance of about 10, the phase is still very structured. The first peak in the crystal B phase which is significantly sharper and more intense than the smectic A phase, suggests that the nearest neighbour cluster is more ordered at the lower temperature, as expected.

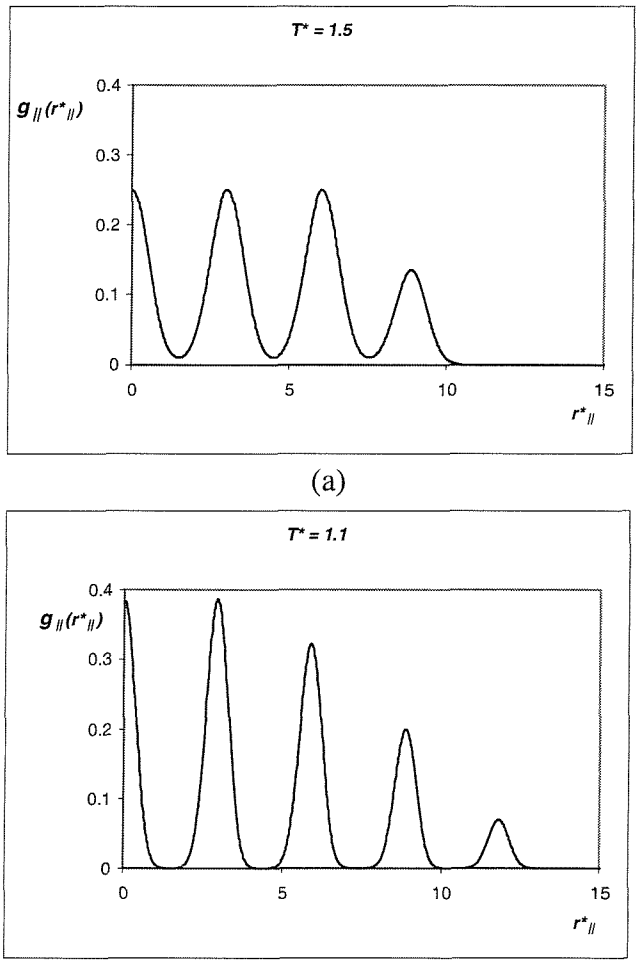

Figure 5.1.9 The parallel distribution function, $g_{\parallel}(r^*_{\parallel})$, at a scaled pressure of 2.0 for (a) the smectic A phase at a scaled temperature of 1.5; (b) the crystal B phase at a scaled temperature of 1.1.

In figure 5.1.10(b), we also note that the structure shows much more order than the corresponding plot for the Gay-Berne mesogen GB(4.4, 20, 1, 1) [19], where a smectic B phase was reported. This prompts us to conclude that the highly ordered structure is most probably a crystal B rather than a smectic B.

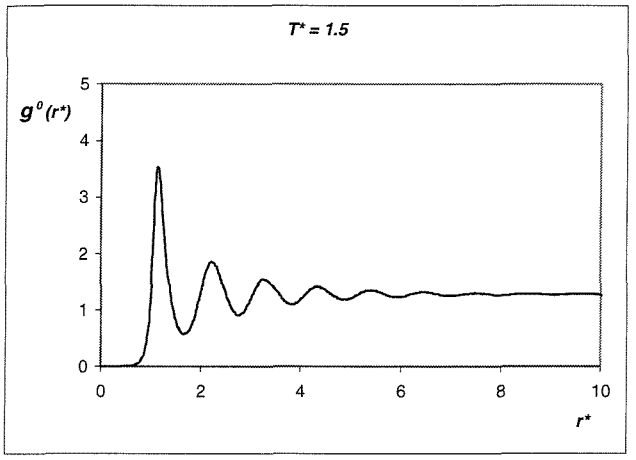

(a)

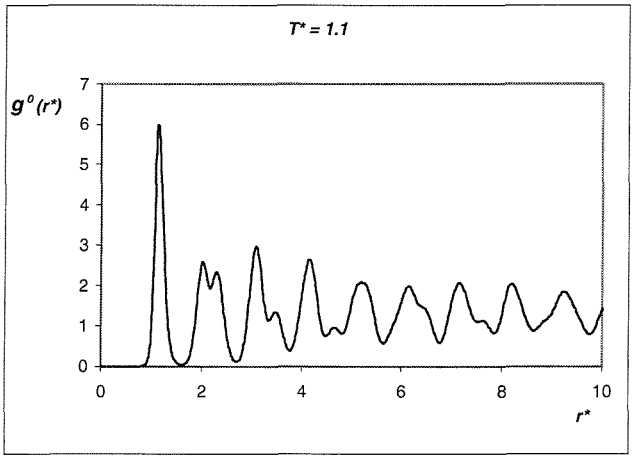

(b)

Figure 5.1.10 The perpendicular distribution function, $g_{\perp}^{0}(r_{\perp})$, representing the translational order within a layer, at a scaled pressure of 2.0 for (a) the smectic A phase at a scaled temperature of 1.5; (b) the crystal B phase at a scaled temperature of 1.1.

In order to characterise more completely the order for the crystal B phase, it is useful to calculate the perpendicular distribution functions for adjacent layers, $g_{\perp}^{n}(r_{\perp}^{*})$, where the index n refers to the layer with which we correlate the particles. Thus, for n equal 0 the distance $r_{\perp}^{*}$ is measured between particles in the same layer, for n equal to 1, the distance is measured for all particles in layers 0 and 1, and for n equal to 2 the distance is measured for all particles in layers 0 and 2, and so on. The plot of $g_{\perp}^{1}(r_{\perp}^{*})$ for the smectic A is shown in figure 5.1.11(a), where we notice that only a few very weak peaks are present, indicating that there is no correlation between the in plane positions of particles contained in adjacent layers. For the crystal B phase, however, we can still see intense peaks, suggesting strong correlations between particles in adjacent layers. We also notice that the first peak in figure 5.1.11(b) appears at a distance of 0.65, which is roughly half the distance between two nearest neighbouring particles in the same layer. The superposition of the distribution functions $g_{\perp}^{0}(r_{\perp}^{*})$ and $g_{\perp}^{1}(r_{\perp}^{*})$ clearly shows that the peaks of the second one perfectly match the minima of the first one. The plots of $g_{\perp}^{2}(2)$ for smectic A and crystal B are shown in figures 5.1.12(a) and 5.1.12(b). Once again, we notice that the flat line in figure 5.1.12(a) which indicates the absence of any correlation of particles between the layers for the smectic A phase. In contrast, for the crystal B phase, we can still observe strong peaks suggesting, yet again, strong correlations between particles in next nearest neighbouring layers. This long-range correlation of particles between layers is a firm conformation of a crystal B structure rather than a smectic B structure.

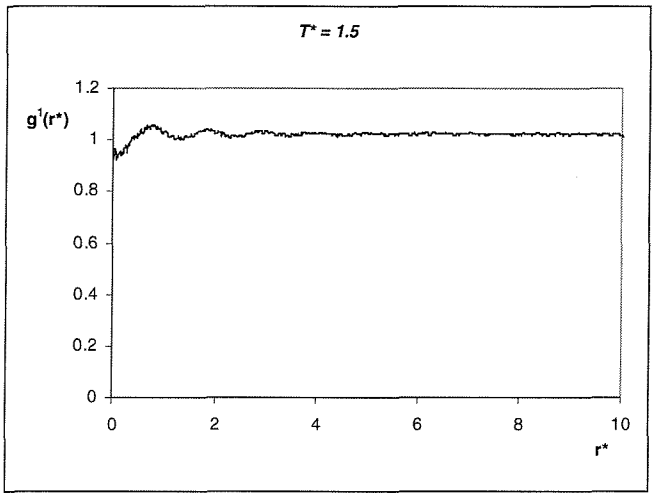

(a)

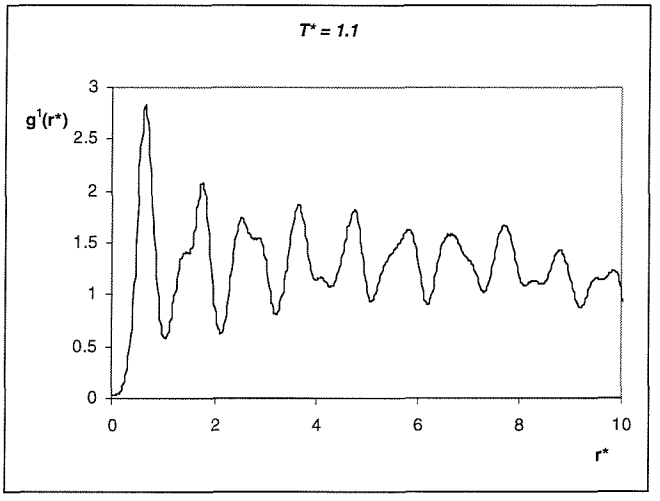

(b)

Figure 5.1.11 The perpendicular distribution function, $g_{\perp}^{1}(r_{\perp}^{*})$, representing the translational correlation of particles within two adjacent layers, at a scaled pressure of 2.0 for (a) the smectic A phase at a scaled temperature of 1.5 and (b) the crystal B phase at a scaled temperature of 1.1.

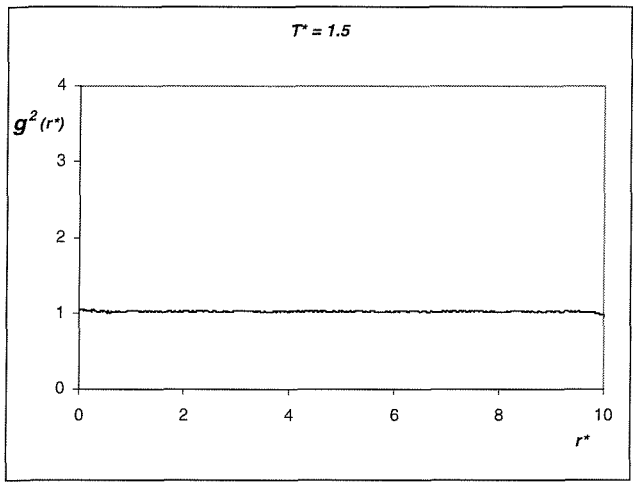

(a)

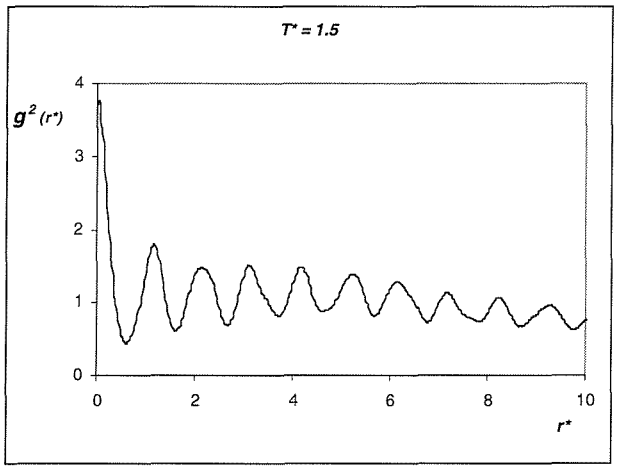

(b)

Figure 5.1.12 The perpendicular distribution function, $g_{\perp}^{2}(r_{\perp}^{*})$, representing the translational correlation of particles within the layers, at a scaled pressure of 2.0 for (a) the smectic A phase at a scaled temperature of 1.5 and (b) the crystal B phase at a scaled temperature of 1.1.

In figure 1.5.14 we show the distance dependent orientational coefficient $G_2(r^*)$ describing the average orientation of two particles with respect to each other. This is defined as

$$G_2(r) =< P_2(\cos\beta_r) >_r \tag{5.6}$$

In the isotropic phase, there is relatively high peak for short distances, meaning that even in the isotropic phase, when two particles are almost in contact, they tend to be parallel to each other. However, very soon the correlation coefficient goes to zero, as expected for an isotropic phase, i.e. orientational correlations are lost. For the smectic A phase, we see that the first peak reaches a maximum value of 0.85 and then decreases slightly to 0.75 and maintains that value for distances as large as 15. For the crystal B phase, the maximum value of the correlation coefficient is now 0.928 due to the increased order of the molecules. Also at long range limit, $G_2(r^*)$ is the square of the order parameter. This gives a value of 0.87 and 0.94 for the order parameter for the *SmA* and *SmB*, respectively. Finally, in figure 5.1.15 we show the radial correlation coefficient which is defined as

$$g_2^+(r) = \left\langle P_2(\cos\beta_{ij}) \right\rangle_r . \tag{5.7}$$

This function probes the distribution of the interparticle vector with respect to the director. For the isotropic phase, there is no director and the coefficient is zero everywhere, showing a spherical distribution of particles surrounding each particle. In the smectic A and crystal B phases, more structure is observed. The negative values obtained for short distances are due to the particles being arranged side-by-side in the layers, that is with the interparticle vector being orthogonal to the director.

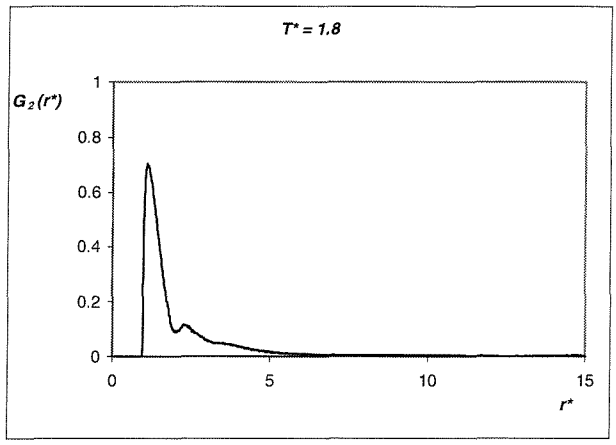

(a)

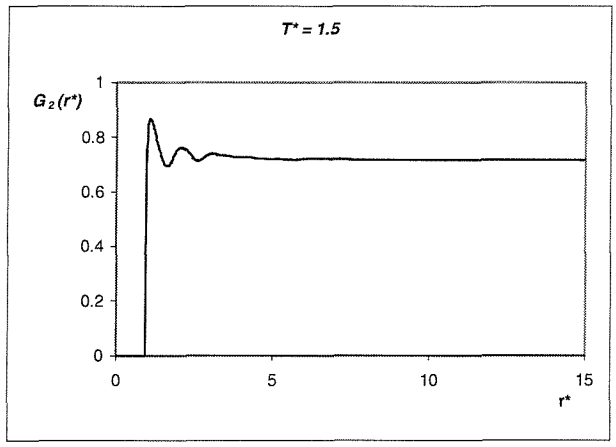

(b)

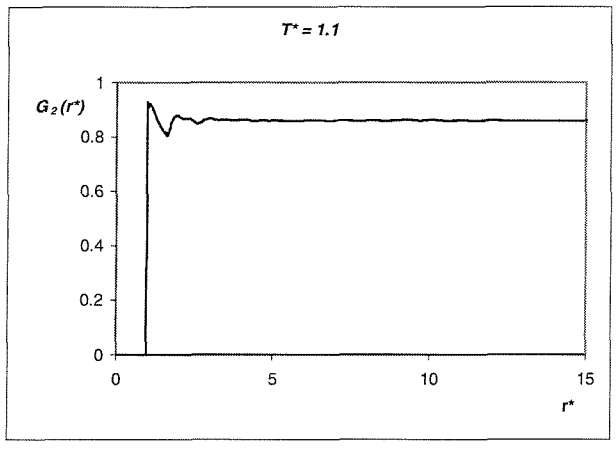

(c)

Figure 5.1.13 Correlation coefficient $G_2(r^*)$ at a scaled pressure of 2.0 for (a) the isotropic phase at a scaled temperature of 1.8; (b) the smectic A phase at a scaled temperature of 1.5 and (c) the crystal B phase at a scaled temperature of 1.1.

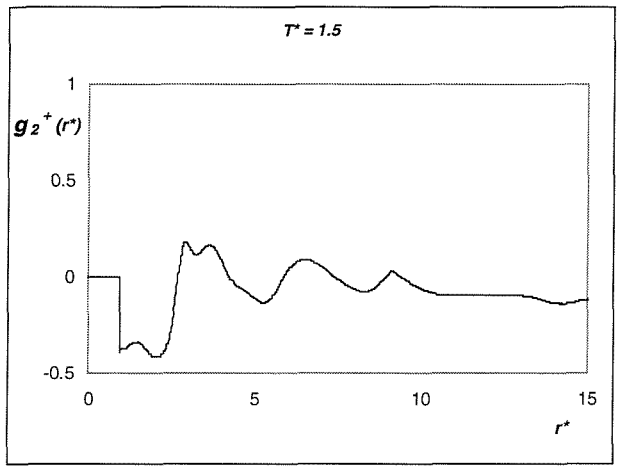

(a)

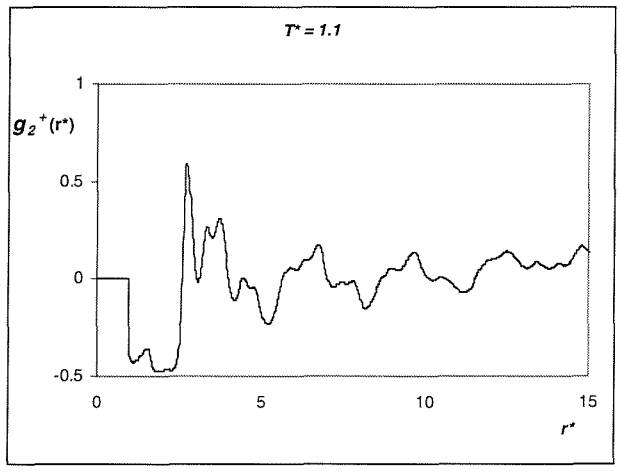

(b)

Figure 5.1.14 Radial correlation coefficient at a scaled pressure of 2.0 for (a) the smectic A phase at a scaled temperature of 1.5; (b) the crystal B phase at a scaled temperature of 1.1.

5.3.2 Comparison with Zewdie's results

The system of spherocylinders which we have investigated, has already been studied by Zewdie [13]. The author used a significantly smaller system of 432 particles and employed constant volume Monte Carlo simulations, although using an algorithm which allows for the change in the shape of the box to favour the equilibration process and help the system to escape from metastable states. In our case we have studied a much larger system (2000 particles) and in an orthorhombic box using constant pressure Monte Carlo simulation. Zewdie presented a detailed investigation for a sample at a scaled number density, ρ^*, of 0.23 as a function of the scaled temperature T^* and surprisingly five different phases were identified:

0.48 0.75 1.22 1.29
Cr----------SmB---------SmA---------N---------I

He did not do a cooling run to check for hysterisis. The five phases were identified by using various distribution functions, such as g(r*), and $g(r^*_{\|})$ as well as order parameters and thermodynamic properties. For our system, the isotropic phase is stable for densities lower than 0.23, while the smectic A phase is stable for densities larger than 0.23. Also, no nematic phases were observed in our simulations.

5.4 System 2

For this system, the spherocylinder with a sphere of radius 1.5 in the middle, we observe the phase sequence Cr-N-I. The phases were identified by examining the snapshots analysing and the plots of distribution and thermodynamic properties. In figure 5.4.1, we present the thermodynamic quantities for this system at the scaled pressure of 1.0. Two transitions can be identified, at scaled temperatures of 1.75 ± 0.05 and 1.25 ± 0.05 which correspond to the N-I and Cr-N transitions, respectively. For the N-I transition, the enthalpy of transition ΔH^* was estimated to be 1.28 ± 0.05 corresponding to an entropy change, $\Delta S/R$, of 0.73 ± 0.05. The values of the orientational order parameter, $\langle P_2 \rangle$, are reported in figure 5.2.1(c). The relative change in volume for the nematic-isotropic transition is estimated to be 8.7%, which is higher than that observed for the GB mesogen which was 4.2%. For the scaled temperatures of 2.0 down to 1.8 the system is in the isotropic phase, as indicated by the small value (< 0.1) for the order parameter. Then at T^* of about 1.70 ± 0.05, the system has a transition to the nematic phase. This is indicated by the increase in the value of the order parameter to about 0.45 at the scaled temperature of 1.7. The system stays in the nematic phase down to a scaled temperature of 1.3 at which point, the order parameter has gradually increased to a value of about 0.7. This value seems to be relatively high for a nematic phase (cf. 0.3 to 0.6), however, form the snapshots and calculated structural properties (see later), there is no indication of a layered phase and the system is still translationally disordered.

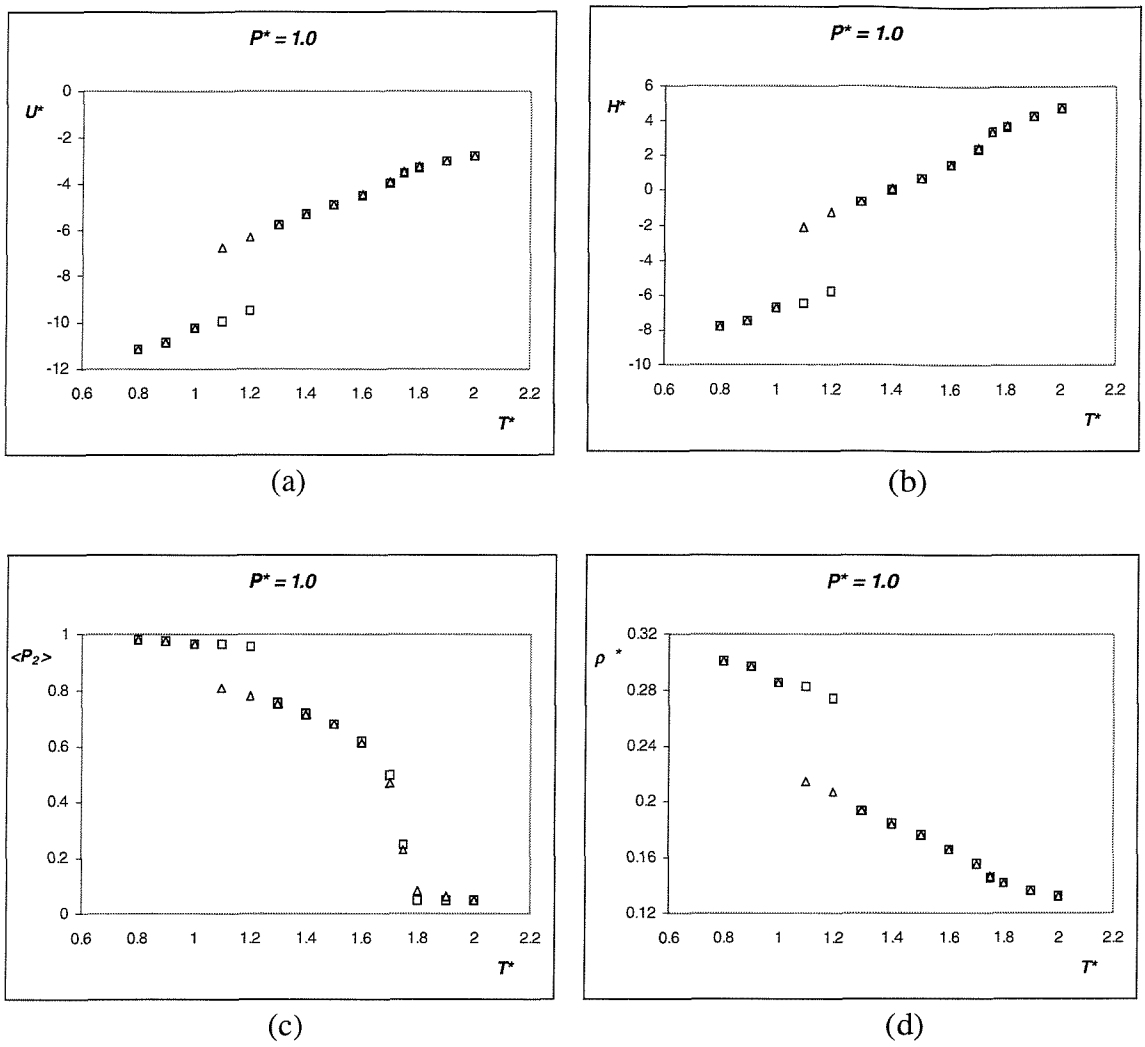

Figure 5.4.1 Thermodynamic properties for the sample at a scaled pressure P^* of 1.0 as a function of the scaled temperature T^*. Squares represent the cooling run while the triangles represent the heating run. (a) Scaled energy per particle, U^*, (b) scaled enthalpy per particle, H^*, (c) orientational order parameter $\langle P_2 \rangle$ and (d) scaled density ρ^*.

For the scaled pressure of 2.0, we observe the same phase behaviour, Cr-N-I, identified from the snapshots of the particles during the production run. The significance of the snapshots is that the phase can quickly be identified, with respect to the molecular orientations. For example the orientationaly ordered nematic and the disordered isotropic can be easily identified, or the layers present in the smectic phases can be seen. The thermodynamic plots for this pressure are presented in figure 5.4.2. The N-I transition occurs at a scaled temperature, T^*, of 2.45 ± 0.05, an increase in T_{NI}^* of 0.7. The change in enthalpy, ΔH^*, associated with this transition is 1.3 ± 0.05 corresponding to an entropy change, $\Delta S/R$, of 0.53 ± 0.05. Then at T^* of 1.75, the system undergoes a transition to the crystal phase. The change in enthalpy for this transition is estimated to be 5.6 ± 0.05 with an associated entropy change of 3.2 ± 0.05. The values of ΔH^* and $\Delta S/R$ are typical for a nematic crystal transition, since the system goes from no long-range translational order to a translationally ordered phase. In figure 5.4.2(d), we have presented the scaled density, ρ^*, for the system as a function of the scaled temperature. For the isotropic-nematic transition the relative change in volume is about 8.8% and for the nematic crystal transition it is about 62.5%.

The values of the orientational order parameter are reported in figure 5.4.2(c). In the isotropic phase, which occurs for T^* greater than 2.5, the order parameter is less than 0.1. Then at the scaled temperature of 2.45 where the nematic isotopic transition occurs, the order parameter starts to increase and at T^* of 2.4, the system is in the nematic phase with an order parameter, $\langle P_2 \rangle$, of about 0.5. The system stays in the nematic phase and the value of the order parameter increases to about 0.75 at T^* of 1.7, just before the transition to the crystal phase. This value of the order parameter, 0.75, seems rather high for a

nematic phase, but the structural properties show no signs of translational order for T^* of 1.7. The Cr-N transition temperature, is very difficult to determine due to the presence of large hysterisis, but the transition occurs in the temperature range of 1.4 -1.7. The value of the order parameter reaches a maximum value of 0.980 at the scaled temperature, T^*, of 1.3, showing a highly orientationally ordered phase.

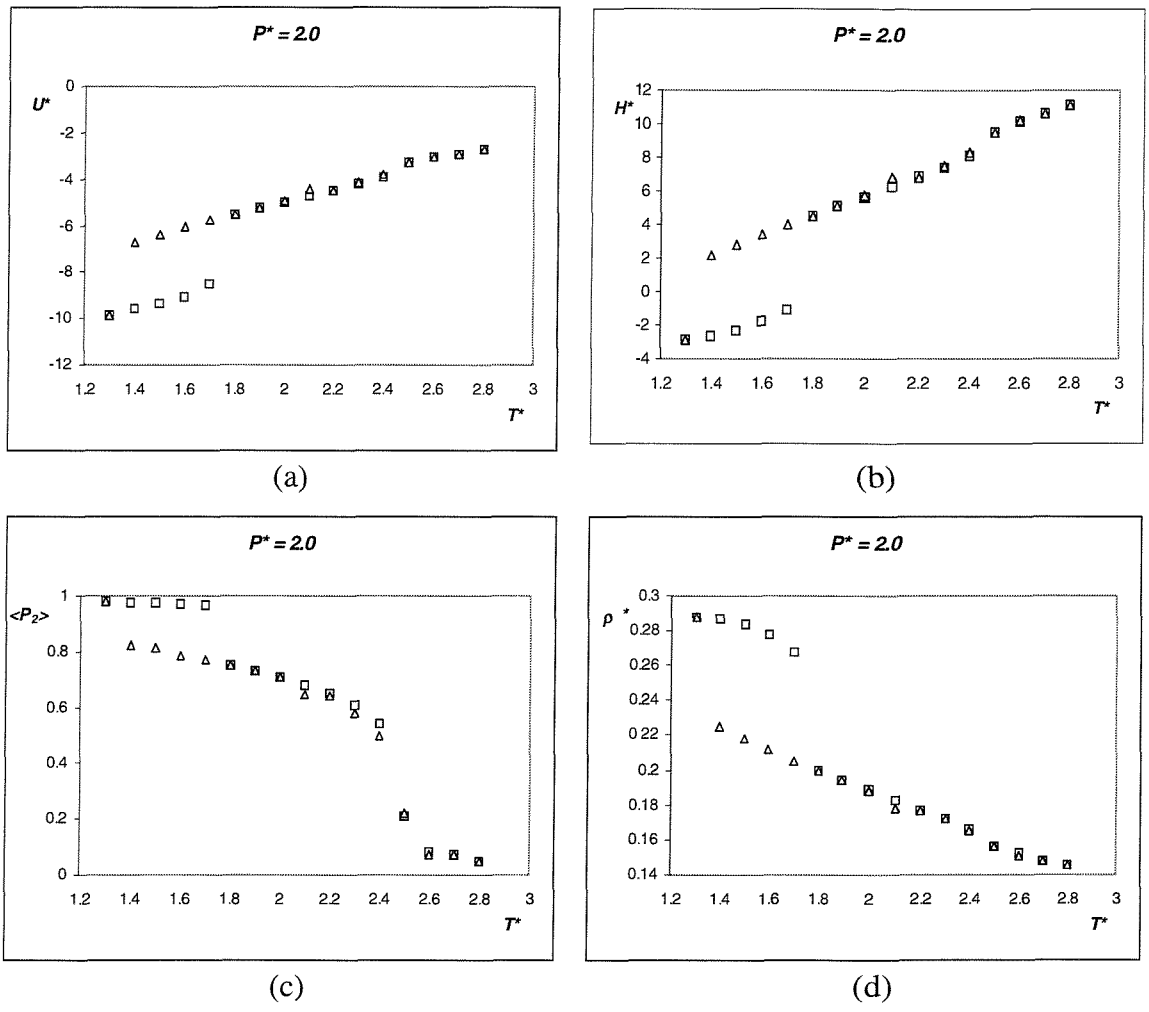

Figure 5.4.2 Thermodynamic properties for system 2 at a scaled pressure P^* of 2.0 as a function of the scaled temperature T^*. Squares represent the cooling run while the triangles represent the heating run. (a) Scaled energy per particle, U^*, (b) scaled enthalpy per particle, H^*, (c) orientational order parameter $<P_2>$ and (d) scaled number density ρ^*.

5.4.2 Structural properties

We now turn our attention to the structural properties to support our tentative identification of the phases from the thermodynamic properties explained in the last subsection. The singlet orientational distribution function for the system at the scaled pressure of 2.0 is shown in figure 5.4.3(a) for the nematic phase at the scaled temperature, T^* of 1.8 and in figure 5.4.3(b) for the crystal phase at T^* of 1.3. We notice that for the nematic phase, the data are much noisier than that in the crystal phase. The reason being that in the nematic phase the system has lower orientational order and so the distribution function has significant values spread over a larger range. This description is in contrast to the crystal phase, where in figure 5.4.3(b) we see a smooth line which is strongly peaked for values of $\cos \beta$ close to unity. In the crystal phase the molecules are highly ordered and the ordering of the molecules extends throughout the sample and so virtually all of the molecules are parallel to the director. The line in the plot for the nematic phase appears to be noisy, however, this is due to the larger scale selected to see the peak more clearly. The snapshots of the molecules for the nematic and crystal phase are shown in figures 5.4.4(a) and 5.4.4(b). Although it is difficult to discern the long-range translational order in figure 5.4.4(b), as expected for a crystal phase, the distribution functions (see later) do suggest a highly ordered phase. The singlet translational distribution function, $\rho(z)$, are reported in figure 5.4.5 for the crystal phase. As we discussed in the Chapter 3, mesogens having this shape anisotropy, i.e. a spherocylinder with a central sphere favour a slipped parallel, rather than a side-by-side, arrangement to enhance packing efficiency. A demonstration of this description is shown in figure 5.4.5 where we can see that the layer spacing is very

small, about 1.1 and as a result there are many peaks associated with this phase. If the phase was not tilted, one would expect a value for the layer spacing which is comparable to that of the length of the molecules, in this case 3.0, and accordingly fewer layers. The broad peak observed in figure 5.4.5 is somewhat unrealistic due to this tilted arrangement of molecules, and so the z axis, dose not represent the layer normal.

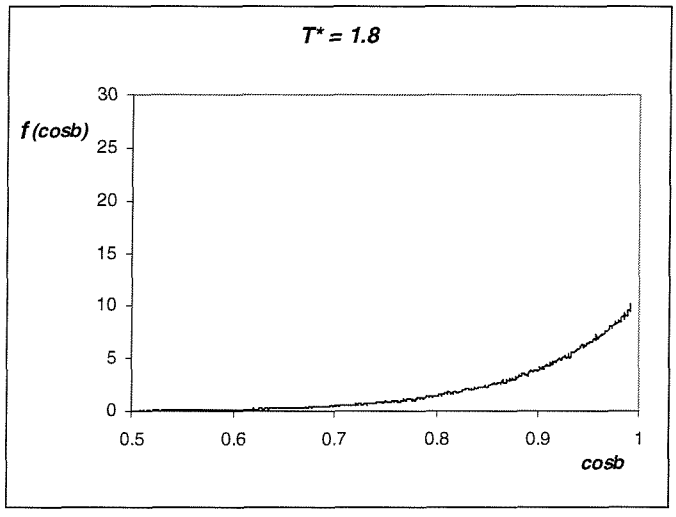

(a)

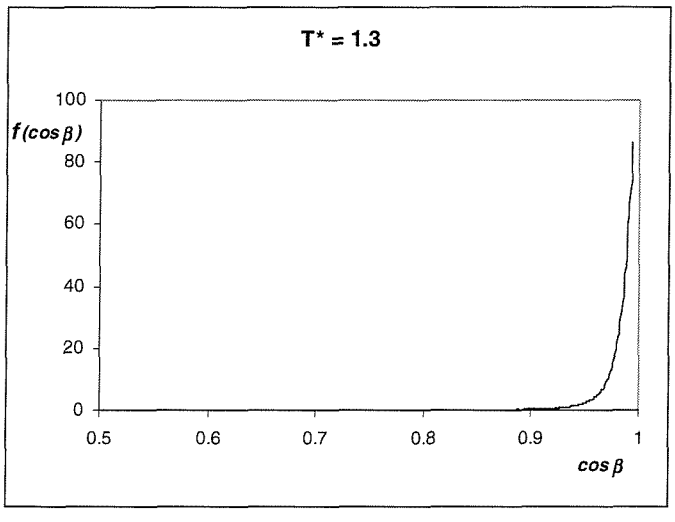

(b)

Figure 5.4.3 Singlet orientational distribution function, $f(\cos \beta)$, for system 2 at a scaled pressure of 2.0. (a) nematic phase at a scaled temperature, T^*, of 1.8; (b) crystal phase at a scaled temperature of 1.3.

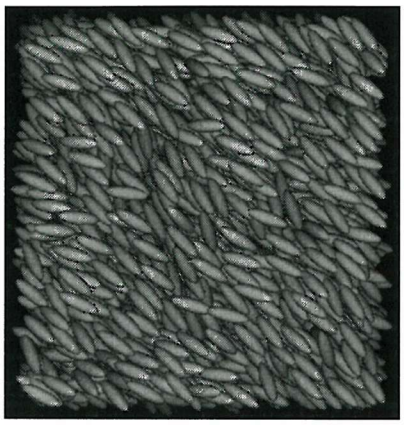

(a)

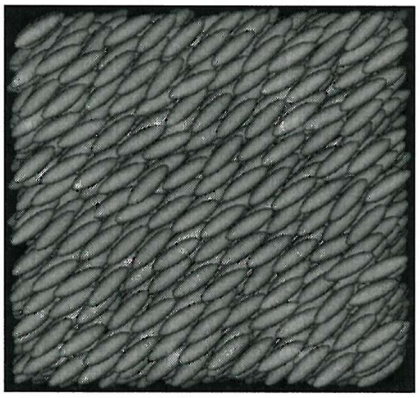

(b)

Figure 5.5.4 Snapshots of the configurations for system 2 at a scaled pressure of 2.0 for (a) the nematic phase at a scaled temperature of 1.8; (b) the crystal phase at a scaled temperature of 1.3.

The distribution functions for ordered phases are calculated along the director. For smectic A and B phases the molecules are, on average, parallel to the layer normal, and as we have seen in the case for system 1, the simulations give these intiutive results. However, for system 2, where the particles are tilted with respect to the layer normal, then the calculation becomes cumbersome and it is very difficult to identify the 'right' layers,

and so the plots for the distribution functions would not give the expected results. Nevertheless, they can still be informative and assist us in identifying the phases formed. In figure 5.4.5, the z axis is the director. Normally the translational distribution function is calculated along the layer normal, but because the phase is tilted, the calculation is done along the director, and so the function calculates distribution for molecules from different layers. The graph has a periodic nature, with a periodicity of about 1.

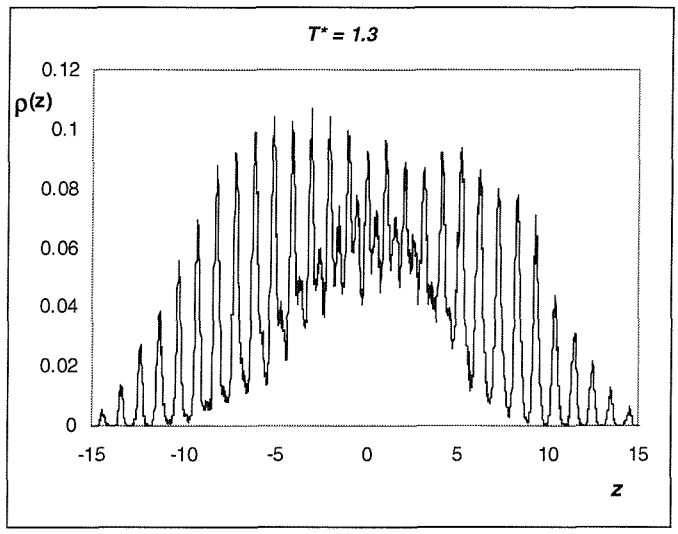

Figure 5.4.5 The singlet translational distribution function, $\rho(z)$, at a scaled pressure of 2.0 for the crystal phase at a scaled temperature of 1.3.

The radial distribution function, $g(r^*)$, for the nematic phase and the crystal phase are shown in figures 5.4.6(a) and 5.4.6(b), respectively. In the nematic phase, we do not observe much structure, as expected. The only obvious structure is a sharp peak at a scaled distance, r^*, of 1.6 followed by a smaller peak, but with a cusp-like shape at a scaled distance of about 3.0. The first peak corresponds to the molecule at a distance of

1.6 from the reference molecule, which is slightly larger than the diameter of the sphere, namely 1.5. The second peak could either correspond to a molecule, which is in an end-to-end arrangement with the reference molecule or to another molecule, which is at a distance of 3.0 from the reference molecule. After the second peak, we only see a horizontal line, indicating a loss of correlation for distances greater than 3.0. The plot for the crystal phase necessarily shows much more structure and the correlation between particles extends to distances as large as 10.0, which is half the size of the simulation box. The first peak is at a scaled distance of about 1.5, which could correspond to a neighbouring molecule in a side-by-side arrangement, rather than slipped. In the crystal phase, the molecules are tightly packed as indicated by the change in the density and so explains why the first peak in the nematic phase is at a scaled distance of 1.6, but in the crystal phase it has decreased to 1.5. The next two peaks are at scaled distances of 1.9 and 2.4, which could correspond to molecules being in a slipped parallel arrangement with the reference molecule. The fourth peak is at a scaled distance of 3.0, either an end-to-end arrangement or two molecules apart in a parallel arrangement. The other peaks are more difficult to assign since they arise from many contributions. In figure 5.4.7, we show the parallel distribution function, $g_{\|}(r_{\|}^*)$, for the crystal phase. This is useful to extract the values of the layer spacing, although this is not apparent from the snapshot; it is found to be about 1.1, which is another indication that the molecules are tilted with respect to the layer normal. The presence of peaks even at large distances, indicates that the phase is highly ordered. Once again, the unusual shape of this plot for $g_{\|}(r_{\|}^*)$ (see figure 5.4.7), could be due to the fact that it is calculated along the director with the assumption that the

director is parallel to the layer normal, but here, the director is at inclined to the layer normal.

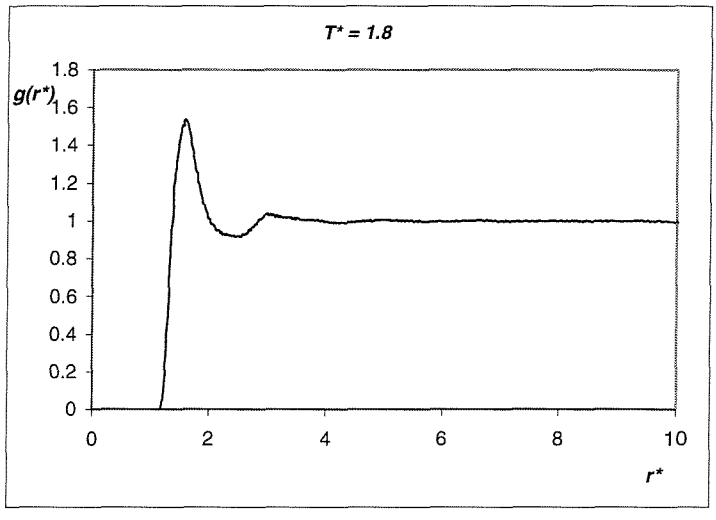

(a)

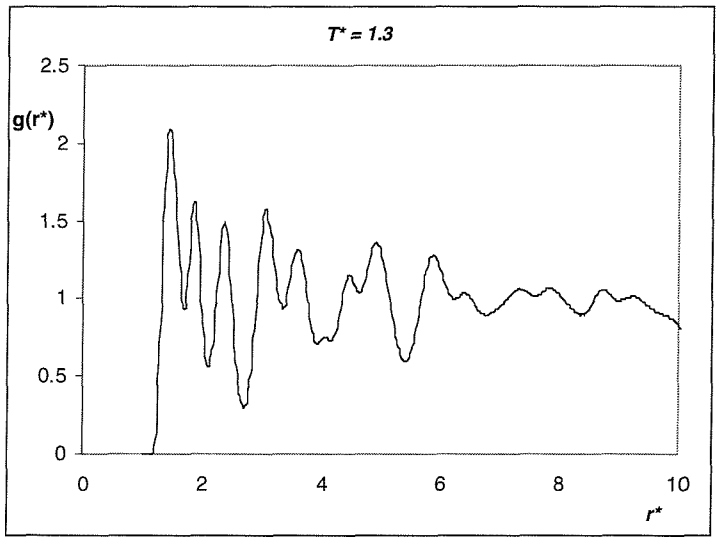

(b)

Figure 5.4.6 Radial distribution function, g(r*), for the two phases at a scaled pressure of 2.0. (a) nematic phase at a scaled temperature, T*, of 1.8 and (b) crystal phase at T* of 1.3.

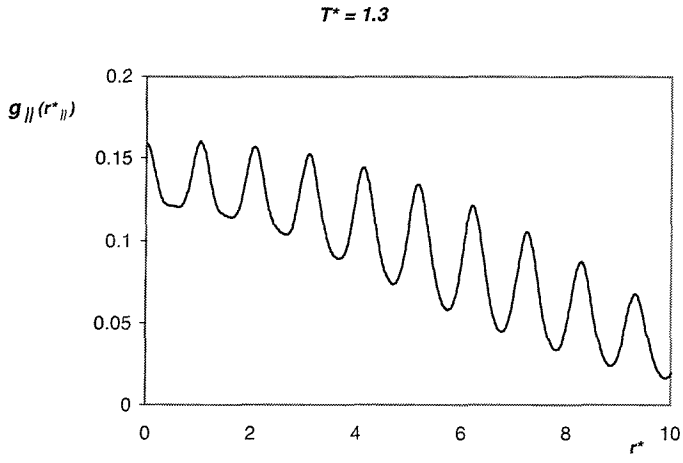

Figure 5.4.7 The parallel distribution function, $g_{\parallel}(r^*_{\parallel})$, at a scaled pressure of 2.0 for the crystal phase at a scaled temperature of 1.3.

In addition to the parallel distribution function, we have also calculated the perpendicular distribution functions, $g_{\perp}^{n}(r_{\perp}^*)$, for the crystal phase at T^* of 1.3. Although this function may not necessarily be as useful for a tilted phase because of the difficulty of identifying the layers, it is still worth examining. The within-layer distribution function $g_{\perp}^{0}(r_{\perp}^*)$ gives information about the correlations for pairs of particles within the same layer, while the between-layer distribution function $g_{\perp}^{1}(r_{\perp}^*)$ examines the correlations for pairs of particles in layers 0 and 1. Further information may be obtained by extending this distribution function to next nearest neighbours, e.g. $g_{\perp}^{2}(r_{\perp}^*)$ which examines the

correlations for pairs of particles in layers 0 and 2. By examining the relative positions of peaks for each layer, we can distinguish the structure and the arrangements of molecules with respect to each other. In figure 5.4.8(a) we show the within-layer perpendicular distribution function for the crystal phase. We notice that it is very structured and the presence of the double peak at a scaled distance of 2.0 indicates a local hexatic arrangement of molecules. The between-layer perpendicular distribution functions, $g_{\perp}^{1}(r_{\perp}^{*})$ and $g_{\perp}^{2}(r_{\perp}^{*})$ are shown in figures 5.4.8(b) and 5.4.8(c), respectively. The peaks at zero may indicate AAA packing of molecules. Finally, in figure 5.4.9, we show the distance dependence of the coefficient $g_2^{+}(r)$, describing the average orientation of the interparticle vector with respect to the director, for the crystal phase. This function is very useful since we can understand how the molecules are arranged with respect to each other and in this case, since the molecules are tilted with respect to the layer normal, we can calculate the tilt angle from the plot of $g_2^{+}(r)$. This is done by taking the value of height of the first peak, in this case 0.2 which corresponds to the average value $<P_2(\cos\beta_r)_r>$,

$$< P_2(\cos\beta_r)_r >= 0.2. \qquad (5.8)$$

The angle β, is the angle between the director and the molecular long axis evaluates to 46.9°. Also we see that in the plot of $g_2^{+}(r)$, the first peak is positive, which means that β has to be less than 90°, i.e. the molecules are not side-by-side, but must be in a slipped parallel arrangement. However, the second peak is very prominent and negative, about -0.5. This suggests that two molecules must be in a parallel arrangement. This arrangement is shown in figure

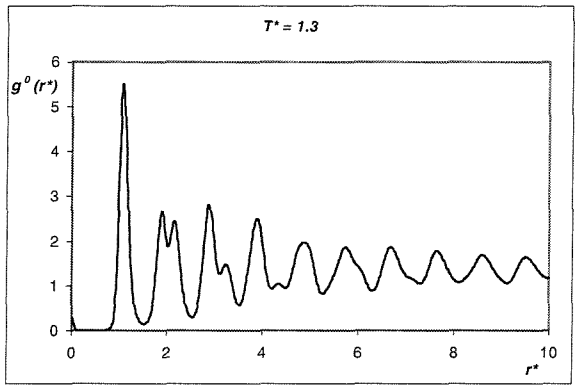

(a)

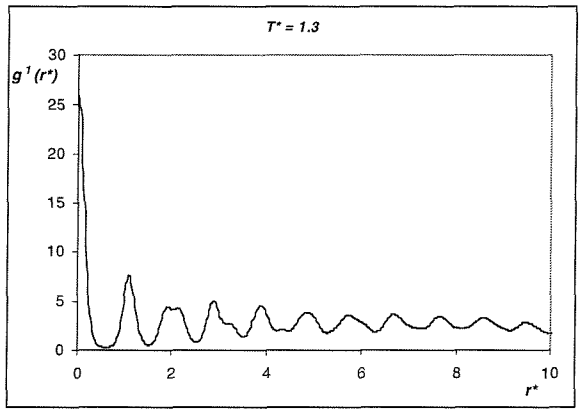

(b)

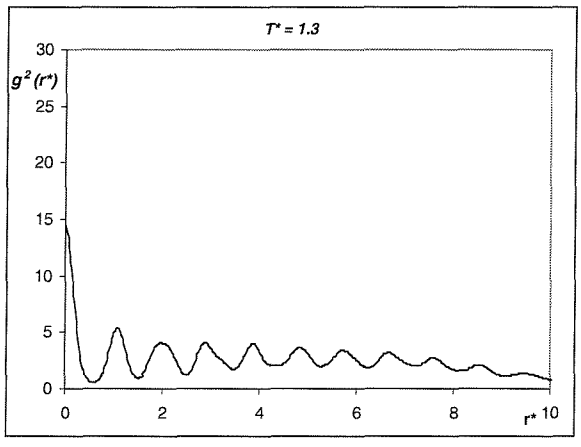

(c)

Figure 5.4.8 The perpendicular distribution function for (a) the translational order within a layer, $g_{\perp}^{0}(r_{\perp})$, (b) the translational order between adjacent layers, $g_{\perp}^{1}(r_{\perp})$, and (c) next nearest neighbours, $g_{\perp}^{2}(r_{\perp})$, at the scaled pressure of 2.0 for the crystal phase at T^* of 1.3.

(a)

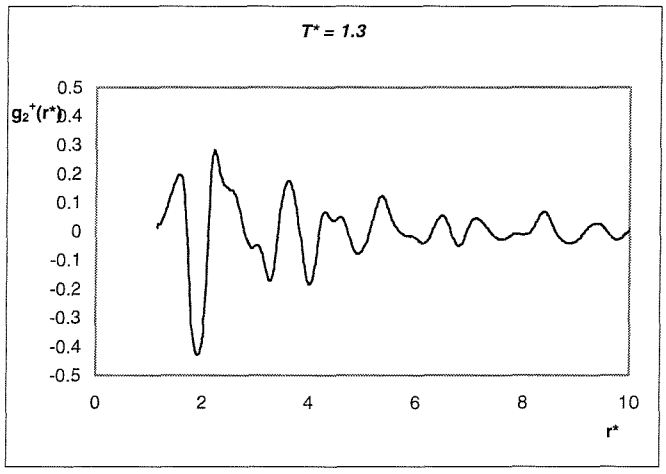

Figure 1.5.14(a) Distribution function for the coefficient $g_2^+(r^*)$ at a scaled pressure of 2.0 for

(b)

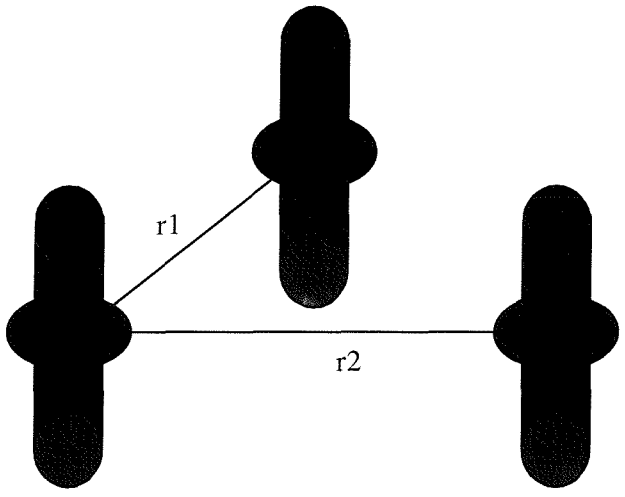

Figure 1.5.14(b) The arrangements of molecules which represent slipped parallel r1 and side-by-side r2, which give rise to the positive and negative peaks in the plot of g_2^+, (see figure 1.5.14(a)). For clarity, the molecules are shown with spaces between them.

5.5 System 3

For this system, a spherocylinder with a sphere of radius 1.75 in the centre, we find the same phase pattern, as that for system 2. That is the system forms three stable phases, Cr-N-I, however, the slight increase of 2.75 in the diameter of the central sphere of the spherocylinders, has the effect of increasing significantly the temperature range over which the nematic phase is stable. The phases were identified from the distribution functions produced after the production run. The nematic-isotropic transition occurs at a scaled temperature of about 4.5 and the crystal-nematic transition temperature occurs at T^* of 1.75. The thermodynamic plots for this system at a scaled pressure, P^*, of 1.0 are presented in figure 5.5.1. The enthalpy change, ΔH^*, for the nematic-isotropic transition is estimated to be 2.39 ± 0.05. The change in entropy, $\Delta S/R$, corresponding to this transition is 0.50 ± 0.05. The crystal-nematic transition occurs at the scaled temperature of 1.90 ± 0.05. For this transition, we expect relatively large values for ΔH^* and $\Delta S/R$ because of the large difference in translational order encountered going from the crystal to nematic phase. The change in enthalpy for this transition is about 6.74 ± 0.05 with an associated entropy change of 3.54 ± 0.05. In contrast to system 2, where we see a very large hysterisis, here we observe none. The plot for the scaled density, ρ^*, are reported in figure 5.5.1(d). The relative change in density for the nematic- isotropic transition is about 12% while for the crystal-nematic transition the relative change is much greater, about 53%, because ρ is very small which suggests an expanded liquid. This is similar to system 2 where we see a very large density change for the two transitions.

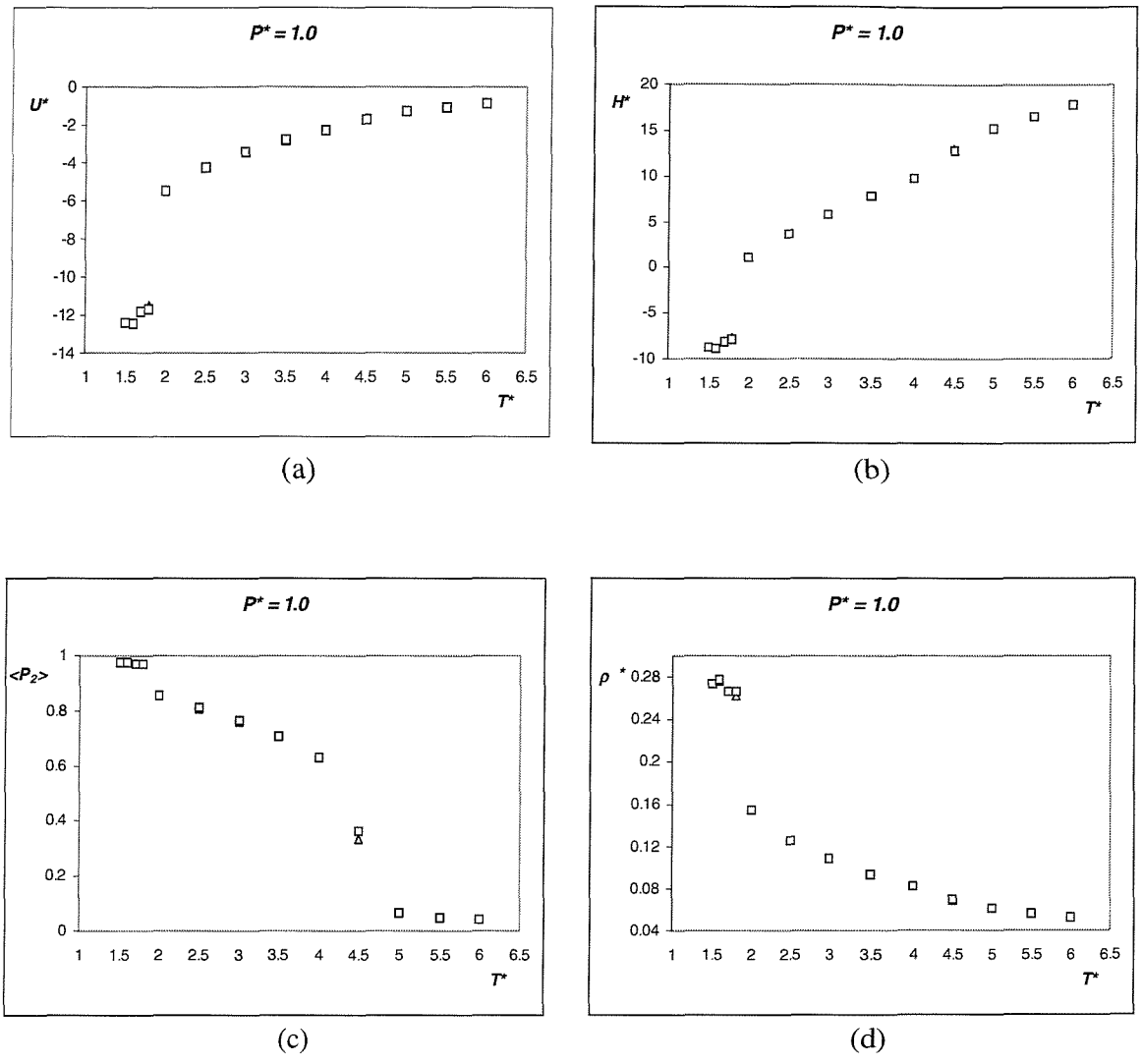

Figure 5.5.1 Thermodynamic properties for system 3 at a scaled pressure P^* of 1.0 as a function of the scaled temperature T^*. Squares represent the cooling run while the triangles represent the heating run. (a) Scaled energy per particle, U^*, (b) scaled enthalpy per particle, H^*, (c) orientational order parameter $\langle P_2 \rangle$ and (d) scaled number density ρ^*.

The orientational order parameters are shown in figure 5.5.1(c), where we can see that the system is in the isotropic phase for scaled temperatures greater than 4.75, as indicated by the low values of $<P_2>$. The nematic phase is stable for the long scaled temperature range of 4.5 to 2.0. The order parameter has a value of 0.35 for the scaled temperature, T^*, of 4.5 while at T^* of 2.0, just before the transition to the crystal phase, it has increased to a value of 0.86. For scaled temperatures less than 1.9 the system is in a very ordered phase as indicated by the large value of 0.98 for the order parameter.

For pressure 2.0, we observe the same phase behaviour as that at the lower scaled pressure of 1.0, i.e. Cr-N-I. The plots for the thermodynamic properties and the order parameter are shown in figure 5.5.2, although with cusp-like slopes for the density and enthalpy plots near the N-I transition. The nematic-isotropic transition occurs at a scaled temperature, T^*, of 8.25 ± 0.025, an increase of about 4 in T^*, in comparison with T_{NI} for pressure 1.0, and the crystal-nematic transition occurs at the scaled temperature of 2.5 ± 0.1. The change in enthalpy, ΔH^* for the nematic-isotopic transition is estimated to be 3.62 ± 0.025 with a corresponding entropy change, $\Delta S/R$, of 0.44 ± 0.025, while for the crystal-nematic transition it is estimated to be 12.9 ± 0.1 with an associated entropy change of 5.16 ± 0.1. The relative change in volume for the nematic-isotropic transition is about 11%, and for the crystal-nematic transition it is 57%. The nematic phase is stable down to the scaled temperature of 3.0. The order parameter, $<P_2>$ keeps increasing from a value of 0.3 at T^* of 8.25 to a value of 0.88 at T^* of 3.0. Below T^* of 3.0, the system is in the crystal phase with an order parameter of 0.98 at T^* of 1.8.

5.5.2 Structural properties

We now turn our attention to the structural properties for this system. The singlet orientational distribution function, $f(\cos\beta)$, is shown in figures 5.5.1(a) for the nematic phase and 5.5.1(b) for the crystal phase. We see that for both phases the form of the plot is essentially the same as those for system 2. The peak in the plot for the crystal phase is slightly sharper and closer to the value of 1.0, which indicates that it is significantly more ordered than the crystal phase in system 2.

In figure 5.5.2, the plot for the translational distribution function for the crystal phase at T* of 2.0 is shown. The structure of the plot is the same as that observed for system 2. Again, the distribution function which should be calculated along the layer normal, in this case, because of the tilted arrangement of molecules, is not calculated against the layer normal. The graph is periodic with a periodicity of about 1.

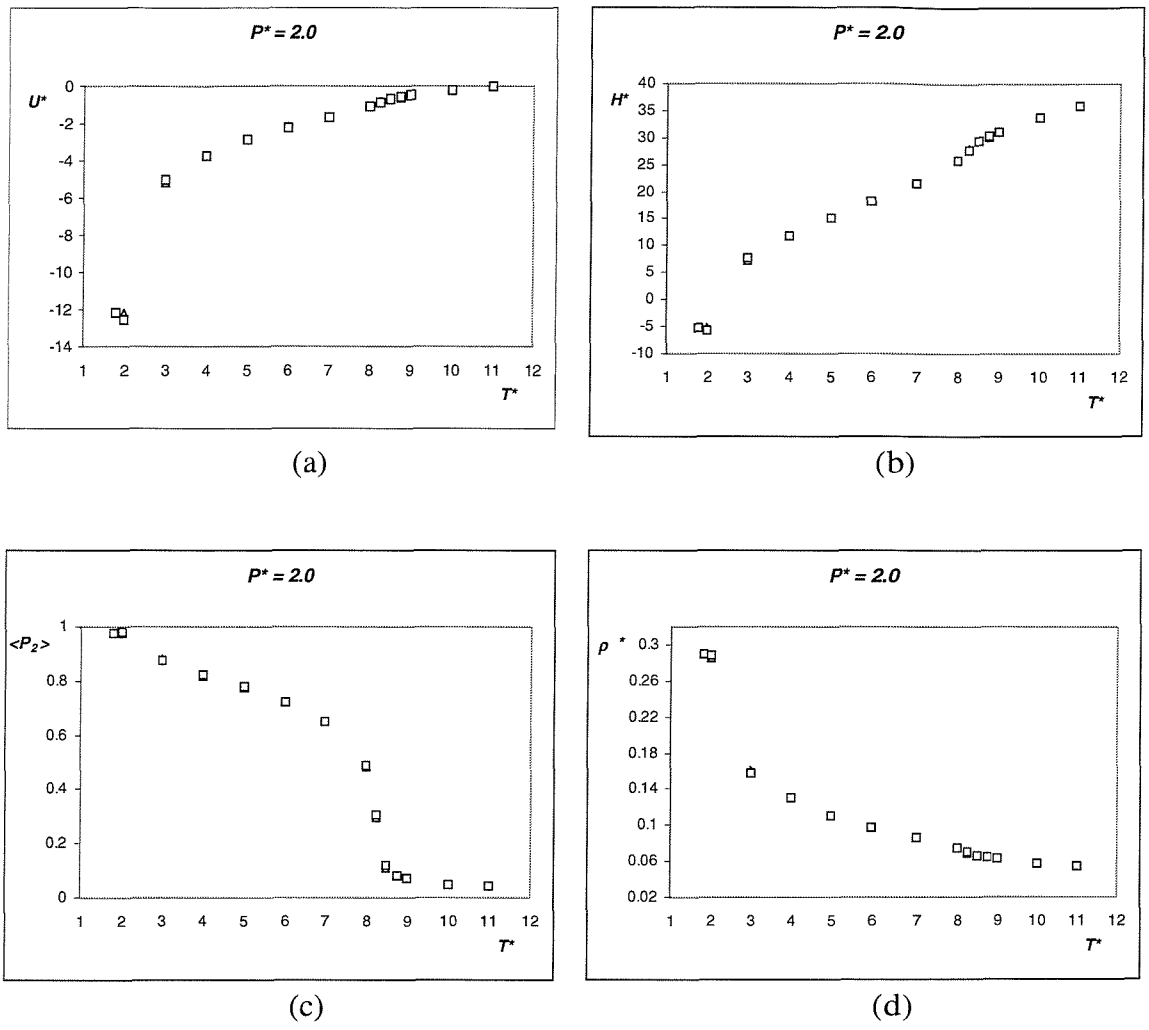

Figure 5.5.2 Thermodynamic properties for system 3 at a scaled pressure P^* of 2.0 as a function of the scaled temperature T^*. Squares represent the cooling run while the triangles represent the heating run. (a) Scaled energy per particle, U^*, (b) scaled enthalpy per particle, H^*, (c) orientational order parameter $<P_2>$ and (d) scaled number density ρ^*.

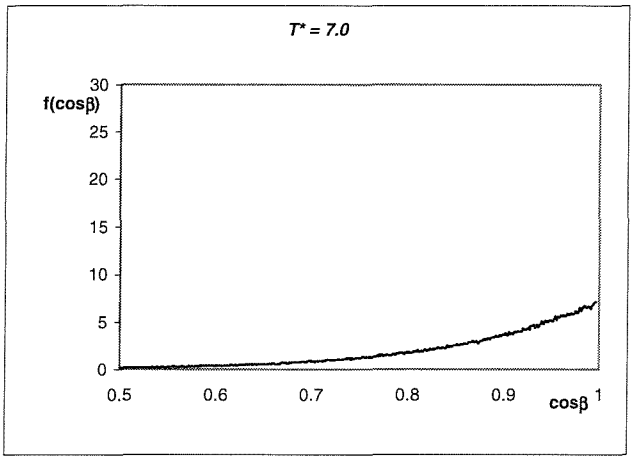

(a)

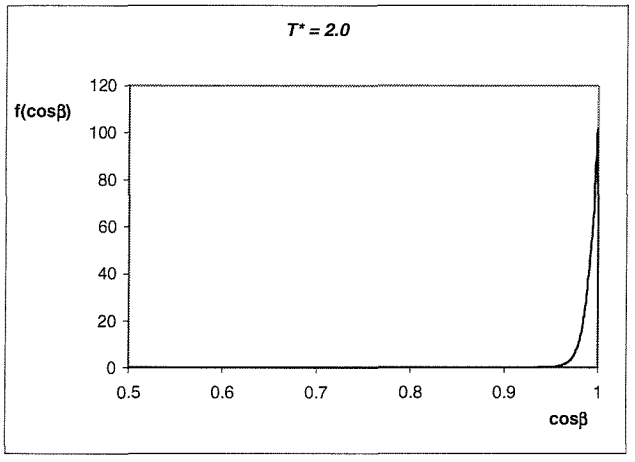

(b)

Figure 5.5.1 Singlet orientational distribution function, $f(cos\beta)$, for the system at a scaled pressure of 2.0. (a) nematic phase at a scaled temperature, T^*, of 7.0; (b) crystal phase at a scaled temperature of 2.0.

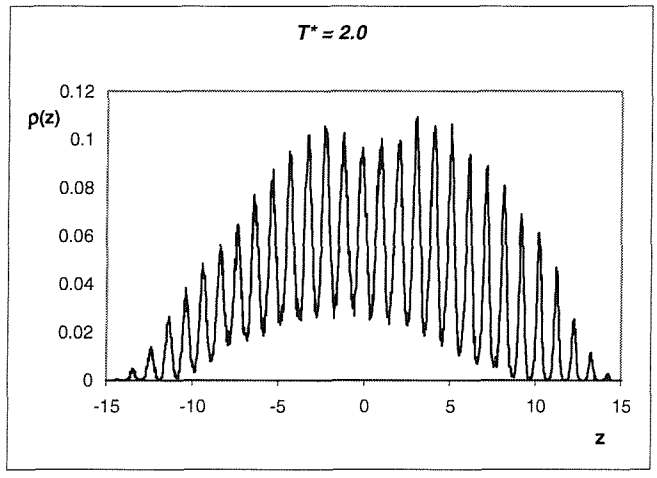

Figure 5.5.2 Singlet translational distribution function, $\rho(z)$, at a scaled pressure of 2.0 for the crystal phase of system 3 at a scaled temperature of 2.0.

The radial distribution function, g(r*) for the nematic phase and the crystal phases are shown in figures 5.5.3(a) and 5.5.3(b), respectively. For the nematic phase, there is only one peak which occurs at a scaled distance, r^*, of about 2.1. If the molecules were on average arranged side-by-side, we would see the first maximum peak at 1.75, which corresponds to the diameter of the sphere. However, the value of 2.1 suggests that the molecules are arranged skewed-parallel rather than side-by-side. In the crystal phase, the plot of $g(r^*)$ shows more structure, as expected. This plot is very similar with that for system 2. In both plots we see the structure extends to large distances. The first peak occurs at a distance of about 1.5, the next at a scaled distance of 1.9 and the third at a scaled distance of 2.4, but none at a scaled distance of 1.75, in keeping with our argument that the molecules are not arranged side-by-side, but slipped-parallel. The fourth peak occurs at a scaled distance of 3.0 which could correspond to two molecules arranged end-to-end. For the crystal phase, we have also calculated the parallel distribution function,

$g_{\|}(r_{\|}^*)$. This is shown in figure 5.5.4 and because the molecules are highly ordered, then we still see structure in the plot of this distribution function even at large scaled distances. From this plot, we can calculate the layer spacing and it is about 1, similar to the layer spacing for system 2.

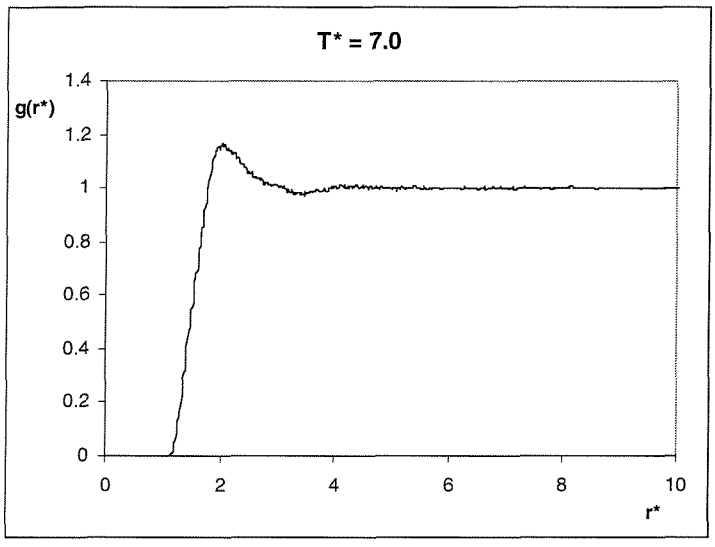

(a)

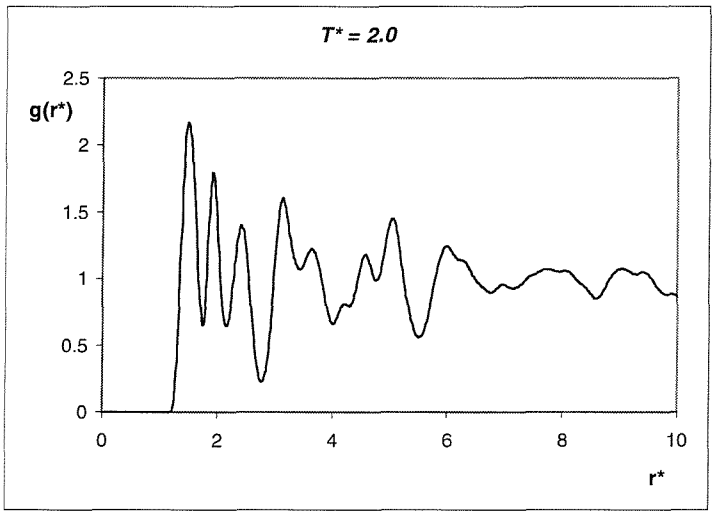

(b)

Figure 5.5.3 Radial distribution function, g(r*), for the three phases of system 3 at a scaled pressure of 2.0. (a) nematic phase at a scaled temperature, T*, of 7.0 and (b) crystal phase at T* of 2.0.

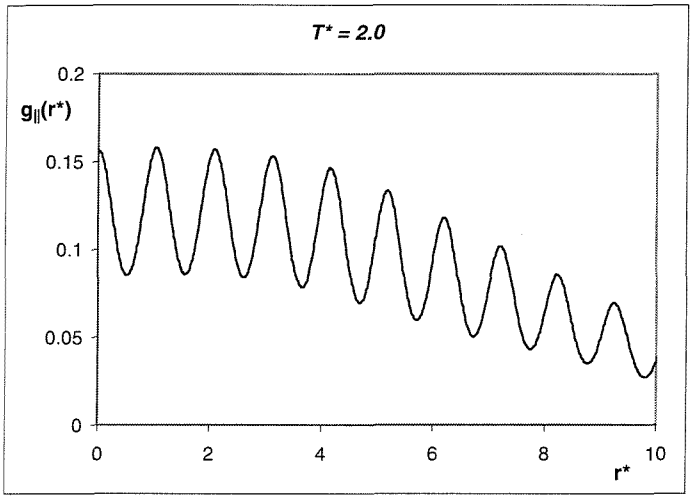

Figure 5.5.4 The parallel distribution function, $g_{\parallel}(r^*_{\parallel})$, at a scaled pressure of 2.0 for the crystal phase of system 3 at a scaled temperature of 2.0.

The perpendicular distribution function, $g_{\perp}^{n}(r_{\perp}^*)$, for within-layer and between-layer for the crystal phase is reported in figure 5.5.5. We see that they are all very structured. For the within-layer distribution function, the first peak is at a scaled distance of 1.1, again another indication that the molecules are tilted rather than in a side-by-side arrangement. Also the peaks at zero indicate that the molecules are packed in an AAA arrangement.

We finish our discussion with an overview of the results and phase behaviour seen for the three systems. In Chapter 3 we introduced the S-functions and how they can be combined with different coefficients, to produce different shapes, in contrast to the GB potential, which limits the shapes of particles to ellipsoids. The importance of this is that we can choose a range of S-functions with different coefficients and investigate the phase behaviour, via computer simulation techniques. The phase behaviour observed for the

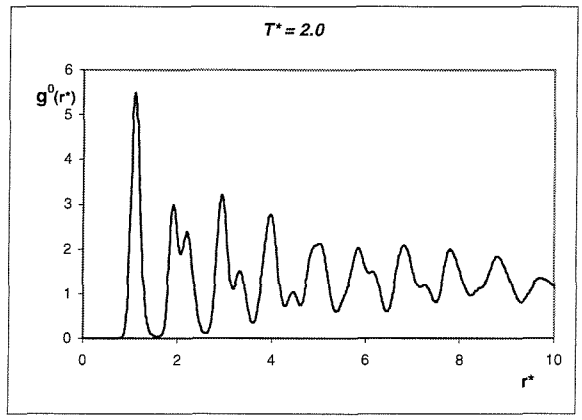

(a)

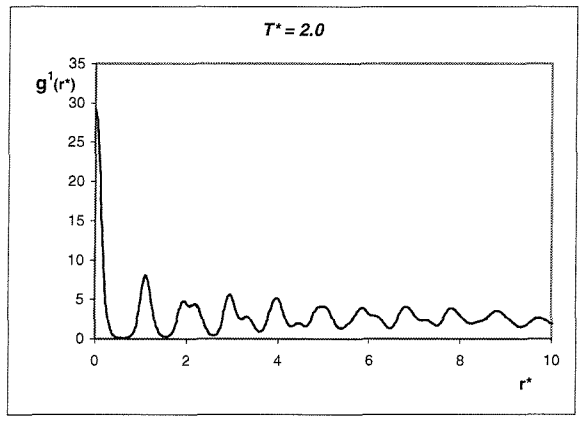

(b)

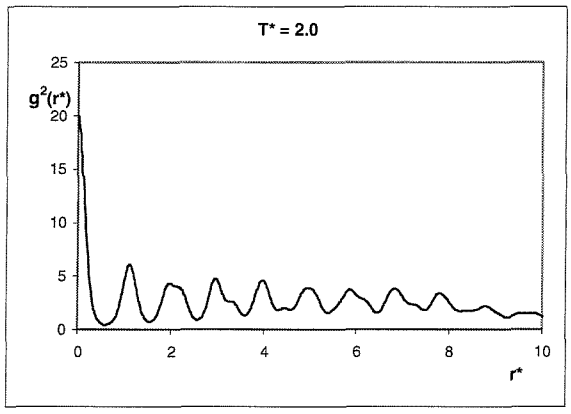

(c)

Figure 5.5.5 The perpendicular distribution function for (a) the translational order within a layer, $g_{\perp}^{0}(r_{\perp})$, (b) the translational order between adjacent layers, $g_{\perp}^{1}(r_{\perp})$, and (c) next nearest neighbours, $g_{\perp}^{2}(r_{\perp})$, at the scaled pressure of 2.0 for the crystal phase of system 3 at T^* of 2.0.

system of spherocylinders (system 1) is similar to that for the GB mesogens, i.e we see the phase pattern, SmB-SmA-I. For system 2 and system 3, where we introduce a sphere in the middle of a spherocylinder, we see a different phase pattern, Cr-N-I. In contrast to our initial prediction that molecules with this shape anisotropy are likely to form SmC phases, due to the tilted arrangement of molecules, here, we have clearly seen that no smectic phase is formed, although the particles pack themselves in a tilted arrangement in the crystal phase. Moreover the sphere destroys the smectic layers, and induces a nematic phase.

References

[1] Duncan W Bruce and Dermot O'Hare, *Inorganic Materials 2nd Edition.*

[2] *The Molecular Physics of Liquid Crystals*, edited by G.R. Luckhurst and G.W. Gray (Academic, London, 1979).

[3] J. Corner, *Proc. R. Soc. Lond. A* **192**, 275 (1948).

[4] P. Bolhuis, D. Frenkel, *J. Chem. Phys.*, **106**, 666 (1997).

[5] J.G. Gay, B.J. Berne, *J. Chem. Phys.*, **74**, 3316 (1981).

[6] B.J. Berne, P. Pechukas, *J.Chem. Phys.*, **56**, 4213 (1972).

[7] A.J. Stone, *Mol. Phys.* **36**, 241 (1978).

[8] (a) S.H. Walmsley, *Chem. Phys. Lett.*, **49**, 320 (1977);
(b) A.L. Tsykalo, A.D. Bagmet, *Mol. Cryst. Liq. Cryst*, **46**, 111 (1978).

[9] M.A. Bates, G.R. Luckhurst, *J. Chem. Phys.*, **110**, 7087 (1999).

[10] G.R. Luckhurst, P.S.J. Simmonds, *Mol. Phys.*, **80**, 233 (1993).

[11] D.J. Adams, G.R. Luckhurst, R.W. Phippen, *Mol. Phys.*, **61**, 1575 (1987).

[12] E. de Miguel, E. Martin del Rio, J.T. Brown, M.P. Allen, *J. Chem. Phys.*, **105**, 4234 (1996).

[13] H.B. Zewdie, *J. Chem. Phys.*, **108**, 2117 (1998).

[14] W.H. Press, B.P. Flannery, S.A. Teukolsky, W.T. Vetterling, *Numerical Recipes: The Art of Scientific Computing* (Cambridge University Press, Cambridge England, 1986), p.301.

[15] M.P. Allen, D.J. Tildesley, *Computer Simulation of Liquids*, (Oxford, Oxford University Press, 1989).

[16] J.A. Barker, R.O. Watts, *Chem. Phys. Lett.*, **3**, 144 (1969).

[17] J. Vieillard-Baron, *Mol. Phys.*, **28**, 809 (1974).

[18] D. Demus, S. Diele, M. Klapperstuck, V. Link, H. Zaschke, *Mol. Cryst. Liq. Cryst.*, **15**, 161 (1971).

The relation between the different orientations and the corresponding shapes produced for two Gay-Berne molecules.

The contact distance for the Gay-Berne potential is given by

$$\sigma = \sigma_0 \left\{ 1 - \chi \left(\frac{f_1^2 + f_2^2 - 2\chi\, f_1 f_2 f_0}{1 - \chi^2 f_0^2} \right) \right\}^{-1/2} ,$$

where $f_0 = \hat{u}_1 \cdot \hat{u}_2$, $f_1 = \hat{u}_1 \cdot \hat{r}$ and $f_2 = \hat{u}_2 \cdot \hat{r}$.

Side-to-end orientation:

$f_0 = 0,\ f_1 = \cos\theta,\ f_2 = \sin\theta$,

which gives $\sigma = \sigma_0 \left\{ 1 - \chi \left(\cos^2\theta + \sin^2\theta \right) \right\}^{-1/2}$,

$$\sigma = \frac{\sigma_0}{(1-\chi)^{1/2}} .$$

I.e. the contact distance σ is a constant giving a circle, i.e. a spherical shape.

Cross configuration:

$f_0 = 0,\ f_1 = \cos\theta,\ f_2 = \sin\theta$,

$\sigma = \sigma_0 \left\{ 1 - \chi \left(\cos^2\theta \right) \right\}^{-1/2}$,

$\sigma^2 = {\sigma_0}^2 \left\{ 1 - \chi \left(\cos^2\theta \right) \right\}$,

Dividing both sides by ${\sigma_0}^2$ gives:

$$\frac{\sigma^2}{{\sigma_0}^2} - \chi \left(\frac{\sigma^2}{{\sigma_0}^2} \right) \cos^2\theta = 1 ,$$

which is the form for an ellipsoid in spherical polar co-ordinates.

Limiting cases:

$\cos^2\theta = 0$ giving $\sigma^2 = {\sigma_0}^2$,

$\cos^2\theta = 1$ giving $\sigma^2 = {\sigma_0}^2\left(\frac{1}{1-\chi}\right)$,

$$\chi = \frac{\left(\frac{\sigma_e}{\sigma_s}\right)^2 - 1}{\left(\frac{\sigma_e}{\sigma_s}\right)^2 + 1},$$

$$1-\chi = \frac{\left(\frac{\sigma_e}{\sigma_s}\right)^2 + 1 - \left(\frac{\sigma_e}{\sigma_s}\right)^2}{\left(\frac{\sigma_e}{\sigma_s}\right)^2 + 1},$$

$$\frac{1}{1-\chi} = \frac{\left(\frac{\sigma_e}{\sigma_s}\right)^2 + 1}{2},$$

$\sigma^2 = {\sigma_0}^2$ which gives $\sigma^2 = \frac{{\sigma_e}^2 + {\sigma_s}^2}{2}$.

Side-by-Side configuration

$f_0 = 0,\ f_1 = f_2 = \cos\theta$,

$$\sigma = \sigma_0\left\{1-\chi\left(\frac{2\cos^2\theta - 2\chi\sin^2\theta}{1-\chi^2}\right)\right\}^{-1/2},$$

$$= \sigma_0\left\{1-2\chi\cos^2\theta\left(\frac{1-\chi}{1-\chi^2}\right)\right\}^{-1/2},$$

$$= \sigma_0 \left\{ 1 - \left(\frac{2\chi}{1-\chi} \right) \cos^2 \theta \right\}^{-1/2},$$

which represents the equation for an ellipsoid.

$$\frac{1+\chi}{\chi} = \left\{ \frac{(\sigma_e/\sigma_s)^2 + 1 + (\sigma_e/\sigma_s)^2 - 1}{(\sigma_e/\sigma_s)^2 - 1} \right\},$$

$$= \frac{\sigma_e^2 + \sigma_s^2}{2\sigma_e^2},$$

$$\sigma = \sigma_0 \left\{ 1 - \left(\frac{\sigma_e^2 + \sigma_s^2}{\sigma_e^2} \right) \cos^2 \theta \right\}^{-1/2},$$

$$= \sigma_0 \left\{ \left(\frac{\sigma_e^2 - \sigma_e^2 + \sigma_s^2}{\sigma_e^2} \right) \cos^2 \theta \right\}^{-1/2},$$

Limiting cases:

$\cos\theta = 0$ giving $\sigma = \sigma_0$,

$\cos\theta = 1$ giving $\sigma = \sigma_e$.